

<sup>1</sup> MEASUREMENT OF ELECTROWEAK PRODUCTION OF  
<sup>2</sup> SAME-SIGN W BOSON PAIRS WITH ATLAS (WORKING  
<sup>3</sup> TITLE)

<sup>4</sup> William Kennedy DiClemente

<sup>5</sup> A DISSERTATION

<sup>6</sup> in

<sup>7</sup> Physics and Astronomy

<sup>8</sup> Presented to the Faculties of The University of Pennsylvania  
<sup>9</sup> in Partial Fulfillment of the Requirements for the Degree of Doctor of Philosophy

<sup>10</sup> 2019 *Last compiled: February 4, 2019*

---

<sup>11</sup>  
<sup>12</sup> I. Joseph Kroll, Professor, Physics  
<sup>13</sup> Supervisor of Dissertation

---

<sup>14</sup>  
<sup>15</sup> Joshua Klein, Professor, Physics  
<sup>16</sup> Graduate Group Chairperson

<sup>17</sup> Dissertation Committee  
<sup>18</sup> Elliot Lipeles, Associate Professor, Physics  
<sup>19</sup> Christopher Mauger, Associate Professor, Physics  
<sup>20</sup> Burt Ovrut, Professor, Physics  
<sup>21</sup> Justin Khoury, Professor, Physics  
<sup>22</sup> I. Joseph Kroll, Professor, Physics

23 MEASUREMENT OF ELECTROWEAK PRODUCTION OF SAME-SIGN W BOSON PAIRS  
24 WITH ATLAS (WORKING TITLE)

25 COPYRIGHT  
26 2019  
27 William Kennedy DiClemente

28 All rights reserved.

---

## Acknowledgements

---

<sup>30</sup> I'd like to thanks the Ghosts of Penn Students Past for providing me with such an amazing thesis  
<sup>31</sup> template.

32

## ABSTRACT

33 MEASUREMENT OF ELECTROWEAK PRODUCTION OF SAME-SIGN W BOSON PAIRS  
34 WITH ATLAS (WORKING TITLE)

35

William Kennedy DiClemente

36

J. Kroll

37

This is the abstract text.

---

# Contents

---

|    |   |       |
|----|---|-------|
| 39 | <b>Acknowledgements</b>   | iii   |
| 40 | <b>Abstract</b>   | iv    |
| 41 | <b>Contents</b>   | v     |
| 42 | <b>List of Tables</b>   | ix    |
| 43 | <b>List of Figures</b>  | xii   |
| 44 | <b>Preface</b>  | xviii |
| 45 | <b>1 Introduction</b>   | 1     |
| 46 | <b>2 Theoretical Framework</b>                                  | 2     |
| 47 | 2.1 Introduction to the Standard Model . . . . .                | 2     |
| 48 | 2.2 Electroweak symmetry breaking and the Higgs boson . . . . . | 4     |
| 49 | 2.3 Vector boson scattering in the Standard Model . . . . .     | 7     |
| 50 | <b>3 LHC and the ATLAS Detector</b>                             | 11    |
| 51 | 3.1 The Large Hadron Collider . . . . .                         | 11    |
| 52 | 3.2 The ATLAS Detector . . . . .                                | 11    |
| 53 | 3.2.1 The Inner Detector . . . . .                              | 11    |
| 54 | 3.2.1.1 Pixel Detector . . . . .                                | 11    |
| 55 | 3.2.1.2 Semiconductor Tracker . . . . .                         | 11    |
| 56 | 3.2.1.3 Transition Radiation Tracker . . . . .                  | 11    |

|    |          |   |           |
|----|----------|---|-----------|
| 57 | 3.2.2    | The Calorimeters . . . . .  | 12        |
| 58 | 3.2.2.1  | Liquid Argon Calorimeters . . . . .   | 12        |
| 59 | 3.2.2.2  | Tile Calorimeters . . . . .   | 12        |
| 60 | 3.2.3    | The Muon Spectrometer . . . . .   | 12        |
| 61 | 3.2.4    | Particle reconstruction . . . . .   | 13        |
| 62 | 3.2.4.1  | Track reconstruction . . . . .  | 13        |
| 63 | 3.2.4.2  | Muon reconstruction . . . . .   | 13        |
| 64 | 3.2.4.3  | Electron reconstruction . . . . .   | 13        |
| 65 | 3.2.4.4  | Jet reconstruction . . . . .  | 13        |
| 66 | <b>4</b> | <b>Alignment of the ATLAS Inner Detector</b>  | <b>14</b> |
| 67 | 4.1      | The alignment method . . . . .  | 15        |
| 68 | 4.1.1    | Alignment levels . . . . .  | 18        |
| 69 | 4.1.2    | Alignment coordinate systems . . . . .  | 19        |
| 70 | 4.2      | Early 2015 alignment of the ATLAS detector . . . . .  | 20        |
| 71 | 4.2.1    | June alignment procedure . . . . .  | 22        |
| 72 | 4.2.2    | Alignment results . . . . .   | 23        |
| 73 | 4.2.2.1  | Residual distributions from collisions . . . . .  | 24        |
| 74 | 4.2.2.2  | Track parameter resolution from cosmic rays . . . . .   | 26        |
| 75 | 4.2.3    | Error scaling . . . . .   | 27        |
| 76 | 4.3      | Level 2 alignment of the TRT . . . . .  | 30        |
| 77 | 4.4      | Momentum bias from sagitta deformations . . . . .   | 31        |
| 78 | 4.4.1    | Sagitta bias monitoring with electron $E/p$ . . . . .   | 33        |
| 79 | 4.4.1.1  | Measuring $\langle E/p \rangle$ . . . . .   | 34        |
| 80 | 4.4.1.2  | Results in 13 TeV data . . . . .  | 35        |
| 81 | <b>5</b> | <b>Measurement of same-sign <math>WW</math> production at <math>\sqrt{s} = 13</math> TeV with ATLAS</b> | <b>39</b> |
| 82 | 5.0.2    | Experimental overview of vector boson scattering . . . . .  | 39        |
| 83 | 5.0.3    | Same-sign $W^\pm W^\pm$ scattering . . . . .  | 40        |
| 84 | 5.0.4    | Overview of backgrounds . . . . .   | 42        |
| 85 | 5.1      | Data and Monte Carlo samples . . . . .  | 45        |
| 86 | 5.1.1    | Monte Carlo samples . . . . .   | 45        |
| 87 | 5.2      | Object and event selection . . . . .  | 46        |

|     |  |    |
|-----|--|----|
| 88  | 5.2.1 Object selection . . . . .   | 47 |
| 89  | 5.2.1.1 Muon candidate selection . . . . .   | 47 |
| 90  | 5.2.1.2 Electron candidate selection . . . . .                                     | 48 |
| 91  | 5.2.1.3 Jet candidate selection . . . . .  | 49 |
| 92  | 5.2.1.4 Treatment of overlapping objects . . . . .                                 | 50 |
| 93  | 5.2.2 Signal event selection . . . . .   | 51 |
| 94  | 5.3 Background estimations . . . . .   | 52 |
| 95  | 5.3.1 Estimation of the $WZ$ background . . . . .                                  | 53 |
| 96  | 5.3.2 Estimation of the $V\gamma$ background . . . . .                             | 55 |
| 97  | 5.3.3 Estimation of backgrounds from charge misidentification . . . . .            | 56 |
| 98  | 5.3.3.1 Validation of the charge misidentification estimate . . . . .              | 58 |
| 99  | 5.3.4.4 Estimation of non-prompt backgrounds with the fake factor method . . . . . | 59 |
| 100 | 5.3.4.1 Overview of the default fake factor method . . . . .                       | 60 |
| 101 | 5.3.4.2 The fake factor with $p_T^{\text{cone}}$ . . . . .                         | 61 |
| 102 | 5.3.4.3 Application of the fake factor . . . . .                                   | 64 |
| 103 | 5.3.4.4 Systematic uncertainties . . . . .   | 67 |
| 104 | 5.3.4.5 Results of the fake factor . . . . .                                       | 68 |
| 105 | 5.3.4.6 Validation of the fake factor . . . . .                                    | 71 |
| 106 | 5.3.5 Reduction of $WZ$ background using custom overlap removal . . . . .          | 71 |
| 107 | 5.4 Cross section measurement . . . . .  | 76 |
| 108 | 5.4.1 Maximum likelihood fit . . . . .   | 76 |
| 109 | 5.4.2 Definition of the fiducial volume . . . . .                                  | 78 |
| 110 | 5.4.3 Cross section extraction . . . . .   | 79 |
| 111 | 5.5 Summary of uncertainties . . . . .   | 80 |
| 112 | 5.5.1 Experimental uncertainties . . . . .   | 80 |
| 113 | 5.5.2 Theoretical uncertainties . . . . .  | 83 |
| 114 | 5.5.2.1 Uncertainties from EWK-QCD interference . . . . .                          | 83 |
| 115 | 5.6 Results . . . . .  | 84 |
| 116 | <b>6 Prospects for same-sign <math>WW</math> at the High Luminosity LHC</b>        | 88 |
| 117 | 6.0.1 Analysis Overview . . . . .  | 89 |
| 118 | 6.1 Theoretical motivation . . . . .   | 89 |
| 119 | 6.1.1 Experimental sensitivity to longitudinal polarization . . . . .              | 90 |

|     |   |     |
|-----|---|-----|
| 120 | 6.2 Monte Carlo samples . . . . .   | 91  |
| 121 | 6.3 Background estimations . . . . .  | 92  |
| 122 | 6.3.1 Truth-based isolation . . . . .   | 92  |
| 123 | 6.4 Object and event selection . . . . .  | 93  |
| 124 | 6.4.1 Object selection . . . . .  | 93  |
| 125 | 6.4.2 Event selection . . . . .   | 94  |
| 126 | 6.5 Selection optimization . . . . .  | 95  |
| 127 | 6.5.1 Random grid search algorithm . . . . .  | 95  |
| 128 | 6.5.2 Inputs to the optimization . . . . .  | 97  |
| 129 | 6.5.3 Results of the optimization . . . . .   | 98  |
| 130 | 6.6 Results . . . . .   | 99  |
| 131 | 6.6.1 Event yields . . . . .  | 99  |
| 132 | 6.6.2 Uncertainties . . . . .   | 102 |
| 133 | 6.6.3 Cross section measurement . . . . .   | 103 |
| 134 | 6.6.4 Longitudinal scattering significance . . . . .  | 103 |
| 135 | <b>7 Conclusion</b>   | 107 |
| 136 | <b>A Additional material on <math>W^\pm W^\pm jj</math> measurement at <math>\sqrt{s} = 13\text{TeV}</math></b> | 108 |
| 137 | A.1 Impact of experimental uncertainty on MC background estimations . . . . .                                   | 108 |
| 138 | A.2 Additional signal region plots . . . . .  | 110 |
| 139 | <b>B Additional material on <math>W^\pm W^\pm jj</math> prospects at the HL-LHC</b>                             | 111 |
| 140 | B.1 Truth isolation . . . . .   | 111 |
| 141 | B.1.1 TRUTH1++ derivations . . . . .  | 112 |
| 142 | B.1.2 Check of truth-based isolation . . . . .  | 113 |
| 143 | B.1.3 Loose isolation working point . . . . .   | 113 |
| 144 | B.2 Plots of other optimization variables . . . . .   | 116 |
| 145 | <b>Bibliography</b>   | 118 |

---

## List of Tables

---

|     |      |  |    |
|-----|------|--|----|
| 147 | 4.1  | The four alignment levels for each of the detector subsystems. The total number of alignable structures and degrees of freedom (DoF) to be aligned are given for each level.   | 20 |
| 149 | 4.2  | Summary of the highest level of alignment applied to each ID subsystem when deriving the June alignment. . . . .   | 23 |
| 151 | 4.3  | Estimated value of the error scaling term $b$ for each subdetector component with the June alignment. . . . .  | 30 |
| 153 | 5.1  | Predicted cross sections for EQK and QCD production of diboson processes relevant to VBS at $\sqrt{s} = 8\text{TeV}$ using the <b>SHERPA</b> MC generator. Loose generator level cuts are applied on lepton $p_T > 5\text{ GeV}$ , dilepton invariant mass $m_{ll} > 4\text{ GeV}$ , and at least two jets with $m_{jj} > 10\text{ GeV}$ . . . . . | 42 |
| 157 | 5.2  | Summary of MC samples used in the analysis. . . . .  | 46 |
| 158 | 5.3  | Muon selection criteria. All muons are required to pass the preselection (top), and then either the signal (middle) or loose (bottom) criteria is applied to the preselected electrons. . . . .  | 48 |
| 160 | 5.4  | Electron selection criteria. All electrons are required to pass the preselection (top), and then either the signal (middle) or loose (bottom) criteria is applied to the preselected electrons. . . . .  | 49 |
| 163 | 5.5  | Jet selection criteria. All jets are required to pass the above selection in order to be used in the analysis. . . . .   | 50 |
| 165 | 5.6  | Summary of the overlap removal procedure used in the analysis. If the criteria in the “check” column is met, in the “result” column, the object on the left of the arrow is removed in favor of the object on the right. . . . .   | 51 |
| 168 | 5.7  | Summary of trigger requirements for electrons and muons for $\sqrt{s} = 13\text{TeV}$ data collected in 2015 and 2016. At least one of the triggers must be satisfied. . . . .   | 51 |
| 170 | 5.8  | The signal event selection. . . . .  | 53 |
| 171 | 5.9  | Event yields in the $WZ$ control region before normalization. All lepton flavor channels are combined. . . . .   | 55 |
| 173 | 5.10 | Selection criteria for the $V\gamma$ control region. . . . .   | 55 |
| 174 | 5.11 | Event yields in the $V\gamma$ control region. The $V\gamma$ scale factor of 1.77 is calculated by scaling up the $Z\gamma$ and $Z+\text{jets}$ backgrounds to account for the difference between the data and predicted total background. . . . .  | 56 |
| 177 | 5.12 | Selection criteria for the same-sign inclusive validation region. . . . .  | 59 |

|     |      |  |     |
|-----|------|--|-----|
| 178 | 5.13 | Event selection for the dijet region used for calculating the fake factor. The selected lepton can pass either the nominal (signal) or loose selections. In the case of the nominal leptons, the $p_T > 27$ GeV requirement is replaced with $p_T > 15$ GeV. . . . .   | 65  |
| 179 |      |  | 70  |
| 180 | 5.14 | Values of the fake factor in each $p_T$ bin and for each individual systematic source. . . . .   | 70  |
| 181 | 5.15 | Estimated yields for the fake lepton background. The estimated yield is shown in the first column together with the statistical uncertainty followed by the systematic uncertainties from variations of the the fake factors within their statistical (stat.) and systematic (syst.) uncertainties. The labels $f_e$ and $f_\mu$ indicate the fake factors for electrons and muons, respectively. . . . .  | 70  |
| 182 | 5.16 | Selection criteria for the same-sign top fakes validation region. . . . .  | 71  |
| 183 | 5.17 | Custom OR definition. Leptons must pass this selection in order to be counted for the trilepton veto. . . . .  | 75  |
| 184 | 5.18 | Definition of the fiducial volume. . . . .   | 78  |
| 185 | 5.19 | Impact of various systematic effects on the fiducial cross section measurement. The impact of a given source of uncertainty is computed by performing the fit with the corresponding nuisance parameter varied up or down by one standard deviation from its nominal value. . . . .  | 81  |
| 186 | 5.20 | List of sources of experimental uncertainties on the reconstruction of physics objects. . . . .  | 82  |
| 187 | 5.21 | Impact of experimental uncertainties for the $W^\pm W^\pm jj$ EWK processes in all channels. . . . .   | 82  |
| 188 | 5.22 | Impact of experimental uncertainties for the $WZ$ process in all channels. . . . .   | 82  |
| 189 | 5.23 | The set of generator level cuts used for generating the interference samples with <code>MadGraph</code> . . . . .  | 84  |
| 190 | 5.24 | Cross sections for each different $W^\pm W^\pm jj$ production mode (inclusive, EWK only, QCD only, and interference only) generated using <code>MadGraph</code> . The cross sections are calculated using a minimal set of generator level cuts from events where the $W$ decays to a muon. . . . .  | 84  |
| 191 | 5.25 | Table of the data and prediction event yields in the signal region before the fit. Numbers are shown for the six lepton flavor and charge channels and for all channels combined. Here the $WZ$ background yields are normalized to the data in the $WZ$ control region. The background estimations from the fake factor are included in the “Non-prompt” category, and backgrounds from $V\gamma$ production and electron charge misidentification are combined in the “ $e/\gamma$ conversions” category. Finally, $ZZ$ , $VVV$ , and $t\bar{t}V$ backgrounds are combined in the “Other prompt” category. . . . . | 86  |
| 192 | 5.26 | Table of the data and prediction event yields in the signal region after the fit. Numbers are shown for the six lepton flavor and charge channels and for all channels combined. The background estimations from the fake factor are included in the “Non-prompt” category, and backgrounds from $V\gamma$ production and electron charge misidentification are combined in the “ $e/\gamma$ conversions” category. Finally, $ZZ$ , $VVV$ , and $t\bar{t}V$ backgrounds are combined in the “Other prompt” category. . . . .   | 86  |
| 215 | 6.1  | Summary of MC samples used in the analysis. . . . .  | 92  |
| 216 | 6.2  | Truth-based isolation requirements for electrons and muons. . . . .  | 93  |
| 217 | 6.3  | Summary of the signal event selection. . . . .   | 95  |
| 218 | 6.4  | Updates to the $W^\pm W^\pm jj$ event selection criteria after optimization. Cuts not listed remain unchanged from the default selection in Table 6.3. . . . .   | 98  |
| 220 | 6.5  | Signal and background event yields using the default event selection for an integrated luminosity of $\mathcal{L} = 3000 \text{ fb}^{-1}$ . Events containing a fake or charge-flipped electron are removed from their respective sources and combined into a single entry each. . . . .   | 100 |
| 223 | 6.6  | Signal and background event yields using the optimized event selection for an integrated luminosity of $\mathcal{L} = 3000 \text{ fb}^{-1}$ . Events containing a fake or charge-flipped electron are removed from their respective sources and combined into a single entry each. . . . .   | 101 |

|     |   |     |
|-----|---|-----|
| 226 | 6.7 Summary of estimated experimental and rate uncertainties. . . . .   | 102 |
| 227 | A.1 Impact of experimental uncertainties for the $W^\pm W^\pm jj$ QCD processes in all channels. .  | 108 |
| 228 | A.2 Impact of experimental uncertainties for triboson process in all channels. . . . .  | 109 |
| 229 | A.3 Impact of experimental uncertainties for $t\bar{t}V$ processes in all channels. . . . .   | 109 |
| 230 | A.4 Impact of experimental uncertainties for the $W\gamma$ process in all channels. . . . .   | 109 |
| 231 | A.5 Impact of experimental uncertainties for the $Z\gamma$ process in all channels. . . . .   | 109 |
| 232 | A.6 Impact of experimental uncertainties for the $ZZ$ process in all channels. . . . .  | 110 |
| 233 | B.1 Event yields prior to applying any form of truth-based isolation criteria. . . . .  | 111 |
| 234 | B.2 Event yields after applying a test version of the truth-based isolation. . . . .  | 112 |
| 235 | B.3 Electron and muon isolation requirements for the loose working point. . . . .   | 113 |
| 236 | B.4 Event yields broken down by sample and by background type using the loose isolation<br>237 workingpoint. Events containing a fake or charge-flipped electron are removed from their<br>238 respective sample and added to the “fakes” and “charge flip” rows, respectively. Errors<br>239 include statistical uncertainty and estimated systematic rate uncertainty based on the<br>240 background process. . . . . | 114 |
| 241 | B.5 Event yields broken down by background type using the tight isolation workingpoint.<br>242 Events containing a fake or charge-flipped electron are removed from their respective<br>243 sample and added to the “fakes” and “charge flip” rows, respectively. Errors include sta-<br>244 tistical uncertainty and estimated systematic rate uncertainty based on the background<br>245 process. . . . .             | 115 |

---

# List of Figures

---

|     |     |  |    |
|-----|-----|--|----|
| 247 | 2.1 | An illustration of the potential term $V(\phi)$ in the cases where $\mu^2 > 0$ (left) and $\mu^2 < 0$ (right). The right-hand plot shows the Higgs potential, or ‘‘Mexican hat potential’’, with the minimum at $ \phi  = \sqrt{-\frac{\mu^2}{\lambda}}$ rather than at $ \phi  = 0$ as in the left-hand plot. . . . .   | 5  |
| 250 | 2.2 | Feynman diagram of a generic VBS process. The gray circle represents any interaction with two incoming and two outgoing vector bosons, including any of the diagrams shown in Figures 2.3 and 2.4. . . . .   | 8  |
| 253 | 2.3 | Leading order $VV \rightarrow VV$ Feynman diagrams involving EWK bosons, from right to left: $s$ -channel, $t$ -channel, $u$ -channel, and the quartic gauge coupling. . . . .   | 8  |
| 255 | 2.4 | Leading order $VV \rightarrow VV$ Feynman diagrams involving the exchange of a Higgs boson, from right to left: $s$ -channel, $t$ -channel, and $u$ -channel. . . . .  | 8  |
| 257 | 2.5 | Cross sections in nanobarns for five different scattering processes of longitudinally polarized vector bosons as a function of center of mass energy $\sqrt{s}$ . Without a SM Higgs boson (left), the cross sections grow unbounded with $\sqrt{s}$ ; however with a 120 GeV Higgs boson (right), the cross sections no longer diverge. . . . .               | 10 |
| 261 | 3.1 | General cut-away view of the ATLAS detector. . . . .   | 12 |
| 262 | 4.1 | Graphical representation of the effect of a misaligned detector element. The reconstructed particle track (dashed arrow) differs from the actual trajectory of the particle (solid arrow) due to the shift in one of the detector elements. The cyan lines represent the track-to-hit residuals. . . . .   | 15 |
| 266 | 4.2 | Graphical representation of the ID alignment chain. . . . .  | 18 |
| 267 | 4.3 | A schematic representation of the Inner Detector in the longitudinal plane with the global coordinate system overlaid on top. The Pixel detector and IBL are shown in blue, the SCT in green, and the TRT in red. The local coordinates for each subdetector module are inset on the right. . . . .  | 21 |
| 271 | 4.4 | The $d_0$ distributions with respect to the reconstructed primary vertex using the $\sqrt{s} = 13\text{TeV}$ collision data sample reconstructed using the June (black) and March (green) alignments. The data is compared to a MC simulation using a perfect detector geometry (red). The distributions are normalized to the same number of entries. . . . . | 24 |

|     |      |   |    |
|-----|------|---|----|
| 275 | 4.5  | Local $x$ (left) and local $y$ (right) residual distributions of the IBL planar sensors using the $\sqrt{s} = 13\text{TeV}$ collision data sample reconstructed using the June (black) and March (green) alignments. The data is compared to a MC simulation using a perfect detector geometry (red). The distributions are normalized to the same number of entries. . . . .   | 25 |
| 279 | 4.6  | The mean of the local $x$ (left) and local $y$ (right) residual distributions as a function of the global $z$ position of each IBL module using the $\sqrt{s} = 13\text{TeV}$ collision data sample reconstructed using the June (black) and March (green) alignments. The data is compared to a MC simulation using a perfect detector geometry (red). . . . .   | 26 |
| 283 | 4.7  | Local $x$ (top) and local $y$ (bottom) residual distributions for the Pixel barrel (excluding the IBL, left) and end-caps (right) using the $\sqrt{s} = 13\text{TeV}$ collision data sample reconstructed using the June (black) and March (green) alignments. The data is compared to a MC simulation using a perfect detector geometry (red). The distributions are normalized to the same number of entries. . . . . | 27 |
| 288 | 4.8  | Local $x$ residual distributions for the SCT barrel (left) and end-caps (right) using the $\sqrt{s} = 13\text{TeV}$ collision data sample reconstructed using the June (black) and March (green) alignments. The data is compared to a MC simulation using a perfect detector geometry (red). The distributions are normalized to the same number of entries. . . . .   | 28 |
| 292 | 4.9  | Residual distributions for the TRT barrel (left) and end-caps (right) using the $\sqrt{s} = 13\text{TeV}$ collision data sample reconstructed using the June (black) and March (green) alignments. The data is compared to a MC simulation using a perfect detector geometry (red). The distributions are normalized to the same number of entries. . . . .   | 28 |
| 296 | 4.10 | Representation of splitting a single cosmic ray track passing through the entire detector (left) into two separate tracks (right). . . . .  | 29 |
| 298 | 4.11 | Distribution of the difference in the impact parameter $\Delta d_0$ (left) and charge over transverse momentum $\Delta q/p_T$ (right) between the two cosmic ray split tracks. The June (black) and March (green) alignments are compared. The distributions are normalized to the same number of entries. . . . .  | 29 |
| 302 | 4.12 | Pull distributions in local $x$ (left) and $y$ (right) for the IBL using the $\sqrt{s} = 13\text{TeV}$ collision data sample after applying the error scaling. . . . .  | 30 |
| 304 | 4.13 | Residual means by straw layer in two TRT $\phi$ -sectors affected by a tilt misalignment. The tilts in each of the three modules are clearly visible in the red points representing the reconstructed data prior to alignment. After four iterations of L2 alignment, the residual means in the gray points are flat. . . . .   | 31 |
| 308 | 4.14 | Two dimensional map of residuals in the first layer of the TRT barrel vs $z$ and $\phi$ . Each bin represents the mean of a Gaussian fit to the TRT residuals in that bin. The map on the left is after the L3 (wire-by-wire) alignment of the TRT performed in 2010, and the map on the right is after the L2 alignment at the end of 2015. The $z$ -axis for both plots use the same scale. . . . .                   | 32 |
| 313 | 4.15 | Representation of a curl distortion in the detector. The image shows a cutaway in the transverse plane. The deformation is represented by the red arrows, and the impact on the reconstructed positive (blue) and negative (green) tracks are shown. The dashed lines represent the true particle trajectories, and the solid lines represent the reconstructed trajectories. . . . .                                   | 33 |
| 318 | 4.16 | Geometric definition of the sagitta $s$ in relation to the length of the chord $l$ and the radius $r$ of a circular arc. . . . .  | 33 |
| 320 | 4.17 | $E/p$ distributions of electrons and positrons in two different $\eta\phi$ bins of the detector. The left hand plot is taken from a region with no momentum bias where $\langle E/p \rangle^+ = \langle E/p \rangle^-$ , while the right hand plot shows an 8% disagreement in $\langle E/p \rangle$ between electrons and positrons. . . . .   | 35 |

|     |      |   |    |
|-----|------|---|----|
| 324 | 4.18 | Sagitta bias in the $\sqrt{s} = 13\text{TeV}$ data collected by ATLAS in 2016 as a function of $\eta$ and $\phi$ for the prompt (left) and reprocessed (right) alignments using the $E/p$ method. . . . .   | 36 |
| 325 | 4.19 | Sagitta bias in the $\sqrt{s} = 13\text{TeV}$ data collected by ATLAS in 2016 projected along $\eta$ for the prompt (gray) and reprocessed (blue) alignments using the $E/p$ method. . . . .  | 37 |
| 326 | 4.20 | Sagitta bias in the $\sqrt{s} = 13\text{TeV}$ data collected by ATLAS in 2017 as a function of $\eta$ and $\phi$ in reconstructed electrons (left) and after two iterations of momentum corrections (right) from the $E/p$ method. . . . .  | 37 |
| 327 | 4.21 | Sagitta bias in the $\sqrt{s} = 13\text{TeV}$ data collected by ATLAS in 2017 projected along $\eta$ in reconstructed electrons (gray) and after one (red) and two (blue) iterations of momentum corrections from the $E/p$ method. . . . .   | 38 |
| 328 |      |   |    |
| 329 |      |   |    |
| 330 |      |   |    |
| 331 |      |   |    |
| 332 |      |   |    |
| 333 |      |   |    |
| 334 | 5.1  | Tree-level Feynman diagrams for VBS EWK $VVjj$ production including triple gauge couplings involving $W$ and/or $Z$ bosons (top left and top middle), quartic gauge coupling (top right), or the exchange of a Higgs boson ( $s$ -channel bottom left and $t$ -channel bottom right). The labels are quarks ( $q$ ), fermions ( $f$ ), and gauge bosons ( $V = W, Z$ ). . . . .   | 41 |
| 335 |      |   |    |
| 336 |      |   |    |
| 337 |      |   |    |
| 338 | 5.2  | Tree-level Feynman diagrams for non-VBS EWK $VVjj$ production. The labels are quarks ( $q$ ), fermions ( $f$ ), and gauge bosons ( $V = W, Z$ ). . . . .  | 41 |
| 339 |      |   |    |
| 340 | 5.3  | Tree-level Feynman diagrams for QCD $VVjj$ production. The labels are quarks ( $q$ ), fermions ( $f$ ), and gauge bosons ( $V = W, Z$ ). . . . .  | 41 |
| 341 |      |   |    |
| 342 | 5.4  | Feynman diagrams for VBS EWK production of $W^\pm W^\pm jj$ events. The leftmost diagram contains a quartic gauge coupling vertex, and the rightmost diagram contains an exchange of a Higgs boson. . . . .   | 43 |
| 343 |      |   |    |
| 344 |      |   |    |
| 345 | 5.5  | $W^\pm W^\pm jj$ VBS event topology containing two leptons (1 and 2) with the same electric charge, two neutrinos, and two forward tagging jets (3 and 4) with large rapidity separation $\Delta y$ . . . . .   | 43 |
| 346 |      |   |    |
| 347 |      |   |    |
| 348 | 5.6  | Generator level comparisons at $\sqrt{s} = 8\text{TeV}$ of dijet invariant mass ( $m_{jj}$ , left) and dijet rapidity ( $\Delta y_{jj}$ , right) in EWK (red) and QCD (blue) $W^\pm W^\pm jj$ events. Both data sets have been normalized to the same area. . . . .   | 43 |
| 349 |      |   |    |
| 350 |      |   |    |
| 351 | 5.7  | ATLAS event display of a $pp \rightarrow W^+ W^+ \rightarrow \mu^+ \nu_\mu \mu^+ \nu_\mu jj$ event. The muons are represented by the red lines travelling from the ID through the MS, and the forward jets are represented by the blue cones with yellow energy deposits in the calorimeters. The direction of the $E_T^{\text{miss}}$ in the transverse plane is indicated by the gray dashed line in the inset image. . . . . | 44 |
| 352 |      |   |    |
| 353 |      |   |    |
| 354 |      |   |    |
| 355 |      |   |    |
| 356 | 5.8  | Leading lepton $p_T$ (left) and $\eta$ (right) distributions in the $WZ$ control region before normalization. All lepton channels are combined. . . . .   | 54 |
| 357 |      |   |    |
| 358 | 5.9  | Trilepton invariant mass $m_{lll}$ distribution in the $WZ$ control region before normalization. All lepton channels are combined. . . . .  | 54 |
| 359 |      |   |    |
| 360 | 5.10 | Charge misidentification rates for electrons as a function of $ \eta $ and $p_T$ . Rates are calculated from $Z \rightarrow e^+ e^-$ MC after applying scale factors to approximate the charge mis-ID rates in data. . . . .  | 57 |
| 361 |      |   |    |
| 362 |      |   |    |
| 363 | 5.11 | Dilepton invariant mass distribution $m_{ll}$ for the $ee$ channel in the same-sign inclusive VR. . . . .   | 59 |
| 364 | 5.12 | $p_T$ distributions for the leading (left) and subleading (right) electron for the $ee$ channel in the same-sign inclusive VR. In these plots, the cut requiring $m_{ee}$ to fall within the $Z$ mass window has been inverted in order to test the modelling away from the $Z$ peak. . . . .   | 60 |
| 365 |      |   |    |
| 366 |      |   |    |
| 367 | 5.13 | $\Delta p_T$ distributions for nominal (blue) and loose (red) muons in simulated $t\bar{t}$ events. Each muon has been matched to a truth-level jet. Both distributions are normalized to unit area. . . . .  | 62 |
| 368 |      |   |    |
| 369 |      |   |    |

|     |      |   |    |
|-----|------|---|----|
| 370 | 5.14 | $\Delta p_T$ distributions for muons (top) and electrons (bottom) in simulated $t\bar{t}$ events. Each lepton has been matched to a truth-level jet, and that truth jet has had its $p_T$ corrected to include all truth muons within a cone of $\Delta R < 0.4$ . The nominal leptons are in black. $\Delta p_T$ is calculated for the loose leptons using $p_T$ (red) and $p_T + p_T^{\text{cone}}$ (blue). . . . .   | 63 |
| 371 |      |   |    |
| 372 |      |   |    |
| 373 | 5.15 | Distributions of $p_T^{\text{cone}}/p_T$ for nominal (black) and loose (red) muons in simulated $t\bar{t}$ events. . . . .  | 64 |
| 374 |      |   |    |
| 375 | 5.16 | The measured fake factor as a function of muon $p_T + p_T^{\text{cone}}$ . The error bars represent the statistical uncertainty only. . . . .   | 65 |
| 376 |      |   |    |
| 377 | 5.17 | The measured fake factor as a function of electron $p_T + p_T^{\text{cone}}$ in the central ( $ \eta  < 1.37$ , blue) and forward ( $ \eta  > 1.37$ , red) regions of the detector. The error bars represent the statistical uncertainty only. . . . .  | 66 |
| 378 |      |   |    |
| 379 |      |   |    |
| 380 | 5.18 | Graphical representation of the fake factor application using $p_T + p_T^{\text{cone}}$ . The value of $p_T + p_T^{\text{cone}}$ for the loose lepton is used to “look up” the fake factor weight which is then applied to the event. The loose lepton’s $p_T$ becomes $p_T + p_T^{\text{cone}}$ for the purpose of the fake background estimation. . . . .   | 67 |
| 381 |      |   |    |
| 382 |      |   |    |
| 383 | 5.19 | Systematic variations in the fake factor as a function of muon $p_T + p_T^{\text{cone}}$ . The individual fake factors obtained for each systematic variation are displayed with their statistical uncertainties. . . . .   | 68 |
| 384 |      |   |    |
| 385 |      |   |    |
| 386 | 5.20 | Systematic variations in the fake factor as a function of electron $p_T + p_T^{\text{cone}}$ in the central ( $ \eta  < 1.37$ , top) and forward ( $ \eta  > 1.37$ , bottom) regions of the detector. The individual fake factors obtained for each systematic variation are displayed with their statistical uncertainties. . . . .  | 69 |
| 387 |      |   |    |
| 388 |      |   |    |
| 389 |      |   |    |
| 390 | 5.21 | Distributions of the subleading lepton $p_T$ in the same-sign top fakes VR for $\mu^\pm\mu^\pm$ events (top right), $e^\pm e^\pm$ events (top left), $\mu^\pm e^\pm$ events (bottom left), and all events combined (bottom right). All errors are statistical only. . . . .   | 72 |
| 391 |      |   |    |
| 392 |      |   |    |
| 393 |      |   |    |
| 394 | 5.22 | Pseudorapidity ( $\eta$ ) distributions of truth muons (top) and electrons (bottom) for Sherpa $W^\pm W^\pm jj$ and $WZ$ MC samples. The blue vertical lines represent the allowed $\eta$ range for each lepton flavor. The numbers correspond to the number of raw MC events that fall within and outside of the allowed $\eta$ range for each MC sample. . . . .  | 73 |
| 395 |      |   |    |
| 396 |      |   |    |
| 397 |      |   |    |
| 398 | 5.23 | Distributions of $p_{T,\text{ratio}}(\mu, j)$ for EWK and QCD $W^\pm W^\pm jj$ signal (black) and $WZ$ background (teal) for truth-matched third muons in events that pass the trilepton veto. Both distributions are normalized to unit area. The associated efficiency curves are on the right where efficiency is defined as the percentage of total events that would pass a cut on $p_{T,\text{ratio}}(\mu, j)$ at a given value on the $x$ -axis. . . . . | 73 |
| 399 |      |   |    |
| 400 |      |   |    |
| 401 |      |   |    |
| 402 |      |   |    |
| 403 | 5.24 | Distributions of $\Delta R(\mu, j)$ for EWK and QCD $W^\pm W^\pm jj$ signal (black) and $WZ$ background (teal) for truth-matched third muons in events that pass the trilepton veto. Both distributions are normalized to unit area. The associated efficiency curves are on the right where efficiency is defined as the percentage of total events that would pass a cut on $\Delta R(\mu, j)$ at a given value on the $x$ -axis. . . . .                     | 74 |
| 404 |      |   |    |
| 405 |      |   |    |
| 406 |      |   |    |
| 407 |      |   |    |
| 408 | 5.25 | Distributions of $p_{T,\text{ratio}}(e, j)$ for EWK and QCD $W^\pm W^\pm jj$ signal (black) and $WZ$ background (teal) for truth-matched third electrons in events that pass the trilepton veto. Both distributions are normalized to unit area. The associated efficiency curves are on the right where efficiency is defined as the percentage of total events that would pass a cut on $p_{T,\text{ratio}}(e, j)$ at a given value on the $x$ -axis. . . . . | 74 |
| 409 |      |   |    |
| 410 |      |   |    |
| 411 |      |   |    |
| 412 |      |   |    |
| 413 | 5.26 | Two-dimensional plots of $p_{T,\text{ratio}}(\mu, j)$ vs $\Delta R(\mu, j)$ for truth-matched third muons in events that pass the trilepton veto for EWK and QCD $W^\pm W^\pm jj$ signal (left) and $WZ$ background (right). The blue overlay indicates the area in which the third leptons will pass the custom OR and result in the event failing the trilepton veto. . . . .   | 75 |
| 414 |      |   |    |
| 415 |      |   |    |
| 416 |      |   |    |

|     |  |     |
|-----|--|-----|
| 417 | 5.27 Visual representation of the different kinematic regions relevant to the cross section measurement. The acceptance factor $\mathcal{A}$ converts from the truth level total phase space to the truth level fiducial region, and the efficiency correction $\mathcal{C}$ translates the fiducial region in to the reconstruction level signal region. . . . .  | 79  |
| 421 | 5.28 The dijet invariant mass $m_{jj}$ distributions for data and predicted signal and background in the signal region after the fit. The shaded band represents the statistical and systematic uncertainties added in quadrature. Note that the bins have been scaled such that they represent the number of events per 100 GeV in $m_{jj}$ . The background estimations from the fake factor are included in the “Non-prompt” category, and backgrounds from $V\gamma$ production and electron charge misidentification are combined in the “ $e/\gamma$ conversions” category. Finally, $ZZ$ , $VVV$ , and $t\bar{t}V$ backgrounds are combined in the “Other prompt” category. . . . . | 85  |
| 429 | 5.29 The event yields for data and predicted signal and background in the $WZ$ and low- $m_{jj}$ control regions after the fit. The shaded band represents the statistical and systematic uncertainties added in quadrature. The background estimations from the fake factor are included in the “Non-prompt” category, and backgrounds from $V\gamma$ production and electron charge misidentification are combined in the “ $e/\gamma$ conversions” category. Finally, $ZZ$ , $VVV$ , and $t\bar{t}V$ backgrounds are combined in the “Other prompt” category. . . . .   | 85  |
| 435 | 5.30 Comparison of the measured $W^\pm W^\pm jj$ EWK fiducial cross section with theoretical calculations from SHERPA v2.2.2 and POWHEG-BOX v2. The light orange band represents the total experimental uncertainty on the measured value, and the dark orange hashed band is the statistical uncertainty. For the simulations, the light blue band represents the total theoretical uncertainty, and the dark blue hashed band are the scale uncertainties. The theory predictions do not include the interference between the EWK and QCD production. . . . .  | 87  |
| 442 | 6.1 Comparison of the leading (left) and subleading (right) lepton $p_T$ distributions for purely longitudinal (LL, black) and mixed polarization (LT+TT, cyan) $W^\pm W^\pm jj$ events. . . . .   | 90  |
| 444 | 6.2 Comparison of the azimuthal dijet separation ( $ \Delta\phi_{jj} $ ) for purely longitudinal (LL, black) and mixed polarization (LT+TT, cyan) $W^\pm W^\pm jj$ events. . . . .   | 91  |
| 446 | 6.3 A visual representation of a two-dimensional rectangular grid (left) and a random grid (right) in variables $x$ and $y$ . The signal events are the black circles, and the red squares are the background events. Each intersection of gray dashed lines represents a cut point to be evaluated by the optimization. . . . .   | 96  |
| 450 | 6.4 Leading (top) and subleading (bottom) jet $p_T$ distributions. The default and optimized cuts are represented by the red and green dashed lines, respectively. The $W^\pm W^\pm jj$ EWK signal (black points) is normalized to the same area as the sum of the backgrounds (colored histogram). . . . .  | 99  |
| 454 | 6.5 Lepton-jet centrality distribution. The default and optimized cuts are represented by the red and green dashed lines, respectively. The $W^\pm W^\pm jj$ EWK signal (black points) is normalized to the same area as the sum of the backgrounds (colored histogram). . . . .   | 100 |
| 457 | 6.6 $p_T$ distributions for the leading jet using the default (left) and optimized (right) event selections for all channels combined. . . . .   | 101 |
| 459 | 6.7 $p_T$ distributions for the subleading jet using the default (left) and optimized (right) event selections for all channels combined. . . . .  | 101 |
| 461 | 6.8 $p_T$ distributions for lepton-jet centrality $\zeta$ using the default (left) and optimized (right) event selections for all channels combined. . . . .   | 102 |

---

|     |      |   |     |
|-----|------|---|-----|
| 463 | 6.9  | Projections of the statistical (black), theoretical (blue), systematic (yellow), and total (red) uncertainties on the measured cross section as a function of integrated luminosity using the optimized event selection. . . . .  | 104 |
| 464 | 6.10 | Dijet azimuthal separation ( $ \Delta\phi_{jj} $ ) for the low $m_{jj}$ region ( $520 < m_{jj} < 1100$ GeV, top) and the high $m_{jj}$ region ( $m_{jj} > 1100$ GeV, bottom). The purely longitudinal (LL, gray) is plotted separately from the mixed and transverse (LT+TT, cyan) polarizations. . . . .   | 105 |
| 465 | 6.11 | Projections of the expected longitudinal scattering significance as a function of integrated luminosity when considering all sources of uncertainties (black) or only statistical uncertainties (red). . . . .  | 106 |
| 472 | B.1  | Number of truth particles within $\Delta R < 0.4$ of a selected muon or electron using the ATLAS standard TRUTH1 (left) and the custom TRUTH1++ (right) derivations in $t\bar{t}$ simulation. The complete truth record is stored in the TRUTH1++ derivation, and this is best seen in the first bin, where the lepton has no nearby truth particles. . . . . | 112 |
| 473 | B.2  | Leading lepton $p_T$ distribution. The default and optimized cuts are represented by the red and green dashed lines, respectively. The $W^\pm W^\pm jj$ EWK signal (black points) is normalized to the same area as the sum of the backgrounds (colored histogram). . . . .   | 116 |
| 474 | B.3  | Dilepton invariant mass distribution. The default and optimized cuts are represented by the red and green dashed lines, respectively. The $W^\pm W^\pm jj$ EWK signal (black points) is normalized to the same area as the sum of the backgrounds (colored histogram). . . . .  | 116 |
| 475 | B.4  | Dijet invariant mass distribution. The default and optimized cuts are represented by the red and green dashed lines, respectively. The $W^\pm W^\pm jj$ EWK signal (black points) is normalized to the same area as the sum of the backgrounds (colored histogram). . . . .   | 117 |
| 476 |      |   |     |
| 477 |      |   |     |
| 478 |      |   |     |
| 479 |      |   |     |
| 480 |      |   |     |
| 481 |      |   |     |
| 482 |      |   |     |
| 483 |      |   |     |
| 484 |      |   |     |

---

## Preface

---

486 This thesis presents the major highlights of my work with the ATLAS experiment as a graduate  
487 student at the University of Pennsylvania from Fall of 2013 until early Spring of 2019.

488 The first step of working on the experiment is to complete a *qualification task* in order to be  
489 included on the author list of ATLAS publications. These tasks are an opportunity to contribute  
490 to the experiment as a whole, such as maintaining detector hardware or monitoring physics perfor-  
491 mance. For my qualification task, I worked with the Inner Detector Alignment group which works  
492 to make sure we have accurate knowledge of the locations of each and every sensor in the detector.  
493 My qualification task involved investigating a possible momentum bias in the Monte Carlo (MC)  
494 simulated data. The MC is supposed to be reconstructed with a perfect detector geometry which  
495 should in principle be free of any momentum biases. Ultimately I determined that the size of the  
496 biases were small enough to be negligible compared to what is seen in the real data, and that they  
497 could be corrected for if necessary.

498 My work with the alignment group would continue for the duration of my time here at Penn. In  
499 early 2015, at the start of the LHC’s second data-taking run (Run 2), I worked assisted in validating  
500 the first set of alignment constants using  $\sqrt{s} = 8$  TeV proton-proton collision data. At this point  
501 I took over the responsibility of alignment of the TRT subdetector. The TRT was aligned to high  
502 accuracy in Run 1, and over the course of my time working on alignment, the TRT never required  
503 a straw-by-straw alignment; however it did require a module-level alignment at the end of 2015.  
504 My final responsibility in the alignment group was monitoring momentum biases using the energy-  
505 momentum ratio ( $E/p$ ) of electrons. For the large data reprocessing, the  $E/p$  method served as a  
506 cross check to a similar method using  $Z$  boson events for monitoring and aligning out momentum  
507 biases in the detector. The results from both methods were also used in the uncertainties for the  
508 tracking measurements.

509 On the analysis side, I had previous experience in Standard Model (SM) electroweak physics  
510 from my time as an undergraduate at Duke University, and it remained a point of interest for  
511 me in graduate school. As such, I was happy to work with fellow Penn students on the cross  
512 section measurement of SM  $WZ$  diboson production with the early  $\sqrt{s} = 13$  TeV ATLAS data.  
513 My contribution to the analysis was primarily on the software side, as I maintained and updated  
514 the analysis framework. While the  $WZ$  measurement is not covered by this thesis, it provided me  
515 with invaluable analysis experience in electroweak physics, as well as a detailed understanding of a  
516 major background to many diboson processes. The results for this analysis can be found published  
517 in Physics Letters B in 2016 [1].

518 The final two analyses I worked on involve the scattering of same-sign  $W$  bosons, and they make  
519 up the majority of this thesis. The first analysis is a measurement of the  $W^\pm W^\pm jj$  cross section  
520 at  $\sqrt{s} = 13$  TeV. This measurement along with that of the CMS collaboration represent the first  
521 observation of the  $W^\pm W^\pm jj$  scattering process. My primary contribution to the analysis is in the  
522 estimation of the fake lepton background, where we implemented a brand new version of the fake  
523 factor method using particle isolation variables. I also did a preliminary study of the interference  
524 between electroweak and strong production of  $W^\pm W^\pm jj$  events, assisted in the production of private  
525 data samples for use with the analysis framework, and used my familiarity with the  $WZ$  process  
526 to optimize the rejection of the background. Ultimately the majority of the  $WZ$  rejection was not  
527 included in the final result; however, it is still covered in the thesis in the hopes that it will be useful  
528 for similar analyses in the future. The formal publication for this measurement will likely be coming  
529 out within the next few months.

530 The second  $W^\pm W^\pm jj$  analysis is a study on the prospects for a measurement of the process at the  
531 upgraded High-Luminosity LHC, scheduled to begin operation in 2026. Here my main contribution  
532 was an optimization of the event selection using a Random Grid Search algorithm. Through the  
533 optimization we expect to take advantage of the higher center of mass energy and greater volume of  
534 data and tighten certain selection cuts to increase the strength of the  $W^\pm W^\pm jj$  signal. In addition, I  
535 once again maintained and updated the analysis framework and produced the group's data samples,  
536 and I also developed a truth-based particle isolation criteria in order to reduce contributions from  
537 backgrounds involving the top quark. The results of this prospects study will be published as a part  
538 of the annual Yellow Report for the High-Luminosity LHC.

Will K. DiClemente  
Philadelphia, February 2019

540

## CHAPTER 1

---

541

### Introduction

---

542 This thesis focuses on

543        TODO: Make sure to mention previous ATLAS measurements of QGC's (wgg and 8 tev sww)  
544        in brief discussion of why these diboson processes are interesting

## CHAPTER 2

---

# Theoretical Framework

---

547 This chapter outlines the theoretical groundwork for the rest of the thesis. An overview of the Stan-  
 548 dard Model of particle physics (SM) is given in Section 2.1, followed by the electroweak symmetry  
 549 breaking mechanism involving the Higgs boson in Section 2.2. Finally, Section 2.3 will go into some  
 550 detail on the interests of vector boson scattering (VBS) specifically.

551 **2.1 Introduction to the Standard Model**

552 The Standard Model of particle physics serves as a mathematical description of the fundamental  
 553 particles of the universe and their interactions. It has been developed over the course of the past  
 554 century, incorporating both predictions from theory and results from experiments. All in all, the SM  
 555 has proven remarkably successful in accurately describing particle interactions seen in experiments.

556 The SM is a quantum field theory (QFT) [2, 3] in which the fundamental particles are represented  
 557 as excited states of their corresponding fields. The spin- $\frac{1}{2}$  fermionic fields give rise to the quarks  
 558 and leptons comprising ordinary matter, the spin-1 fields correspond to the electroweak bosons and  
 559 the gluon which mediate the electroweak and strong forces, respectively, and finally the scalar Higgs  
 560 field is responsible for electroweak symmetry breaking. The excitations and interactions of the fields  
 561 are governed by the SM Lagrangian, which is invariant under local transformations of the group  
 562  $SU(3) \times SU(2) \times U(1)$ . **TODO: need more detail/refinement here**

563 The first quantum field theory to be developed is quantum electrodynamics (QED) [4], which  
 564 describes the electromagnetic interaction. The theory predicts the existence of a  $U(1)$  gauge field  
 565 that interacts with the electrically charged fermions. This field corresponds to the photon. A key  
 566 aspect of QED is that it is perturbative. The coupling constant  $\alpha = e^2/4\pi$  is small, where  $e$  is

567 electrical charge of the field, allowing for the use of perturbation theory in calculations. In this case,  
 568 calculations can be written as a power series in  $\alpha$ , where successive higher order terms contribute  
 569 less to the final result. **TODO: renormalizability here?**

570 The strong interaction—the theory of quarks and gluons—has also been described using QFT  
 571 as quantum chromodynamics (QCD). The symmetry group for QCD is  $SU(3)$ , and its eight gen-  
 572 erators correspond to the eight differently charged, massless gluons [5]. Unlike in QED, which has  
 573 positive and negative charges, the strong force has three “colors”. Color charge combined with the  
 574 non-Abelian nature of  $SU(3)$ , which allows the gluons to interact with each other, result in the  
 575 most well-known property of QCD: color confinement. In order to increase the separation between  
 576 two color-charged quarks, the amount of energy required increases until it becomes energetically  
 577 favorable to pair-produce a new quark-antiquark pair, which then bind to the original quarks. The  
 578 end result of this is that only color-neutral objects exist in isolation. What this means for the strong  
 579 coupling constant  $\alpha_s$  is that its value at the low energies where confinement occurs is large, on  
 580 the order of  $\alpha_s \sim 1$ . The consequence of this is that perturbation theory cannot be used to accu-  
 581 rately approximate interactions. While this appears at first to be a critical problem for predictions,  
 582 fortunately it turns out that  $\alpha_s$  “runs”, or decreases in magnitude at higher energy [6, 7]. This so-  
 583 called “asymptotic freedom” allows QCD to be calculated perturbatively [8] at energies accessible  
 584 by collider experiments including the LHC.

585 The last gauge field corresponds to the weak interaction. Ultimately, the weak  $SU(2)$  and the  
 586 electromagnetic  $U(1)$  mix to form the  $SU(2) \times U(1)$  *electroweak* (EWK) interaction [9, 10]. A  
 587 more detailed description of the mixing will be discussed in conjunction with electroweak symmetry  
 588 breaking (EWSB) in Section 2.2; however, a summary of the resulting EWK interaction is presented  
 589 here, at the risk of some repeated information to follow. There are three weak isospin bosons arising  
 590 from the  $SU(2)$  group ( $W_\mu^1$ ,  $W_\mu^2$ , and  $W_\mu^3$ ) and one weak hypercharge boson from the  $U(1)$  group  
 591 ( $B_\mu$ ). The  $W_3$  and  $B$  bosons mix according to the weak mixing angle  $\theta_W$  to form the  $Z$  boson and  
 592 the photon according to:

$$\begin{pmatrix} \gamma \\ Z \end{pmatrix} = \begin{pmatrix} \cos \theta_W & \sin \theta_W \\ -\sin \theta_W & \cos \theta_W \end{pmatrix} \begin{pmatrix} B_\mu \\ W_\mu^3 \end{pmatrix} \quad (2.1)$$

593 The value of  $\theta_W$  is not predicted by the SM; it is one example of an experimental input to the  
 594 theory, measured to be  $\sin^2 \theta_W = 0.23153 \pm 0.00016$  [11]. The charged  $W^\pm$  bosons are a mixture of  
 595 the remaining  $W_\mu^1$  and  $W_\mu^2$  bosons:

$$W^\pm = \frac{1}{\sqrt{2}}(W_\mu^1 \mp iW_\mu^2) \quad (2.2)$$

596 Unlike the photon (and the gluon of QCD), the  $W^\pm$  and  $Z$  bosons are massive. This means that  
 597 even though SU(2) is non-Abelian, the range of interaction is short and confinement does not occur.  
 598 Lastly, the EWK interaction is chiral, only coupling to the left-handed component of the fermion  
 599 fields

600 One final field remains within the SM: the scalar Higgs field. It was originally proposed in the  
 601 1960's to explain the masses of the  $W^\pm$  and  $Z$  bosons [12, 13, 14] and is the mechanism for the  
 602 EWSB process. The particle associated with the field is a massive scalar boson, which was at last  
 603 discovered by ATLAS and CMS in 2012 [15, 16] with a mass of 125 GeV.

## 604 2.2 Electroweak symmetry breaking and the Higgs boson

605 The results of electroweak mixing and the implications of the Higgs field have been introduced  
 606 in the previous section. If the EWK theory were an unbroken symmetry, the associated  $W^\pm$  and  
 607  $Z$  bosons would be massless; however, when observed experimentally, they were found to be quite  
 608 heavy [17, 18], at around 80 GeV and 91 GeV, respectively [19]. Here, a more detailed explanation  
 609 of the Higgs mechanism and how it “spontaneously breaks” the EWK symmetry, resulting in the  
 610 three massive bosons ( $W^\pm$  and  $Z$ ) and one massless boson (photon), is presented.

611 To see how the Higgs mechanism results in the massive vector bosons and a massless photon,  
 612 consider the following. Beginning with a complex scalar doublet  $\phi$  defined as:

$$\phi = \begin{pmatrix} \phi^+ \\ \phi^0 \end{pmatrix} = \sqrt{\frac{1}{2}} \begin{pmatrix} \phi_1 + i\phi_2 \\ \phi_3 + i\phi_4 \end{pmatrix} \quad (2.3)$$

613 a Lagrangian  $\mathcal{L}$  can be written:

$$\mathcal{L} = (\mathcal{D}_\mu \phi)^\dagger (\mathcal{D}^\mu \phi) - \mu^2 \phi^\dagger \phi - \lambda(\phi^\dagger \phi)^2 \quad (2.4)$$

614 where  $\lambda > 0$  and  $\mathcal{D}_\mu$  is the covariant derivative.  $\mathcal{D}_\mu$  is defined such that  $\mathcal{L}$  is invariant under a local  
 615 SU(2)  $\times$  U(1) gauge transformation:

$$\mathcal{D}_\mu \phi = \left( \partial_\mu + \frac{ig}{2} \tau_a W_\mu^a + \frac{ig'}{2} B_\mu \right) \phi \quad (2.5)$$

616 where  $W_\mu^a$  ( $a = 1, 2, 3$ ) are the SU(2) fields with generators  $\tau_a$  and coupling constant  $g$ , and  $B_\mu$  is  
 617 the U(1) field with coupling constant  $g'$ .

618 Isolating the potential term:

$$V(\phi) = \mu^2 \phi^\dagger \phi + \lambda(\phi^\dagger \phi)^2 \quad (2.6)$$

619 a choice must be made on the sign of  $\mu^2$ , and the case of interest is for  $\mu^2 < 0$ . This results in  
 620 the famous “mexican hat potential” shown in Figure 2.1, which is minimized along the collection of  
 621 points:

$$\phi^\dagger \phi = \frac{1}{2} (\phi_1^2 + \phi_2^2 + \phi_3^2 + \phi_4^2) = -\frac{\mu^2}{2\lambda} \quad (2.7)$$

622 This means that the minimum of the potential is not at  $\phi = 0$  (as it would be in the case where  
 623  $\mu^2 > 0$ ), but rather at a value:

$$v \equiv \sqrt{-\frac{\mu^2}{\lambda}} \quad (2.8)$$

624 With no loss of generality due to the SU(2) symmetry,  $\phi_1 = \phi_2 = \phi_4 = 0$  can be imposed on  
 625 Equation 2.7 leaving  $\phi_3^2 = v^2$ . Finally, the *vacuum expectation value* (VEV) of the field can be  
 626 written as:

$$\langle \phi \rangle = \sqrt{\frac{1}{2}} \begin{pmatrix} 0 \\ v \end{pmatrix} \quad (2.9)$$

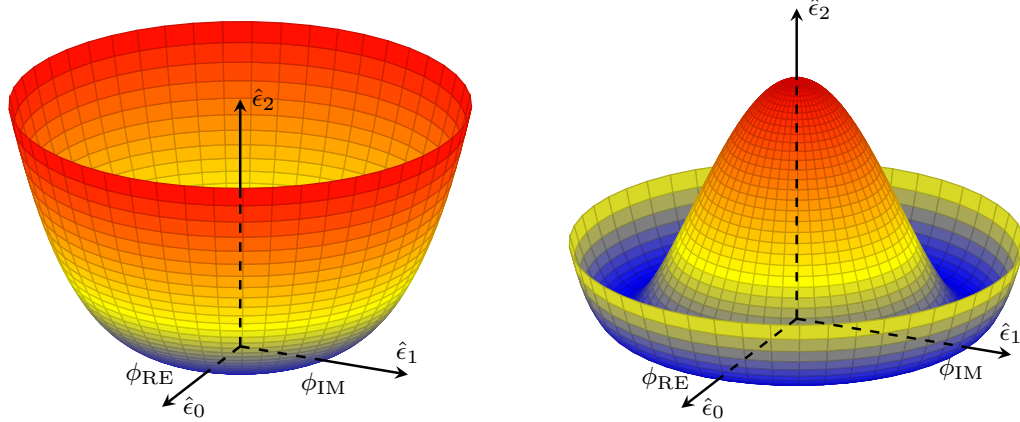


Figure 2.1: An illustration of the potential term  $V(\phi)$  in the cases where  $\mu^2 > 0$  (left) and  $\mu^2 < 0$  (right). The right-hand plot shows the Higgs potential, or “Mexican hat potential”, with the minimum at  $|\phi| = \sqrt{-\frac{\mu^2}{\lambda}}$  rather than at  $|\phi| = 0$  as in the left-hand plot.

627 The VEV can be substituted back into the original Lagrangian in Equation 2.4, and, following  
 628 quite a bit of math, a collection of mass terms can be identified:

$$\mathcal{L} \subset \mathcal{L}_M \equiv \frac{1}{8} v^2 g^2 \left[ (W_\mu^1)^2 + (W_\mu^2)^2 \right] + \frac{1}{8} v^2 \left[ g^2 (W_\mu^3)^2 - 2gg' W_\mu^3 B^\mu + g'^2 (B_\mu)^2 \right] \quad (2.10)$$

629 Focusing on the first term for the moment, substituting in Equation 2.2 for the physical  $W^\pm$  bosons,  
 630 the mass term can be seen clearly:

$$M_W^2 W^+ W^- = \left(\frac{1}{2}vg\right)^2 W^+ W^- \quad (2.11)$$

631

$$M_W = \frac{1}{2}vg \quad (2.12)$$

632 With a bit of clever forward-thinking, the second term of Equation 2.10 can be rewritten as:

$$\frac{1}{8}v^2 \left[ gW_\mu^3 - g'B_\mu \right]^2 + 0 \left[ g'W_\mu^3 - gB_\mu \right]^2 = \frac{1}{2}M_Z^2 Z_\mu^2 + \frac{1}{2}M_A^2 A_\mu^2 \quad (2.13)$$

633 where  $Z_\mu^2$  and  $A_\mu^2$  represent the physical  $Z$  boson and photon, respectively, and are defined as:

$$Z_\mu = \frac{gW_\mu^3 - g'B_\mu}{\sqrt{g^2 + g'^2}} \quad (2.14)$$

634

$$A_\mu = \frac{g'W_\mu^3 - gB_\mu}{\sqrt{g^2 + g'^2}} \quad (2.15)$$

635 From this, it can be seen that the photon is massless, and the mass of the  $Z$  boson is identified as:

$$M_Z = \frac{1}{2}v\sqrt{g^2 + g'^2} \quad (2.16)$$

636 Lastly, the Higgs field can couple directly to the fermions. Taking the electron as an example,  
 637 an additonal Lagrangian term can be written:

$$\mathcal{L}_e = -G_e [\bar{e}_L \phi e_R + \bar{e}_R \phi^\dagger e_L] \quad (2.17)$$

638 where  $e_L$  and  $e_R$  are the left-handed doublet and right-handed singlet, respectively, and  $\phi$  is as in  
 639 Equation 2.3. The symmetry can be spontaneously broken by a perturbation about the VEV:

$$\phi = \sqrt{\frac{1}{2}} \begin{pmatrix} 0 \\ v + h(x) \end{pmatrix} \quad (2.18)$$

640 which, when substituted into  $\mathcal{L}_e$  gives:

$$\begin{aligned} \mathcal{L}_e &= -\frac{G_e}{\sqrt{2}}v(\bar{e}_L e_R + \bar{e}_R e_L) - \frac{G_e}{\sqrt{2}}(\bar{e}_L e_R + \bar{e}_R e_L)h \\ &= -m_e \bar{e}e - \frac{m_e}{v} \bar{e}eh \end{aligned} \quad (2.19)$$

641 for electron mass  $m_e = \frac{G_e v}{\sqrt{2}}$ . From the second term, it can be seen that the strength of the Higgs  
 642 coupling to the electron is proportional to the mass of the electron. The rest of the fermion couplings  
 643 follow from this example.

644 What is accomplished here is quite remarkable. The weak and electromagnetic interactions have  
 645 been unified into a single  $SU(2) \times U(1)$  interaction, and the physical bosons observed in nature arise  
 646 as mixtures of the four gauge fields. Three of the four degrees of freedom in the scalar field  $\phi$  of  
 647 Equation 2.3, are absorbed by the  $W^\pm$  and  $Z$  bosons, and the fourth generates the Higgs boson.  
 648 Additionally, it is shown that the Higgs couples to fermions in proportion to their mass. From  
 649 experimental measurements, the value of the VEV has been determined to be  $v \approx 246$  GeV [19].  
 650 However, it should be noted that the theory does not predict the mass of the Higgs boson or of the  
 651 fermions; these must all be determined from experiment.

### 652 2.3 Vector boson scattering in the Standard Model

653 Due to the non-Abelian nature of the EWK interaction, the associated gauge bosons are allowed  
 654 to self-interact. This results in triple and quartic couplings of gauge bosons (TGCs and QGCs,  
 655 respectively). The SM allowed TGCs are the  $WW\gamma$  and  $WWZ$  vertices, which can be measured  
 656 experimentally via diboson production or through vector boson fusion (VBF). QGCs predicted by the  
 657 model include  $WWZ\gamma$ ,  $WW\gamma\gamma$ ,  $WWZZ$ , and  $WWWW$  vertices accessible in triboson production  
 658 or via vector boson scattering (VBS)<sup>1</sup> [20]. VBS processes are defined by a  $VV \rightarrow VV$  signature,  
 659 where  $V$  represents one of the EWK gauge bosons ( $W^\pm$ ,  $Z$ , or  $\gamma$ ), as shown in Figure 2.2. The actual  
 660 interaction between the incoming and outgoing vector bosons can be mediated by the exchange of  
 661 a virtual  $V$  or directly via a QGC (as in Figure 2.3), or by the exchange of a Higgs boson (as in  
 662 Figure 2.4).

663 As detailed in the previous section, the Higgs mechanism produces three Goldstone bosons and a  
 664 Higgs boson. The Goldstone bosons are then “eaten” by the physical gauge bosons, giving them mass  
 665 and consequently a longitudinal polarization<sup>2</sup>. In fact, according to the Electroweak Equivalence  
 666 Theorem, the high-energy interactions of longitudinal gauge bosons can be accurately described by  
 667 the Goldstone bosons of the EWSB mechanism [21]. Thus, the scattering of the massive gauge  
 668 bosons are inextricably linked to EWSB.

669 It turns out that without a light SM Higgs boson, the scattering amplitude of longitudinally  
 670 polarized vector bosons grows with center-of-mass energy and ultimately violates unitarity above

---

<sup>1</sup>Vector boson fusion and scattering typically refer to the  $s$ -channel and  $t$ -channel exchanges of a vector boson, respectively. Since both deal with a similar  $VV \rightarrow VV$  process, for the remainder of this thesis, *vector boson scattering* will refer to both VBF and VBS.

<sup>2</sup>A massless spin-1 boson can have one of two transverse polarization states, while a massive spin-1 boson can also be longitudinally polarized. As a result, only the massive  $W^\pm$  and  $Z$  bosons, and not the massless photon, are sensitive to EWSB.

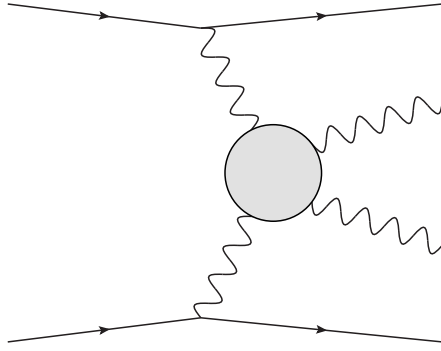


Figure 2.2: Feynman diagram of a generic VBS process. The gray circle represents any interaction with two incoming and two outgoing vector bosons, including any of the diagrams shown in Figures 2.3 and 2.4.

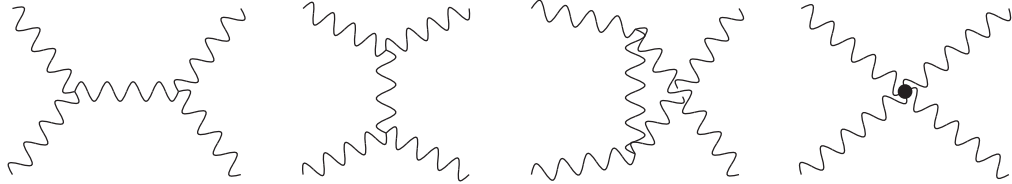


Figure 2.3: Leading order  $VV \rightarrow VV$  Feynman diagrams involving EWK bosons, from right to left:  $s$ -channel,  $t$ -channel,  $u$ -channel, and the quartic gauge coupling.

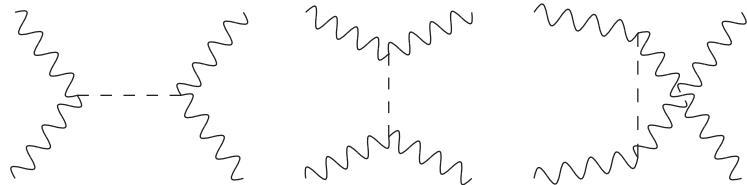


Figure 2.4: Leading order  $VV \rightarrow VV$  Feynman diagrams involving the exchange of a Higgs boson, from right to left:  $s$ -channel,  $t$ -channel, and  $u$ -channel.

671     $\sqrt{s} \approx 1.2$  [22, 23]. Writing down the equations for the transverse and longitudinal polarization  
 672    vectors for a gauge boson of mass  $M_V$  [24]:

$$\epsilon_{\pm}^{\mu} = \frac{1}{\sqrt{2}}(0, 0, \pm i, 0) \quad (2.20)$$

673

$$\begin{aligned} \epsilon_L^{\mu} &= \frac{1}{M_V}(|\vec{p}|, 0, 0, E) \\ &= \frac{p^{\mu}}{M_V} + v^{\mu} \end{aligned} \quad (2.21)$$

674    where  $v^{\mu}$  is of the order  $M_V/E$  and becomes small in the high energy limit, it can be seen that

675  $\epsilon_L^\mu$  grows with the momentum of the boson  $p^\mu$ . Therefore, the dominant contribution to the VBS  
 676 process at high energy comes from the longitudinally polarized gauge bosons [25].

677 The high-energy behavior of longitudinally polarized vector boson scattering can be explored in  
 678 the case of opposite-sign  $W^+W^- \rightarrow W^+W^-$  scattering. In the high-energy limit ( $s \gg M_W^2, M_H^2$ ),  
 679 the amplitude of  $W^+W^-$  scattering without considering the Higgs contributions (the relevant dia-  
 680 grams in Figure 2.3) can be written as [23]:

$$\mathcal{M}_{\text{gauge}} = -\frac{g^2}{4M_W^2} u + \mathcal{O}(1) \quad (2.22)$$

681 where  $g$  is the EWK coupling and  $u$  is one of the Mandelstam variables (the others being  $s$  and  
 682  $t$ ). The  $\mathcal{O}(E^4)$  terms cancel out between the TGC and QGC diagrams [25]. What is left is an  
 683 amplitude proportional to  $E^2$  that diverges as  $E/M_W \rightarrow \infty$ . **TODO: what is the latex symbol for**  
 684 **infinity** However, the amplitude from the diagrams involving the Higgs boson (the relevant diagrams  
 685 in Figure 2.4) is:

$$\mathcal{M}_{\text{Higgs}} = -\frac{g^2}{4M_W^2} \left[ \frac{(s - M_W^2)^2}{s - m_H^2} + \frac{(t - M_W^2)^2}{t - M_H^2} \right] \quad (2.23)$$

686 which, in the high-energy limit, reduces to:

$$\mathcal{M}_{\text{Higgs}} = \frac{g^2}{4M_W^2} u + \mathcal{O}(1) \quad (2.24)$$

687 Adding the two equations together cancels out the  $E^2$  term and leaves only terms constant in  
 688 energy. Therefore, with a SM Higgs, the scattering amplitude for longitudinally polarized  $W$  bosons  
 689 no longer diverges. Plots of the cross section of several  $VV \rightarrow VV$  scattering processes are shown  
 690 in Figure 2.5 with and without a SM Higgs boson.

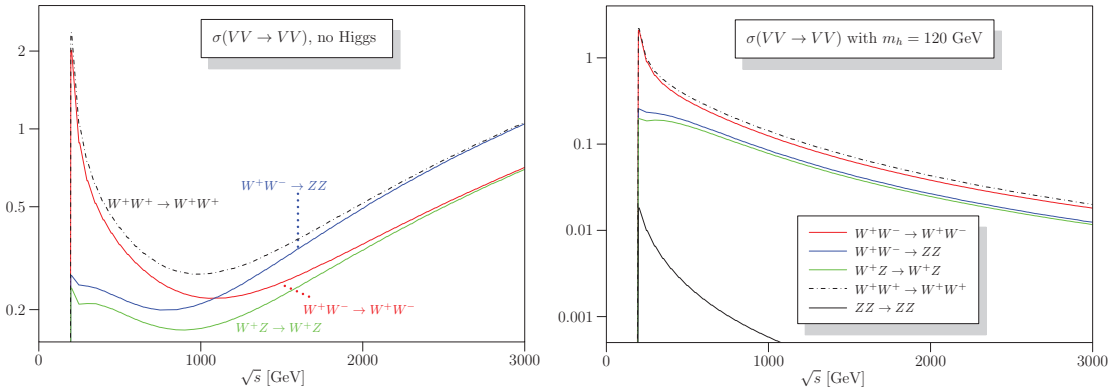


Figure 2.5: Cross sections in nanobarns for five different scattering processes of longitudinally polarized vector bosons as a function of center of mass energy  $\sqrt{s}$ . Without a SM Higgs boson (left), the cross sections grow unbounded with  $\sqrt{s}$ ; however with a 120 GeV Higgs boson (right), the cross sections no longer diverge. Plots taken from [26].

691

## CHAPTER 3

692

# LHC and the ATLAS Detector

693 **3.1 The Large Hadron Collider**

694 The Large Hadron Collider (LHC) [27] is...

695 **3.2 The ATLAS Detector**

696 ATLAS is a general-purpose particle detector...

697 **3.2.1 The Inner Detector**

698 The Inner Detector serves the primary purpose of measuring the trajectories of charged particles...

699 **3.2.1.1 Pixel Detector**

700 The Pixel detector consists of four cylindrical barrel layers and three disk-shaped endcap layers...

701 **3.2.1.2 Semiconductor Tracker**

702 The Semiconductor Tracker uses the same basic technology as the Pixels, but the fundamental unit  
703 of silicon is a larger “strip”...

704 **3.2.1.3 Transition Radiation Tracker**

705 The Transition Radiation Tracker is the outermost component of the ID...

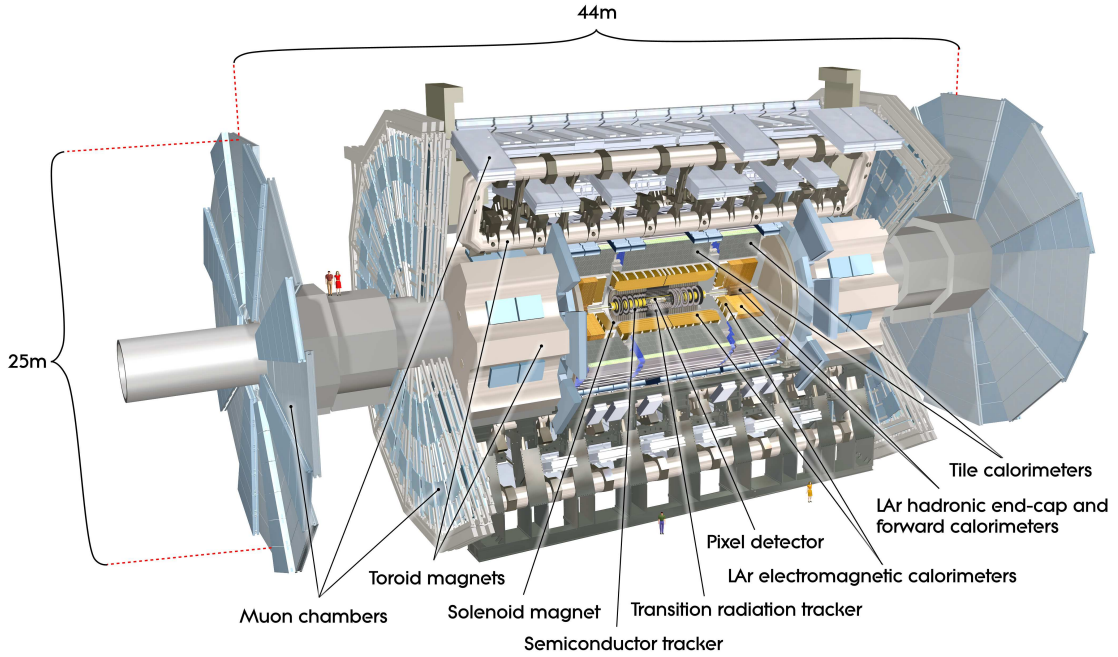


Figure 3.1: General cut-away view of the ATLAS detector [28].

### 706 3.2.2 The Calorimeters

707 ATLAS includes two types of calorimeter system for measuring electromagnetic and hadronic showers. These are the Liquid Argon (LAr) calorimeters and the Tile calorimeters. Together, these cover  
 708 the region with  $|\eta| < 4.9\dots$

#### 710 3.2.2.1 Liquid Argon Calorimeters

711 The Liquid Argon system consists of...

#### 712 3.2.2.2 Tile Calorimeters

713 The Tile calorimeter provides coverage for hadronic showers...

### 714 3.2.3 The Muon Spectrometer

715 Muon spectrometer stuff.

<sup>716</sup> **3.2.4 Particle reconstruction**

<sup>717</sup> Particle reconstruction algorithms

<sup>718</sup> **3.2.4.1 Track reconstruction**

<sup>719</sup> **3.2.4.2 Muon reconstruction**

<sup>720</sup> **3.2.4.3 Electron reconstruction**

<sup>721</sup> **3.2.4.4 Jet reconstruction**

## CHAPTER 4

---

# 723 Alignment of the ATLAS Inner Detector

---

724 When a charged particle passes through the ATLAS ID, it leaves hits in the sensors along its path.  
725 In order to accurately measure the track of the particle, it is necessary to know where these hits  
726 occurred as precisely as possible, which in turn requires knowledge of the physical location of the  
727 element that registered the hit. If one of these elements is *misaligned*, or displaced relative to its  
728 position in the known detector geometry, the assumed location of the corresponding hit will not  
729 match its actual location, resulting in an incorrect track fit. These misalignments can occur for  
730 any number of reasons, including but not limited to elements shifting during maintenance periods  
731 or cycles in ATLAS’s magnetic field, or small movements during normal detector operations. The  
732 effect of a misaligned detector element on the track reconstruction is shown in Figure 4.1.

733 In order to correct the misalignments, the ID alignment procedure is applied to accurately  
734 determine the physical position and orientation of each detector element. The baseline accuracy of  
735 the alignment is required to be such that the track parameter resolutions are not degraded by more  
736 than 20% with respect to those derived from a perfect detector geometry<sup>3</sup>. This corresponds to a  
737 precision of better than  $10\mu\text{m}$  in the positioning of the elements of the silicon detectors [29].

738 This chapter outlines the ID alignment procedure, the alignment of the detector during the 2015  
739 data taking period, and the steps taken to measure momentum biases in the alignment.

---

<sup>3</sup>The so-called *perfect geometry* refers to the description of the ATLAS detector in which every sensor precisely matches its design specifications. The perfect geometry contains no misalignments, and the position of each sensor is known exactly.

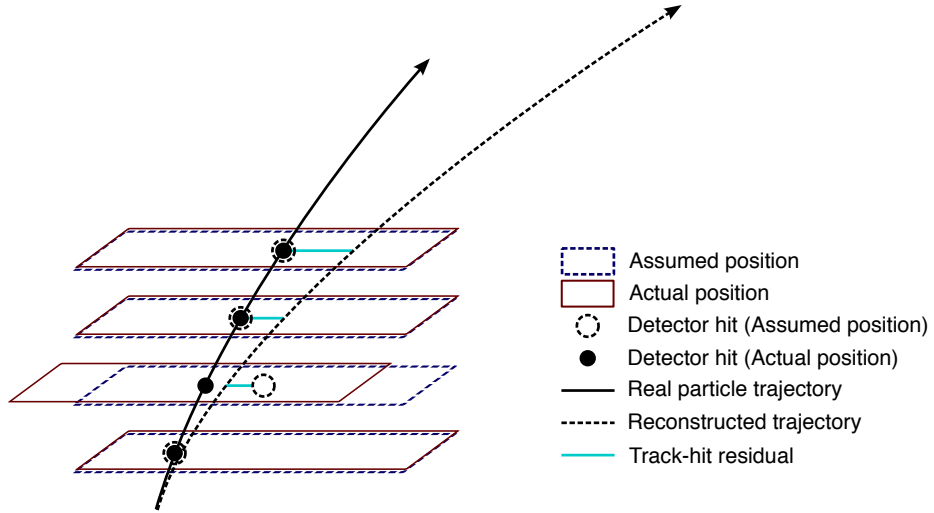


Figure 4.1: Graphical representation of the effect of a misaligned detector element. The reconstructed particle track (dashed arrow) differs from the actual trajectory of the particle (solid arrow) due to the shift in one of the detector elements. The cyan lines represent the track-to-hit residuals.

#### 740 4.1 The alignment method

741 The alignment procedure uses track-based algorithm that updates the locations of detector elements  
 742 in order to minimize the set of track-hit *residuals*. These residuals are defined as the distance between  
 743 the fitted track position in a given detector element to the position of the hit recorded by the same  
 744 element, and are shown by the cyan lines in Figure 4.1. Tracks in ATLAS are parameterized as  
 745 five-dimensional vectors [30]:

$$\vec{\tau} = (d_0, z_0, \phi_0, \theta, q/p) \quad (4.1)$$

746 where  $d_0$  and  $z_0$  are the transverse and longitudinal impact parameters with respect to the origin,  
 747 respectively,  $\phi_0$  is the azimuthal angle of the track at the point of closest approach to the origin,  $\theta$   
 748 is the polar angle, and  $q/p$  is the charge of the track divided by its momentum. The residual for the  
 749  $i^{\text{th}}$  hit of a given track can then be written in terms of the track parameters  $\vec{\tau}$  and a set of alignment  
 750 parameters  $\vec{a}$  that describe the hit location [31]:

$$r_i(\vec{\tau}, \vec{a}) = (\vec{m}_i - \vec{e}_i(\vec{\tau}, \vec{a})) \cdot \hat{k} \quad (4.2)$$

751 where  $\vec{e}_i$  is the intersection point of the extrapolated track with the sensor,  $\vec{m}_i$  is the position of the  
 752 associated hit within the sensor, and  $\hat{k}$  is the unit vector defining the direction of the measurement  
 753 within the sensor.  $\vec{r}$  is then the vector of residuals for the given track.

754 A  $\chi^2$  function can be built from the residuals of all collected tracks:

$$\chi^2 = \sum_{\text{tracks}} \vec{r}^T V^{-1} \vec{r} \quad (4.3)$$

755 where  $V$  is the covariance matrix of the hit measurements. The  $\chi^2$  function is then minimized with  
 756 respect to the alignment parameters  $\vec{a}$ , which contain all degrees of freedom being aligned. The  
 757 minimization condition with respect to  $\vec{a}$  is:

$$\frac{d\chi^2}{d\vec{a}} = 0 \rightarrow 2 \sum_{\text{tracks}} \left( \frac{d\vec{r}}{d\vec{a}} \right)^T V^{-1} \vec{r} = 0 \quad (4.4)$$

758 This equation can be difficult to solve exactly, so the residual is rewritten as a first order Taylor  
 759 expansion:

$$\vec{r} = \vec{r}_0 + \frac{d\vec{r}}{d\vec{a}} \delta\vec{a} \quad (4.5)$$

760 where  $\vec{r}_0$  is dependent on an initial set of track and alignment parameters  $\vec{r}_0$  and  $\vec{a}_0$ , respectively;  
 761 the track parameter dependence has also been folded into the total derivative  $\frac{d\vec{r}}{d\vec{a}}$ . Equation 4.5 can  
 762 then be inserted into the minimization condition from Equation 4.4 to give:

$$\left[ \sum_{\text{tracks}} \left( \frac{d\vec{r}}{d\vec{a}} \right)^T V^{-1} \left( \frac{d\vec{r}}{d\vec{a}} \right) \right] \delta\vec{a} + \sum_{\text{tracks}} \left( \frac{d\vec{r}}{d\vec{a}} \right)^T V^{-1} \vec{r}_0 = 0 \quad (4.6)$$

763 From this equation, the alignment matrix  $\mathcal{M}_a$  and alignment vector  $\vec{\nu}_a$  can be defined:

$$\mathcal{M}_a = \sum_{\text{tracks}} \left( \frac{d\vec{r}}{d\vec{a}} \right)^T V^{-1} \left( \frac{d\vec{r}}{d\vec{a}} \right) \quad (4.7)$$

764

$$\vec{\nu}_a = \sum_{\text{tracks}} \left( \frac{d\vec{r}}{d\vec{a}} \right)^T V^{-1} \vec{r}_0 \quad (4.8)$$

765 Finally, the alignment corrections  $\delta\vec{a}$  can be solved for by inverting the alignment matrix:

$$\delta\vec{a} = -\mathcal{M}_a^{-1} \vec{\nu}_a \quad (4.9)$$

766 which is a linear system of equations with a number of equations equal to the number of alignment  
 767 degrees of freedom [32].

768 Inverting the matrix and solving this system of equations is referred to as *Global  $\chi^2$*  align-  
 769 ment [31]. This can be useful, as  $\mathcal{M}_a$  contains all the correlations between the alignable structures.  
 770 However, inverting the matrix becomes difficult when the number of degrees of freedom becomes  
 771 large, and as the number of alignable structures increases, so too does the size of the matrix  $\mathcal{M}_a$ .  
 772 Eventually inverting the matrix becomes too computationally intensive to be practical.

773 This problem is solved by the *Local*  $\chi^2$  algorithm [33]. In this case, the alignment matrix is  
 774 constructed to be block-diagonal, allowing for it to be inverted even for large numbers of degrees of  
 775 freedom. This is achieved by replacing the full derivative in Equation 4.6 with the partial derivative  
 776  $\frac{\partial \vec{r}}{\partial \vec{a}}$ . The new alignment matrix  $\mathcal{M}'_a$  and alignment vector  $\vec{\nu}'_a$  become:

$$\mathcal{M}_a = \sum_{\text{tracks}} \left( \frac{\partial \vec{r}}{\partial \vec{a}} \right)^T V^{-1} \left( \frac{\partial \vec{r}}{\partial \vec{a}} \right) \quad (4.10)$$

$$\vec{\nu}_a = \sum_{\text{tracks}} \left( \frac{\partial \vec{r}}{\partial \vec{a}} \right)^T V^{-1} \vec{r}_0 \quad (4.11)$$

777 Inverting  $\mathcal{M}'_a$  is considerably faster and less intensive even for large numbers of degrees of freedom;  
 778 however, the correlations between the alignable structures is lost.

780 Due to the Taylor expansion used in Equation 4.6, several iterations of the alignment algorithm  
 781 may be necessary to converge on a final set of alignment constants. The Local  $\chi^2$  alignment typically  
 782 requires more iterations due to the loss of the correlation information [34]. In practice, the ATLAS  
 783 reconstruction is run over a set of events, and the resulting tracks are fed to the alignment algorithm.  
 784 The residuals are calculated, the alignment matrix is built and inverted, and a new set of alignment  
 785 constants is obtained. The convergence of the alignment can be checked by:

786 1. Measure the  $\Delta\chi^2$  with the previous iteration. If it is near zero, then the  $\chi^2$  is approaching its  
 787 minimum.

788 2. Looking at the residual distributions for different alignable structures. A well aligned detector  
 789 will have a mean residual of zero with a width approximating the intrinsic resolution of the  
 790 detector.

791 If the above checks are satisfied, the process is finished and the final alignment constants are read  
 792 out; if not, another iteration is performed. A visual representation of the alignment chain is shown  
 793 in Figure 4.2.

794 Since a  $\chi^2$  minimization is used to align the detector, if there is a systematic misalignments in  
 795 the detector that does not adversely affect the  $\chi^2$ , the algorithm will be insensitive to it. These  
 796 misalignments are referred to as *weak modes*, and special care is taken to remove them [35]. One  
 797 potential impact of weak modes is a bias in the track momentum of reconstructed particles. This  
 798 particular effect is the subject of Section 4.4.

799 In practice, the detector is aligned both in “real-time” as data is collected, and during dedicated  
 800 offline alignment campaigns. The real-time alignment is run in ATLAS’s so-called *calibration loop*,

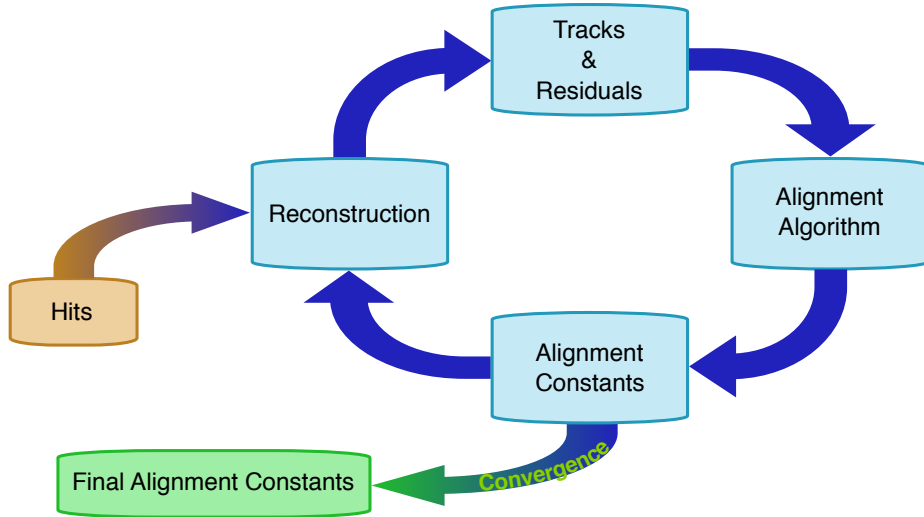


Figure 4.2: Graphical representation of the ID alignment chain.

801 which comprises the first stage in the preparation of data for physics analysis. The calibration loop  
 802 requires the alignment as well as various other detector calibrations to be available within 48 hours  
 803 for initial data processing. A fast, coarse-grained alignment<sup>4</sup> is run on a subset of the available  
 804 data containing full tracking information, and the results are propagated to the reconstruction of  
 805 that particular run [36]. Due to the time constraints of the calibration loop, a full sensor-by-sensor  
 806 alignment is not possible.

807 The more thorough and finely tuned alignments are reserved for the dedicated alignment cam-  
 808 paigns. These generally occur early in data taking campaigns, typically once a sufficient amount  
 809 of data is collected after a detector shutdown, in order to obtain a good baseline alignment for use  
 810 in the remainder of the data collection period. Once data taking is complete, another campaign  
 811 determines an improved set of alignment constants (divided into several “blocks” to account for  
 812 time-dependent misalignments), and the full data is reprocessed using the newly derived detector  
 813 geometry. The initial offline alignment of the ATLAS detector at the beginning of Run 2 in 2015 is  
 814 the subject of Section 4.2.

### 815 4.1.1 Alignment levels

816 The alignment of the detector is performed at several levels of increasing granularity. This adds  
 817 flexibility in being able to align only as finely as needed, and it also allows for global, detector-level

---

<sup>4</sup>The calibration loop runs up to a Level 2 alignment in the silicon detectors, which involves treating each layer of sensors as a single object, defined in greater detail in Table 4.1.

818 misalignments to be corrected first before dealing with finer adjustments.

- 819     ● Level 1 (L1) alignment involves moving entire subdetector components as a single unit, such  
820       as the entire Pixel detector, or the SCT barrel. These often have the largest misalignments,  
821       but they are easily corrected and do not require large volumes of data to do so.
- 822     ● Level 2 (L2) alignment treats individual layers in the silicon detectors (modules in the TRT)  
823       and end cap disks as individual alignable objects.
- 824     ● Level 2.7 (L27) alignment was introduced with the addition of the IBL to the ID in Run 2. It  
825       involves the stave-by-stave alignment of the IBL and Pixel barrel<sup>5</sup>.
- 826     ● Level 3 (L3) alignment treats each sensor in the silicon detectors and each straw in the TRT  
827       as an individual alignable object. It is the finest grained alignment available but also the most  
828       computationally intensive due to the large number of degrees of freedom. The large number  
829       of individual detector sensors being aligned also requires the largest amount of statistics.

830 The different alignment levels are listed in more detail in Table 4.1, including the number of alignable  
831 structures and associated degrees of freedom for each detector component.

832 The implementation of the alignment algorithm in the software is flexible enough to allow each  
833 subsystem to be aligned individually at a specified level. Each alignable structure has six degrees of  
834 freedom: 3 translations ( $T_x, T_y, T_z$ ) and 3 rotations ( $R_x, R_y, R_z$ )<sup>6</sup>; however individual degrees of  
835 freedom may be turned on and off as required. In a typical alignment job, L1 and L2 contain few  
836 enough degrees of freedom that the Global  $\chi^2$  algorithm can be used, but L3 alignments (which can  
837 contain over 36,000 degrees of freedom in the silicon detectors alone) require the Local  $\chi^2$  algorithm.

### 838 4.1.2 Alignment coordinate systems

839 The global coordinate system ( $x, y, z$ ) used by the ID alignment matches that of the ATLAS detector  
840 in general. The positions and orientations of individual detector modules of the ID are defined by  
841 a right-handed local coordinate system ( $x', y', z'$ ) where the origin is defined as the geometrical  
842 center of the module. The  $x'$ -axis for each silicon module is defined to point along the most sensitive  
843 direction of the module, the  $y'$ -axis is oriented along the long side of the module, and the  $z'$ -axis is

---

<sup>5</sup>For the purposes of this Chapter, the term “Pixel” will refer to the original three layers of the Pixel detector, and the IBL will be referenced separately.

<sup>6</sup>The TRT is an exception, as the subdetector does not have any resolution along the length of the straw. Therefore, for the barrel,  $T_z$  is omitted. Similarly for the straws themselves, only two parameters are defined: translation with respect to the radial direction ( $T_\phi$ ) and rotation with respect to the radial axis ( $R_r$  for the barrel and  $R_z$  for the end-caps) [37].

| Level  | Description of alignable structure       | Structures    | DoF     |
|--------|--|---------------|---------|
| 1      | IBL detector                             | 1             | 6       |
|        | Whole Pixel detector                     | 1             | 6       |
|        | SCT barrel and 2 end-caps                | 3             | 18      |
|        | TRT barrel and 2 end-caps ( $T_z$ fixed) | 3             | 17      |
| Total: |  | 8             | 47      |
| 2      | IBL detector                             | 1             | 6       |
|        | Pixel barrel layers                      | 3             | 18      |
|        | Pixel end-cap disks                      | $2 \times 3$  | 36      |
|        | SCT barrel layers                        | 4             | 24      |
|        | SCT end-cap disks                        | $2 \times 9$  | 108     |
|        | TRT barrel 32 modules ( $T_z$ fixed)     | $3 \times 32$ | 480     |
|        | TRT end-cap wheels                       | $2 \times 40$ | 480     |
| Total: |  | 208           | 792     |
| 2.7    | IBL staves                               | 14            | 84      |
|        | Pixel barrel staves                      | $22+38+52$    | 672     |
|        | Pixel end-cap disks                      | $2 \times 3$  | 18      |
|        | Total:                                   |               | 132     |
| 3      | IBL modules                              | 280           | 1,680   |
|        | Pixel modules                            | 1,744         | 10,464  |
|        | SCT modules                              | 4,088         | 24,528  |
|        | TRT barrel wires ( $T_\phi, R_r$ only)   | 105,088       | 210,176 |
|        | TRT end-cap wires ( $T_\phi, R_Z$ only)  | 245,760       | 491,520 |
|        | Total silicon sensors:                   |               | 6,112   |
|        | Total TRT wires:                         |               | 350,848 |
| Total: |  | 36,672        | 701,696 |

Table 4.1: The four alignment levels for each of the detector subsystems. The total number of alignable structures and degrees of freedom (DoF) to be aligned are given for each level.

844 orthogonal to the  $(x', y')$  plane. For the TRT straws, the  $x'$ -axis is perpendicular to both the wire  
 845 and the radial direction, defined from the origin of the global frame to the straw center, the  $y'$ -axis  
 846 points along the straw, and once again the  $z'$ -axis is orthogonal to the  $(x', y')$  plane. A depiction of  
 847 the global and local coordinate systems for the ID is shown in Figure 4.3.

848 When considering the alignment degrees of freedom listed earlier in Section 4.1.1, grouped collec-  
 849 tions of modules, layers, or entire subdetectors use the global coordinate system; individual modules  
 850 use their respective local coordinate systems. The translations  $T_i$  are with respect to the origin of  
 851 the given reference frame, and the rotations  $R_i$  are taken about the Cartesian axes.

## 852 4.2 Early 2015 alignment of the ATLAS detector

853 At the end of Run 1, the LHC was shut down for upgrades and maintenance. During this time,  
 854 a number of upgrades were performed on the ATLAS detector, including the installation of a new

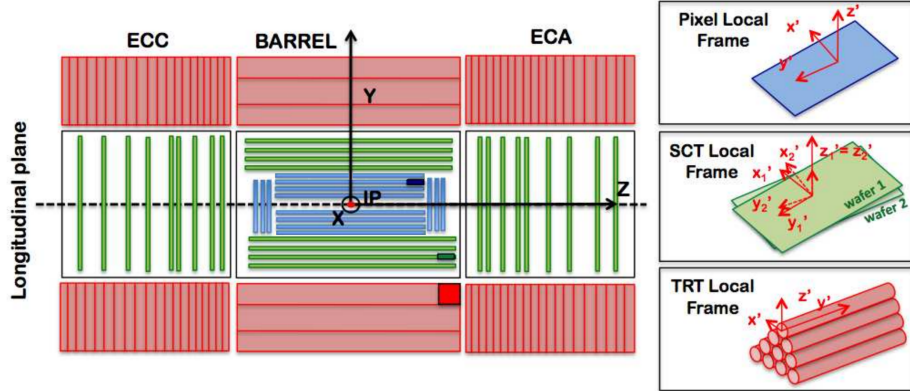


Figure 4.3: A schematic representation of the Inner Detector in the longitudinal plane with the global coordinate system overlaid on top. The Pixel detector and IBL are shown in blue, the SCT in green, and the TRT in red. The local coordinates for each subdetector module are inset on the right. Image taken from [38].

855 innermost layer of the Pixel detector, the Insertable B-Layer (IBL) [39]. TODO: This will certainly  
 856 be defined in the detector description, so maybe the citation and abbreviation are not needed These  
 857 changes to the ID required some detector components to be removed temporarily, and many elements  
 858 shifted relative to each other over the course of the maintenance process. In order to correct for these  
 859 large detector movements prior to  $\sqrt{s} = 13$  TeV collision data taking, an alignment was performed  
 860 using cosmic ray data collected in early 2015 [38]. This alignment was able to correct for the majority  
 861 of the large detector-wide misalignments as well as determine the global position of the IBL at the  
 862 micron level.

863 In June of 2015, shortly after the data taking period began, the first track-based alignment  
 864 of the refurbished ID was performed using  $\mathcal{L} = 7.9 \text{ pb}^{-1}$  of  $\sqrt{s} = 13 \text{ TeV pp}$  collision data [40].  
 865 Starting from the initial geometry determined by the cosmic ray alignment, referred to hereafter  
 866 as the *March alignment*, an improved set of alignment constants, called the *June alignment*, was  
 867 derived from a data set of approximately 1.4 million selected tracks. For comparison, a MC sample  
 868 containing approximately 2.7 million tracks was constructed from dijet events simulated using a  
 869 perfect detector geometry; the MC events are reweighted to match the  $\eta$  and  $p_T$  distributions found  
 870 in the data. Additional validation of the alignment results uses a set of cosmic ray data collected  
 871 by the detector during the LHC collisions.

---

**872 4.2.1 June alignment procedure**

873 The data set used as the input for the alignment contains a subset of physics events used for prompt  
 874 reconstruction recorded at a rate of 10 Hz. To ensure that only high quality tracks are used for the  
 875 alignment, each track is required to have transverse momentum  $p_T > 3$  GeV, contain at least one  
 876 hit in the Pixel detector, at least seven hits in the combined silicon detectors, and at least 25 hits  
 877 in the TRT.

878 A full L3 alignment of the IBL was included in the March alignment; however, a realignment  
 879 was necessary. Since the cosmic rays pass through the detector top-down, the staves on the sides of  
 880 the IBL could not be aligned as precisely as those on the top and bottom due to lower statistics.  
 881 Additionally, the IBL was operating at a temperature of  $-20^\circ\text{C}$  during the cosmic data taking  
 882 and at  $-10^\circ\text{C}$  for collision data taking. This proved to be significant, as it was observed that  
 883 the IBL staves experience a temperature-dependent, parabolic bowing in the local  $x'$ -direction of  
 884 approximately  $-10\mu\text{m/K}$  [41]. As a result, a full L3 alignment of the IBL was essential in order to  
 885 correct for the bowing. Due to it being a brand new element of the detector as well as its importance  
 886 in vertexing and  $b$  jet tagging, aligning the IBL sensors with a high degree of precision was of great  
 887 importance.

888 The June alignment was performed in two stages, with the first pass focusing on relative move-  
 889 ments of the big structures and correcting for the bowing of the IBL. The March alignment corrected  
 890 for these larger movements as well; however, it was observed during Run 1 that these sort of mis-  
 891 alignments are introduced by changing conditions in the detector [35], such as in the cooling system  
 892 or magnet power cycling, which may have occurred between the early cosmic data taking and the  
 893 first  $\sqrt{s} = 13$  TeV collisions. The silicon detectors were aligned at several different levels and the  
 894 IBL was aligned at the module level; the TRT detector was kept fixed to act as a global reference  
 895 frame. The full alignment chain for the first pass consisted of the following steps:

- 896 1. The IBL, Pixel, and SCT detectors were aligned at L1. The SCT barrel was not aligned in  
   897  $T_z$  in order to constrain global displacements along the  $z$ -axis, as the TRT is not sensitive to  
   898 that degree of freedom.
- 899 2. The IBL, and Pixel barrel and end-caps, and SCT barrel were aligned at L2. The SCT end-caps  
   900 were aligned at L1.
- 901 3. The IBL and pixel barrel were aligned at L27, using all six degrees of freedom. The Pixel  
   902 end-cap disks were only aligned in the plane ( $T_x$ ,  $T_y$ , and  $R_z$ ). The SCT was treated the same

903 as in the previous step.

904 4. The IBL was aligned at L3 using all six degrees of freedom for each module.

905 The primary goal for the second pass was to remove a bias in the transverse impact parameter  
 906  $d_0$  present in the March alignment. The resolution of  $d_0$  was also poorer than expected. In order  
 907 to correct for this, an additional constraint was passed to the alignment by adding an impact  
 908 parameter with respect to the beam spot as a pseudo-measurement [42]. When the alignment  
 909 algorithm minimizes the  $\chi^2$ , it will take care of the impact parameter minimization as well. Only  
 910 the IBL and Pixel detectors were aligned in this step. The stages of the second pass are listed below,  
 911 and the beam spot constraint was used in each:

912 1. The IBL and Pixel detectors were aligned at L2 with the SCT fixed.

913 2. The IBL was aligned at L27

914 3. The IBL and Pixel barrel and end-caps were aligned at L3.

915 The set of alignment constants obtained at the end of the second pass represents the June alignment.

916 The highest level of alignment over the course of the two passes for each subdetector is listed in  
 917 Table 4.2.

| Detector |          | Highest level of alignment           |
|----------|----------|--------------------------------------|
| IBL      |          | L3                                   |
| Pixel    | Barrel   | L3                                   |
|          | End-caps | L3 ( $T_x$ , $T_y$ , and $R_z$ only) |
| SCT      | Barrel   | L2 (except $T_z$ )                   |
|          | End-caps | L1                                   |
| TRT      |          | None                                 |

Table 4.2: Summary of the highest level of alignment applied to each ID subsystem when deriving the June alignment.

### 918 4.2.2 Alignment results

919 The primary measure of alignment quality is assessed by looking at the track-hit residual distri-  
 920 butions. If the detector is well aligned, the residuals will be Gaussian-distributed with a mean  
 921 of zero and a width approximating the detector's resolution. The residual distributions are con-  
 922 structed from the same selection of tracks that were used to perform the alignment, and are the  
 923 focus of Section 4.2.2.1. A second check on the alignment involves observables sensitive to the track

parameter resolution. In this case, cosmic rays are used, making use of a “split track” technique that takes advantage of the top-to-bottom cosmic ray trajectory (compared to the center-out trajectory of collision tracks). This method and the corresponding tests of the alignment are detailed in Section 4.2.2.2

Additionally, the effect of the beam spot constrained alignment on the impact parameter  $d_0$  needs to be checked. The  $d_0$  distributions for both the March and June alignments are compared to the MC simulation using a perfect geometry in Figure 4.4. In the March alignment, there is a bias of 18  $\mu\text{m}$  in the mean of the distribution and the width is nearly twice that of the perfect geometry. After the second pass of the June alignment, the mean has shifted to 1  $\mu\text{m}$  and the distribution has narrowed considerably. From this, it appears that the constrained alignment successfully removed the  $d_0$  bias.

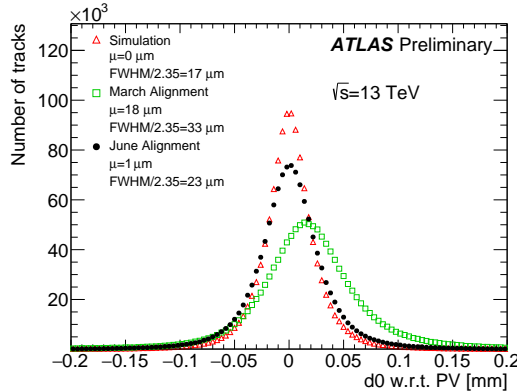


Figure 4.4: The  $d_0$  distributions with respect to the reconstructed primary vertex using the  $\sqrt{s} = 13$  TeV collision data sample reconstructed using the June (black) and March (green) alignments. The data is compared to a MC simulation using a perfect detector geometry (red). The distributions are normalized to the same number of entries.

#### 4.2.2.1 Residual distributions from collisions

As mentioned previously, the primary focus of the June alignment campaign was on the IBL and the Pixel detectors. The detectors are the closest to the beam line and have the finest resolutions of the ID subdetectors. The residual distributions in local  $x$  and  $y$  of the IBL planar sensors<sup>7</sup> are shown in Figure 4.5. These and subsequent figures in this section compare the June and March alignments to the perfectly-aligned MC simulation. Noticeable improvement in the distribution widths can be

<sup>7</sup>The IBL contains 12 planar sensors in the center of a stave, with four 3D sensors on either end. Only the planar sensors are shown here due to low statistics in the 3D sensors as well as poor MC modeling of these sensors.

seen in both the local  $x$ - and  $y$ -directions, nearly matching the simulation in local  $x$ , which is the most sensitive direction.

Due to the temperature-dependent bowing of the IBL, it is also interesting to look at the means of the residual distributions for each ring of IBL sensors along the beam line, as shown in Figure 4.6. A deformation is clearly visible in the March alignment in both measurement directions, and the shape in the local  $x$ -direction is consistent with an average stave bowing due to the different operating temperature of the IBL during the March alignment and the 13 TeV collisions. This feature was nearly eliminated in both directions through the L3 alignment of the IBL sensors.

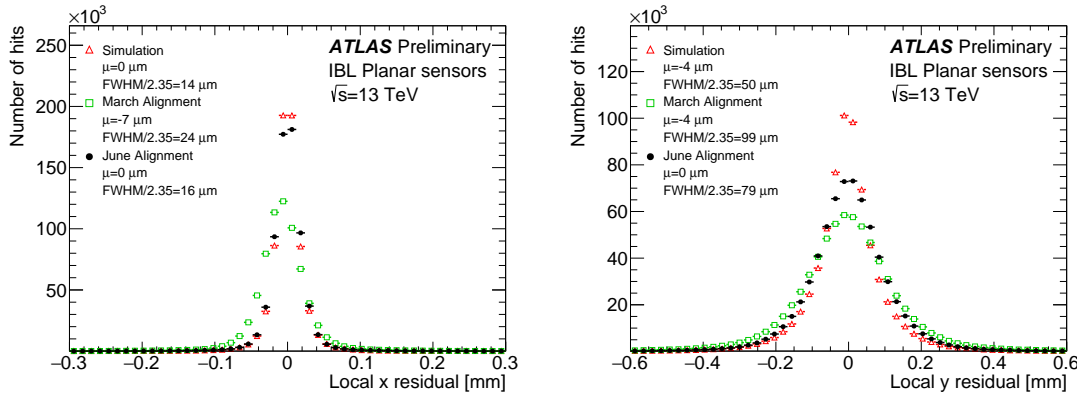


Figure 4.5: Local  $x$  (left) and local  $y$  (right) residual distributions of the IBL planar sensors using the  $\sqrt{s} = 13$  TeV collision data sample reconstructed using the June (black) and March (green) alignments. The data is compared to a MC simulation using a perfect detector geometry (red). The distributions are normalized to the same number of entries.

The local  $x$  and  $y$  residual distributions for the Pixel detector barrel and end-caps are shown in Figure 4.7. Even though the IBL is not included in the plots of the barrel, some of the noticeable improvement in the more sensitive local  $x$  direction is an effect of the improved IBL alignment. Similarly, the relatively broad local  $y$  residual distribution in the barrel likely indicates that further refinement of the IBL alignment was needed along that direction. Even so, the June alignment outperforms the March alignment and rivals the simulation in most of the plots.

Similar distributions for the SCT and TRT barrel and end-caps are shown in Figures 4.8 and 4.9, respectively. Much like with the Pixel residuals, there is a reduction in the width of the TRT residuals between the March and June alignments due to the alignment of the other subdetectors improving the quality of the track fit. Even though neither subdetector was aligned at module-level, the residuals indicate that the previous L3 alignment performed in Run 1 has not degraded

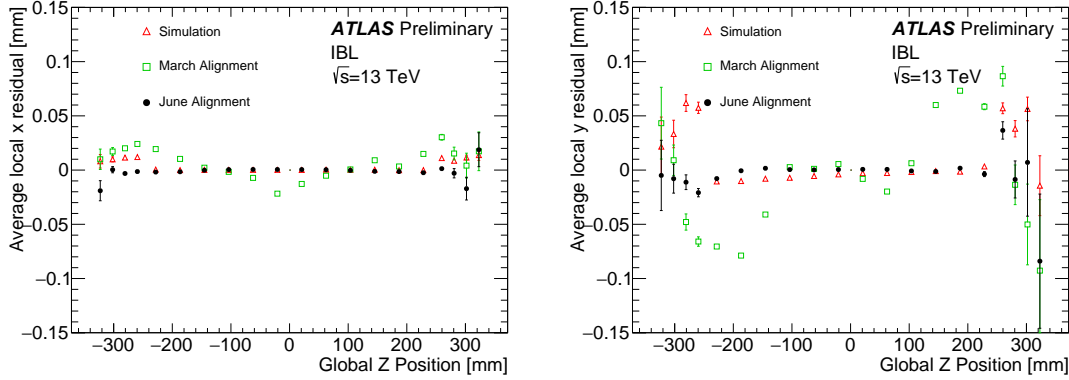


Figure 4.6: The mean of the local  $x$  (left) and local  $y$  (right) residual distributions as a function of the global  $z$  position of each IBL module using the  $\sqrt{s} = 13$  TeV collision data sample reconstructed using the June (black) and March (green) alignments. The data is compared to a MC simulation using a perfect detector geometry (red).

significantly during the upgrade and maintenance period.

#### 4.2.2.2 Track parameter resolution from cosmic rays

Cosmic ray data is very useful as an independent check on the alignment in the barrel of the detector. While tracks from  $pp$  collisions originate within the detector and travel outwards, a cosmic ray that passes through the center of the detector leaves a track in both halves of the detector. If the cosmic ray is split in half, as in Figure 4.10, then it can be treated as two separate tracks each with nearly identical track parameters (some differences arise due to energy loss as the particle passes through the detector). The distribution of the difference in a given track parameter  $\Delta\tau$  is approximately Gaussian with a variance  $\sigma^2(\Delta\tau)$ . Since both tracks come from the same particle, each track individually has a variance equal to  $\sigma^2(\Delta\tau)/2$ . The resolution of the track parameter is then given by the root mean square of the distribution divided by  $\sqrt{2}$ .

Cosmic rays whose split tracks each had transverse momentum  $p_T > 2$  GeV and at least one, eight, and 25 hits in the barrels of the Pixel, SCT, and TRT detectors, respectively, were selected to measure a collection of track parameters. Figure 4.11 shows the difference in the impact parameter  $\Delta d_0$  and the charge divided by the transverse momentum  $\Delta q/p_T$  of the selected split-track cosmic rays for both the March and June alignments. Both distributions show a reduction in width in the June alignment, corresponding to an improvement in the resolution of each track parameter. The  $\Delta d_0$  plot shows a significant improvement in the June alignment, further validating the removal of

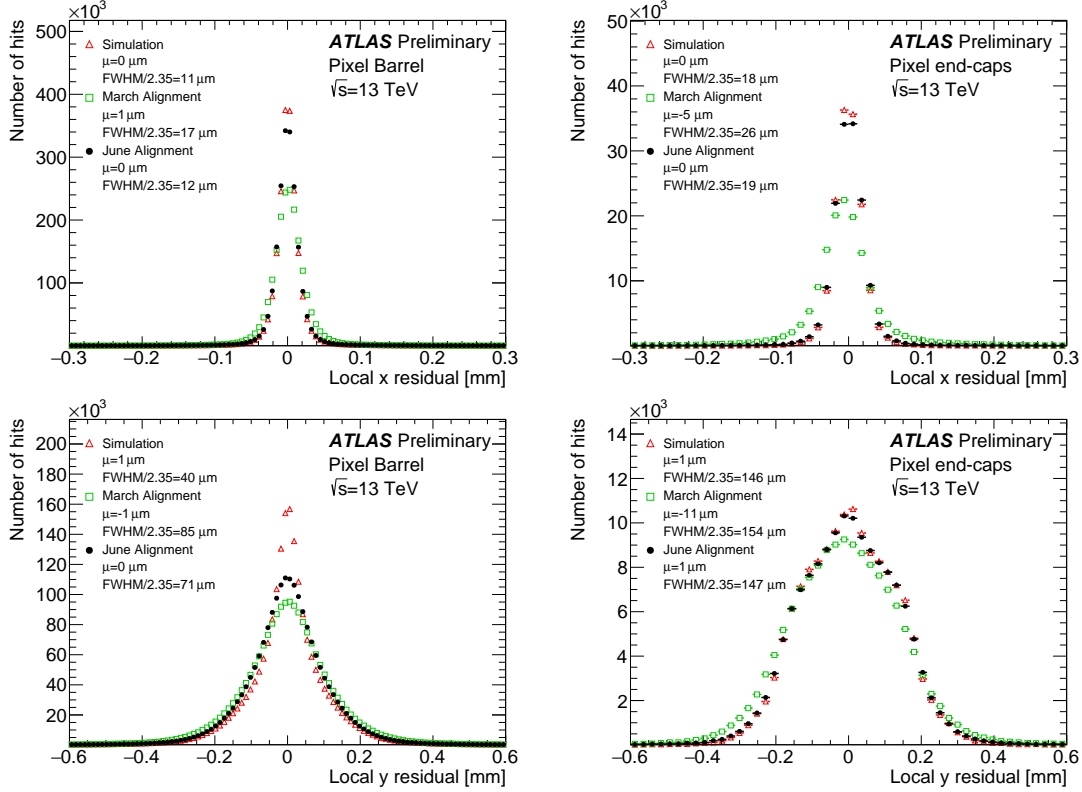


Figure 4.7: Local  $x$  (top) and local  $y$  (bottom) residual distributions for the Pixel barrel (excluding the IBL, left) and end-caps (right) using the  $\sqrt{s} = 13$  TeV collision data sample reconstructed using the June (black) and March (green) alignments. The data is compared to a MC simulation using a perfect detector geometry (red). The distributions are normalized to the same number of entries.

978 the bias in the impact parameter.

### 979 4.2.3 Error scaling

980 The final step in preparing the new set of June alignment constants deals with the adjustment of  
 981 the hit errors, or *error scaling*. Knowledge of the exact position of a hit measurement on a track  
 982 is limited by the accuracy with which the sensors' positions are known. Let  $\sigma$  represent the hit  
 983 uncertainty used in track fitting, and  $\sigma_0$  be the detector's intrinsic uncertainty. If  $\sigma = \sigma_0$ , the pull  
 984 of the track-hit residual distributions should form a Gaussian distribution centered at zero with a  
 985 standard deviation  $\sigma = 1$  [32]. In the case of residual misalignment, the pull distributions' standard  
 986 deviations will stray from unity. The hit uncertainty can be written as:

$$\sigma = a \cdot \sigma_0 \oplus b \quad (4.12)$$

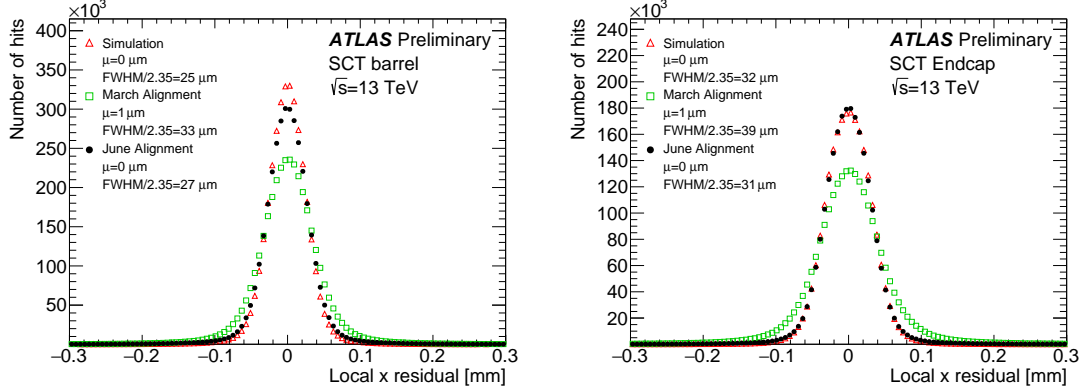


Figure 4.8: Local  $x$  residual distributions for the SCT barrel (left) and end-caps (right) using the  $\sqrt{s} = 13 \text{ TeV}$  collision data sample reconstructed using the June (black) and March (green) alignments. The data is compared to a MC simulation using a perfect detector geometry (red). The distributions are normalized to the same number of entries.

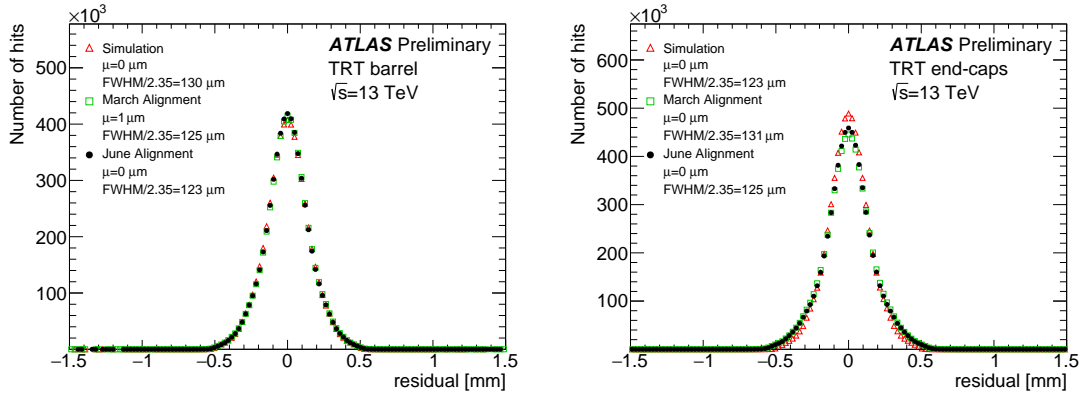


Figure 4.9: Residual distributions for the TRT barrel (left) and end-caps (right) using the  $\sqrt{s} = 13 \text{ TeV}$  collision data sample reconstructed using the June (black) and March (green) alignments. The data is compared to a MC simulation using a perfect detector geometry (red). The distributions are normalized to the same number of entries.

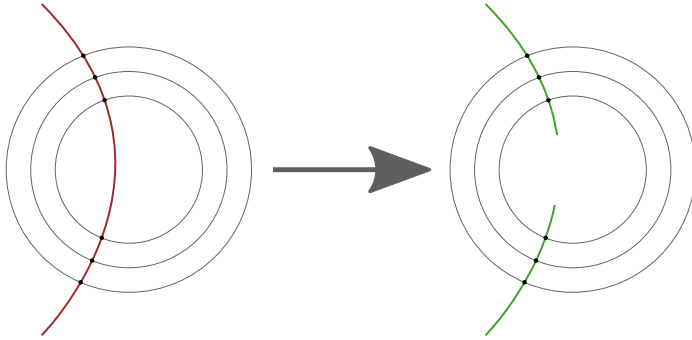


Figure 4.10: Representation of splitting a single cosmic ray track passing through the entire detector (left) into two separate tracks (right).

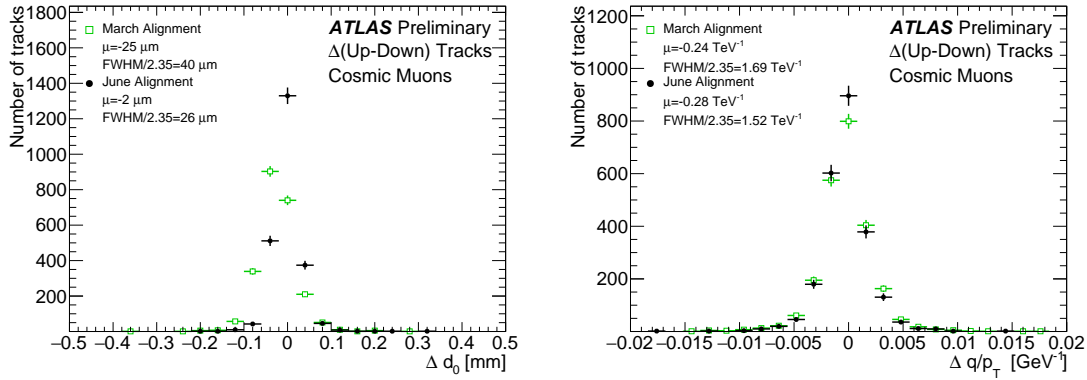


Figure 4.11: Distribution of the difference in the impact parameter  $\Delta d_0$  (left) and charge over transverse momentum  $\Delta q/p_T$  (right) between the two cosmic ray split tracks. The June (black) and March (green) alignments are compared. The distributions are normalized to the same number of entries.

where  $a$  is a scaling factor, and  $b$  is a constant term which can be interpreted as a measure of any remaining misalignment of the detector elements. In this alignment campaign, the value of  $a$  is fixed at  $a = 1$  and  $b$  is evaluated from the residual pull distributions for each subdetector in its sensitive directions.

Once the value of  $b$  is determined, pull distributions derived from the new value of  $\sigma$  should have unit width. The error scaling values for each subdetector are listed in Table 4.3, and the pull distributions for the IBL after error scaling are shown in Figure 4.12.

| Detector | Coordinate | $b(\mu\text{m})$ |
|----------|------------|------------------|
| IBL      | $x$        | 6.4              |
|          | $y$        | 43.6             |
| Pixel    | $x$        | 5.2              |
|          | $y$        | 28.6             |
| Pixel    | $x$        | 7.5              |
|          | $y$        | 0                |
| SCT      | $x$        | 10.8             |
|          | $x$        | 8.6              |
| TRT      | $r\phi$    | 0                |
|          | $r\phi$    | 0                |

Table 4.3: Estimated value of the error scaling term  $b$  for each subdetector component with the June alignment.

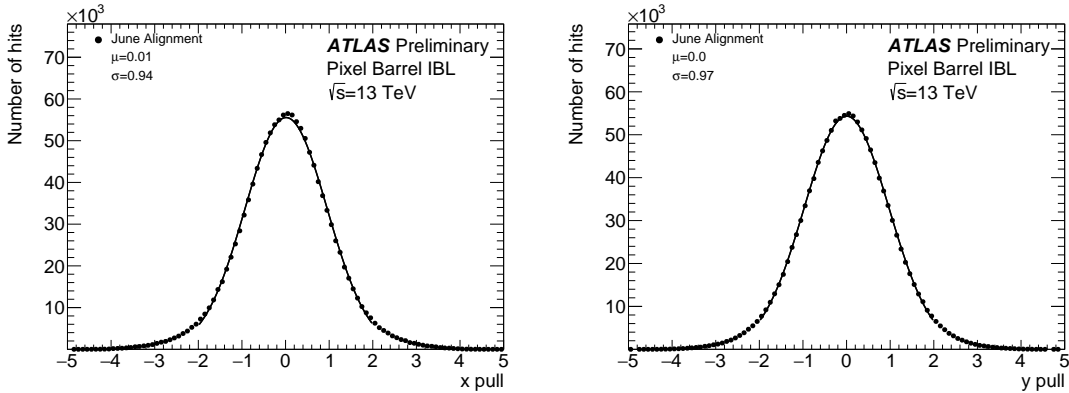


Figure 4.12: Pull distributions in local  $x$  (left) and  $y$  (right) for the IBL using the  $\sqrt{s} = 13$  TeV collision data sample after applying the error scaling.

### 4.3 Level 2 alignment of the TRT

During validation of the final end-of-year reprocessing of the 2015 data, a misalignment was found in the barrel of the TRT detector, as several modules (triangular clusters of straws) showed rotations in the local  $y$  coordinate. The then-best available constants included a full L3 alignment of the silicon detectors and a separate L2 alignment of the TRT. However, not all degrees of freedom were enabled when the TRT was aligned. To correct for these tilts, an additional four iterations of L2 alignment were performed on the TRT enabling all available degrees of freedom ( $T_x$ ,  $T_y$ ,  $R_x$ ,  $R_y$ , and  $R_z$  in the barrel, and  $T_x$ ,  $T_y$ , and  $R_z$  for the endcaps). Plots of the residual means from barrel  $\phi$  sectors containing modules affected by the tilt misalignment are shown in Figure 4.13 before and after the L2 alignment.

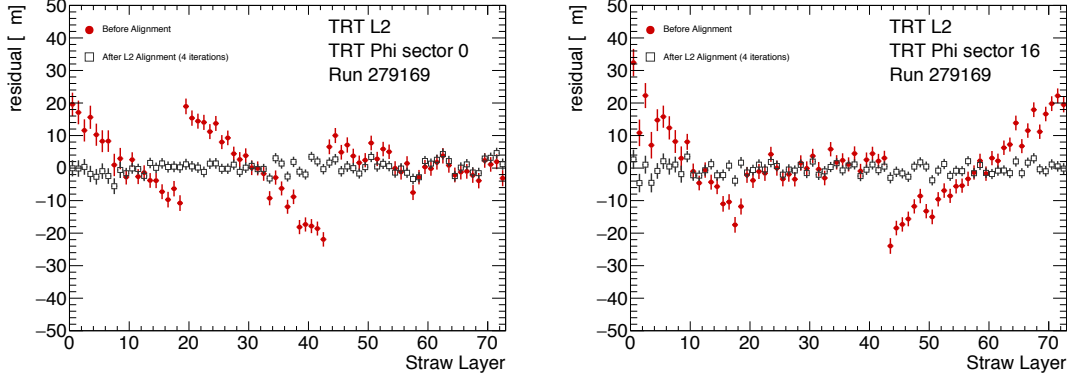


Figure 4.13: Residual means by straw layer in two TRT  $\phi$ -sectors affected by a tilt misalignment. The tilts in each of the three modules are clearly visible in the red points representing the reconstructed data prior to alignment. After four iterations of L2 alignment, the residual means in the gray points are flat.

Following the L2 alignment, some additional time was taken to determine if a full wire-by-wire L3 alignment of the TRT was necessary. The TRT was last aligned at L3 during Run 1, but initial alignment campaigns in Run 2 did not show signs of misalignment, as can be seen from the residual distributions in Figure 4.9. In order to assess the alignment more carefully, two dimensional residual maps in  $\phi$  and  $z$  were constructed for each layer in the TRT barrel and endcaps using the current alignment. These maps were compared to a similar set using the L3 alignment from 2010, from which it was determined that the straw-level alignment indeed hadn't degraded and a new L3 alignment was not needed. The maps for the first layer of the TRT barrel are shown in Figure 4.14 for both sets of alignment constants.

#### 4.4 Momentum bias from sagitta deformations

A variety of weak mode deformations can exist in the detector even after alignment. As mentioned previously, these weak modes consist of misalignments which don't affect the  $\chi^2$  of the residuals and thus are not handled by the basic alignment algorithm. In the presence of a weak mode, the description of the detector geometry can still provide efficient and high quality track fits, but there may also be systematic biases in one or more track parameters. Several weak modes, their impacts on the reconstruction, and the steps taken to eliminate them are detailed in [35, 43]. This section focuses specifically on sagitta distortions that result in a bias in the reconstructed track momentum.

These *sagitta* distortions consist of detector movements orthogonal to the trajectory of the outgo-

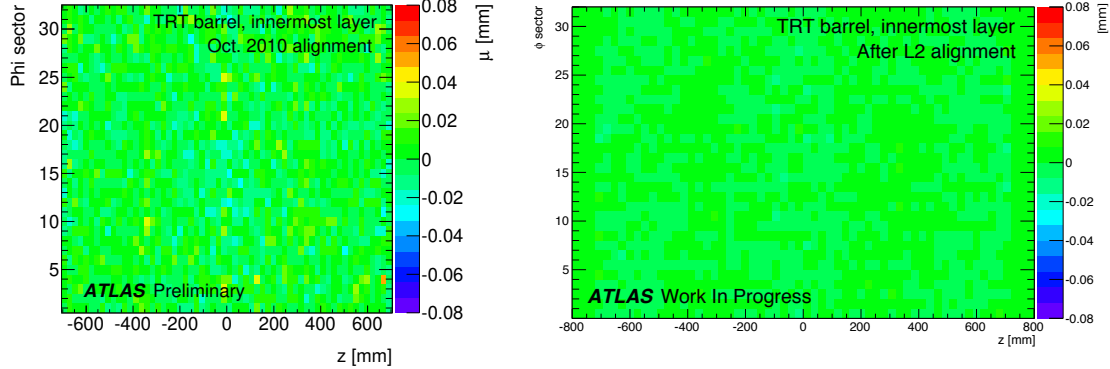


Figure 4.14: Two dimensional map of residuals in the first layer of the TRT barrel vs  $z$  and  $\phi$ . Each bin represents the mean of a Gaussian fit to the TRT residuals in that bin. The map on the left is after the L3 (wire-by-wire) alignment of the TRT performed in 2010, and the map on the right is after the L2 alignment at the end of 2015. The  $z$ -axis for both plots use the same scale. Left figure taken from [32].

1022 ing particle. The effect on the reconstructed track curvature is different for positively and negatively  
1023 charged particles, resulting in a charge-antisymmetric bias. This effect is illustrated in the curl  
1024 deformation shown in Figure 4.15.

1025 In the plane transverse to ATLAS’s magnetic field, outgoing particle tracks form circular arcs.  
1026 The sagitta is defined as the distance from the center of this arc to the center of its base, as shown in  
1027 Figure 4.16, and it represents the “amount of bending” in the track. In the case where the sagitta  $s$   
1028 is considerably smaller than the detector radius  $R_0$ , which is a valid assumption when working with  
1029 high momentum tracks, the transverse momentum of a particle of charge  $q$  can be written as [44]:

$$p_T \propto qB \frac{R_0^2}{8s} \quad (4.13)$$

1030 where  $B$  is the strength of the detector’s magnetic field. If a sagitta bias is present, the track’s  
1031 transverse momentum shifts by [43]:

$$q/p_T \rightarrow q/p_T + \delta_s \quad \text{or} \quad p_T \rightarrow p_T \cdot (1 + qp_T\delta_s)^{-1} \quad (4.14)$$

1032 where  $\delta_s$  is a universal bias parameter that uniquely defines the deformation. Finally, since the  
1033 reconstructed polar angle does not change under a sagitta deformation, the longitudinal component  
1034 of the momentum scales along with the transverse component, and an equivalent equation can be  
1035 written for the total momentum:

$$p \rightarrow p \cdot (1 + qp_T\delta_s)^{-1} \quad (4.15)$$

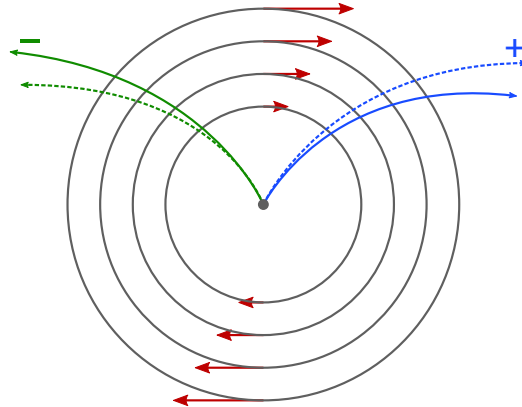


Figure 4.15: Representation of a curl distortion in the detector. The image shows a cutaway in the transverse plane. The deformation is represented by the red arrows, and the impact on the reconstructed positive (blue) and negative (green) tracks are shown. The dashed lines represent the true particle trajectories, and the solid lines represent the reconstructed trajectories.

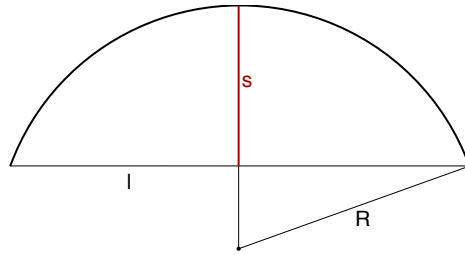


Figure 4.16: Geometric definition of the sagitta  $s$  in relation to the length of the chord  $l$  and the radius  $r$  of a circular arc.

#### 1036 4.4.1 Sagitta bias monitoring with electron $E/p$

1037 Since a sagitta bias results in changes in the momentum of particles' tracks as measured by the ID,  
1038 they can be identified using independent measurements from other systems in the detector. One  
1039 such method involves using the energy-momentum ratio of electrons ( $E/p$ ). Since the electron's  
1040 energy is measured in ATLAS's calorimeter systems, it is not sensitive to any sagitta bias that may  
1041 exist in the ID and the corresponding track momentum. Under the assumption that the calorimeter  
1042 response is independent of the charge of incoming particles, a charge-dependent momentum bias in  
1043 the ID will manifest as a difference in the  $E/p$  ratio for electrons and positrons.

1044 In the presence of a sagitta bias, the momentum will change according to Equation 4.15 and the  
1045 average measured  $\langle E/p \rangle$  can be written as:

$$\langle E/p \rangle^\pm \rightarrow \langle E/p \rangle^\pm \pm \langle E_T \rangle \delta_s \quad (4.16)$$

1046 where the approximation  $p_T \approx E_T$  is used. Assuming that  $\langle E/p \rangle^+ = \langle E/p \rangle^-$  in the absense of a  
 1047 bias, the sagitta bias parameter can be written as:

$$\delta_s = \frac{\langle E/p \rangle^+ - \langle E/p \rangle^-}{2\langle E_T \rangle} \quad (4.17)$$

1048 If the kinematic selections for electrons and positrons are identical, the energy scale of the calorimeter  
 1049 will not factor into the  $\langle E/p \rangle$  difference; however, it will affect  $\langle E_T \rangle$  which would scale the measured  
 1050  $\delta_s$ . This is expected to be a small effect, as the energy scale for electrons has been measured at  
 1051  $\sqrt{s} = 13$  TeV with uncertainties on the per-mil level across the entire detector [45].

#### 1052 4.4.1.1 Measuring $\langle E/p \rangle$

1053 The  $E/p$  ratio is measured using electrons and positrons from  $Z \rightarrow e^\pm e^\mp$  events in order to obtain  
 1054 a high purity sample of electron candidates. They are required to pass a basic selection criteria to  
 1055 ensure they are well measured by both the ID and the calorimeters:

- 1056 •  $E_T > 25$  GeV
- 1057 •  $|\eta| < 2.47$ , excluding the calorimeter’s barrel-to-endcap transition region in  $1.37 < |\eta| < 1.52$
- 1058 • Pass MediumLH identification working point detailed in Section 3.2.4.3
- 1059 • Pass a selection of quality cuts, including a requirement that the electron be identified using  
 1060 cluster information in the calorimeter
- 1061 • The associated track must have at least one hit in the IBL, three in the Pixel detector, and  
 1062 five in the SCT detector.

1063 Events with exactly two opposite-charge electrons passing this selection with a dielectron invariant  
 1064 mass within 30 GeV of the  $Z$  boson mass are then used for the  $E/p$  calculation.

1065 Since the size of the sagitta bias  $\delta_s$  is not expected to be constant across the entire detector,  
 1066 a two-dimensional rectangular grid binned in detector  $\eta$  and  $\phi$  is constructed. From the selected  
 1067 events, separate distributions of  $E/p$  are made for electrons and positrons lying in each bin. Each  
 1068 distribution is fit with Crystal Ball function<sup>8</sup>, and the peak of the distribution is taken as the value  
 1069 of  $\langle E/p \rangle$ . If there is no bias on the track momentum in the bin, the peaks for electrons and positrons  
 1070 should match. Example  $E/p$  distributions including the Crystal Ball fits are shown in Figure 4.17.

---

<sup>8</sup>The Crystal Ball function is a probability density function consisting of a Gaussian core and a power-law tail.

1071 It is important to emphasize that deviations from one in the *ratio* of  $\langle E/p \rangle$  for electrons and  
 1072 positrons indicates that a momentum bias may be present. The value of  $\langle E/p \rangle$  itself is not expected  
 1073 to equal one exactly, as the track momentum on average tends to be slightly lower than the energy  
 1074 measurement in the calorimeter. This is due to the fact that if the electron were to radiate a photon,  
 1075 its momentum would change slightly, while it is likely that both the electron and the emitted photon  
 1076 would leave energy deposits near each other in the calorimeter and be reconstructed into the same  
 1077 object.

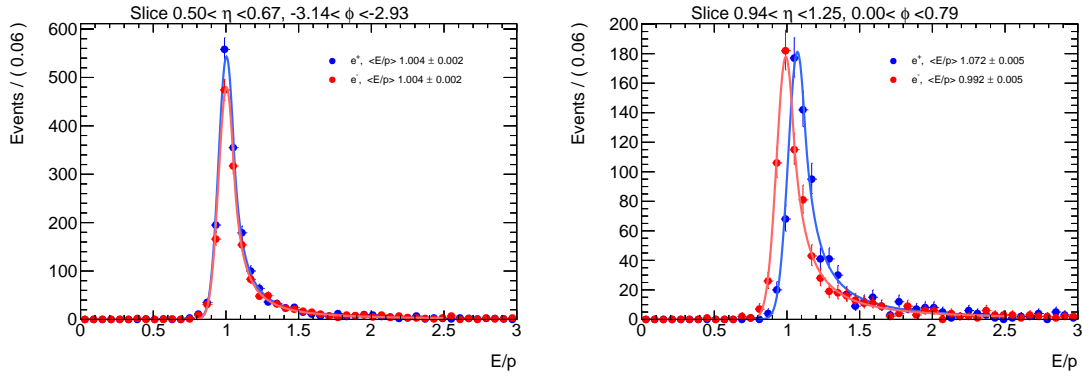


Figure 4.17:  $E/p$  distributions of electrons and positrons in two different  $\eta\text{-}\phi$  bins of the detector. The left hand plot is taken from a region with no momentum bias where  $\langle E/p \rangle^+ = \langle E/p \rangle^-$ , while the right hand plot shows an 8% disagreement in  $\langle E/p \rangle$  between electrons and positrons.

1078 Once the  $\langle E/p \rangle^\pm$  distributions in each  $\eta\text{-}\phi$  bin have been extracted from the fits, a two dimensional map of  $\delta_s$  can be constructed using Equation 4.17. The map gives an overview of sagitta  
 1079 biases that may be present in the detector, and can be used by the alignment algorithm to reduce  
 1080 the bias in the next iteration. In this case, the tracks fed to the alignment have their momenta  
 1081 corrected according to [43]:

$$q/p_{\text{corr}} = q/p_{\text{reco}}(1 - qp_T\delta_s) \quad (4.18)$$

1083 where  $p_{\text{reco}}$  is the reconstructed momentum of the track. The corrected momentum is then con-  
 1084 strained in the alignment.

#### 1085 4.4.1.2 Results in 13 TeV data

1086 The  $E/p$  method has been used to monitor sagitta biases in the detector several times over the  
 1087 course of Run 2. During this time, it has primarily served as an independent cross-check to a  
 1088 second method using  $Z \rightarrow \mu^\pm \mu^\mp$  events [43]. The  $Z \rightarrow \mu^\pm \mu^\mp$  method identifies individual track  
 1089 momentum biases through shifts in the reconstructed  $Z$  mass, which leaves it relatively insensitive

1090 to global sagitta biases. For this reason, the sagitta bias maps produced using this technique are  
 1091 normalized to those from the  $E/p$  method before being used to constrain the alignment.

1092 The results of two implementations of the  $E/p$  method are presented here.

- 1093 1. The first follows the end-of-year reprocessing of the entire ATLAS 2016 data set at  $\sqrt{s} =$   
 1094 13 TeV. Two sets of alignment constants are compared: the *prompt* alignment, which was  
 1095 derived shortly after each run was recorded, and the *reprocessed* alignment. The maps of the  
 1096 sagitta bias comparing the two alignments calculated using the  $E/p$  method are shown in  
 1097 Figure 4.18, and the comparison of the  $\eta$  projection of each map is shown in Figure 4.19.
- 1098 2. The second uses the 2017 data after reprocessing, and compares the effects of multiple it-  
 1099 erations of the method. In each iteration, the momenta of the electrons and positrons are  
 1100 corrected based on Equation 4.15 using the value of  $\delta_s$  computed in the previous iteration,  
 1101 and a new sagitta bias map is calculated. If the method is indeed characterizing the sagitta  
 1102 biases correctly, the corrections should converge quickly. The initial sagitta bias map is com-  
 1103 pared to the map after two such iterations in Figure 4.20, and the sagitta bias projected along  
 1104  $\eta$  for each iteration is shown in Figure 4.21. Indeed, after just two iterations,  $\delta_s$  is consistent  
 1105 with zero in nearly all bins.

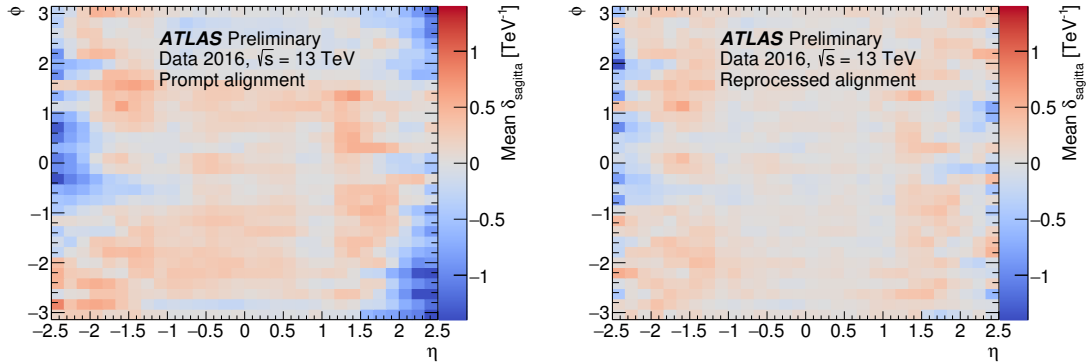


Figure 4.18: Sagitta bias in the  $\sqrt{s} = 13$  TeV data collected by ATLAS in 2016 as a function of  $\eta$  and  $\phi$  for the prompt (left) and reprocessed (right) alignments using the  $E/p$  method.

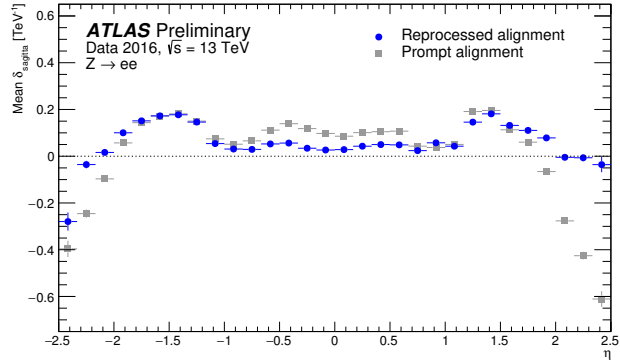


Figure 4.19: Sagitta bias in the  $\sqrt{s} = 13 \text{ TeV}$  data collected by ATLAS in 2016 projected along  $\eta$  for the prompt (gray) and reprocessed (blue) alignments using the  $E/p$  method.

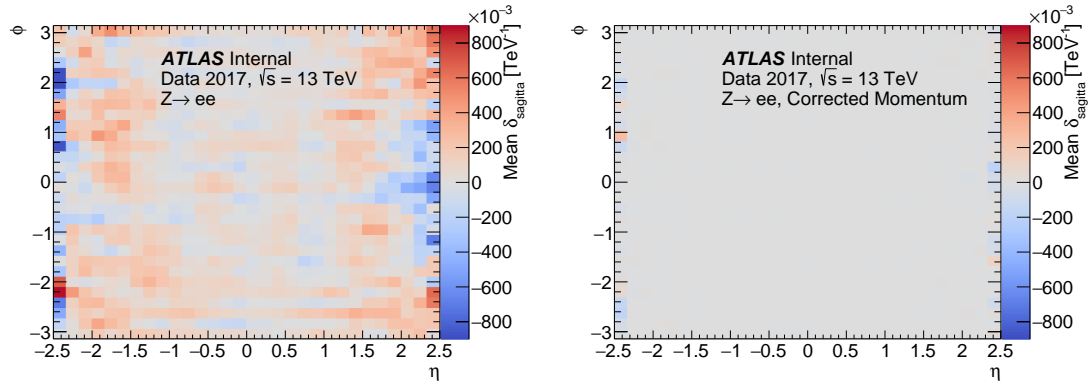


Figure 4.20: Sagitta bias in the  $\sqrt{s} = 13 \text{ TeV}$  data collected by ATLAS in 2017 as a function of  $\eta$  and  $\phi$  in reconstructed electrons (left) and after two iterations of momentum corrections (right) from the  $E/p$  method.

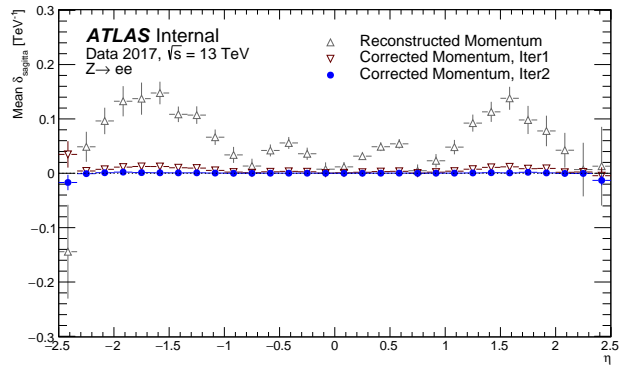


Figure 4.21: Sagitta bias in the  $\sqrt{s} = 13$  TeV data collected by ATLAS in 2017 projected along  $\eta$  in reconstructed electrons (gray) and after one (red) and two (blue) iterations of momentum corrections from the  $E/p$  method.

1106

## CHAPTER 5

1107

1108

# Measurement of same-sign $WW$ production at $\sqrt{s} = 13$ TeV with ATLAS

1109 Production of same-sign  $W$  boson pairs is a particularly interesting SM process. When produced  
1110 via vector boson scattering (VBS),  $W^\pm W^\pm jj$  is particularly sensitive to the electroweak symmetry  
1111 breaking (EWSB) mechanism as well as potential “beyond the Standard Model” (BSM) physics.  
1112  $W^\pm W^\pm jj$  events can be produced via electroweak-mediated (EWK) diagrams, of which VBS is a  
1113 subset, or QCD-mediated diagrams. The biggest advantage of same-sign  $W^\pm W^\pm jj$  lies in its ratio  
1114 of electroweak (EWK) to QCD production cross sections. Despite the opposite-sign  $W^\pm W^\mp$  having  
1115 a considerably larger total cross section, its EWK-mediated diagrams are considerably smaller than  
1116 its QCD-mediated diagrams, while for same-sign  $W^\pm W^\pm$  the ratio is approximately one to one.  
1117 This makes  $W^\pm W^\pm jj$  one of the best channels for studying VBS at the LHC.

1118 The first evidence of electroweak (EWK)  $W^\pm W^\pm jj$  production was seen by the ATLAS and  
1119 CMS experiments at  $\sqrt{s} = 8$  TeV with excesses of  $3.6\sigma$  [46] and  $2.0\sigma$  [47] over backgrounds, respec-  
1120 tively. More recently, ATLAS and CMS have both observed the EWK process at  $\sqrt{s} = 13$  TeV  
1121 with significances of  $6.9\sigma$  [48] and  $5.5\sigma$  [49], respectively. The analysis presented in this chap-  
1122 ter is based off of the ATLAS  $\sqrt{s} = 13$  TeV observation and cross section measurement of EWK  
1123  $W^\pm W^\pm jj$  production [48, 50].

### 1124 5.0.2 Experimental overview of vector boson scattering

1125 VBS processes are very important to understand due to their sensitivity to the EWSB mechanism.  
1126 As explained in Section 2.3, in the absence of a light SM Higgs boson, the scattering amplitude of  
1127 longitudinally polarized vector bosons grows with center-of-mass energy. However, once the Higgs is

introduced, the divergences cancel and the cross section no longer grows unbounded.

With the discovery of the Higgs boson in 2012 [15, 16], the EWSB mechanism can now be directly studied. Due to the exchange of a Higgs in the  $s$ - and  $t$ -channel VBS diagrams ( $W^\pm W^\pm jj$  itself only contains the  $t$ -channel diagram), VBS processes are directly sensitive to properties of the Higgs. For example, the high-mass tail in the  $VV$  scattering system allows an approximation of the effective coupling strength of the Higgs to vector bosons that is independent of any assumptions on the Higgs width [51]. Additionally, the center of mass energy dependence of the  $VV$  scattering can reveal whether the Higgs boson unitarizes the longitudinal scattering amplitude fully or only partially [52].

VBS events are characterized by two quarks from the colliding protons each radiating a massive vector boson which then scatter and decay in the detector. The incoming quarks carry a large amount of momentum and only deflect a small amount upon radiating the vector boson; as a result, they often travel very close to the beam line. Ignoring the decay products of the bosons, these VBS events result in a final state of two vector bosons ( $V$ ) and two jets ( $j$ ) at high pseudorapidities (called *forward jets*) from the outgoing quarks. The shorthand  $VVjj$  is used to represent this final state.

$VVjj$  events can be produced via two different physical processes. The first involves purely electroweak interactions in the tree-level diagrams, with  $\mathcal{O}(\alpha_{\text{EWK}}) = 6$  and will be referred to as *EWK production*. This can be further broken down into VBS and non-VBS production. In the VBS EWK production, the scattering occurs via triple or quartic gauge couplings, as well as the  $s$ - or  $t$ -channel exchange of a Higgs boson. The non-VBS EWK production contains the same final state of two vector bosons and two outgoing quarks, but the bosons do not scatter. Due to gauge invariance, it is not possible to separate the VBS from the non-VBS productions [53]; therefore, both are included in the signal generation and are indistinguishable from one another. The second process involves a mix of the EWK and strong interactions, of order  $\mathcal{O}(\alpha_s) = 2 \otimes \mathcal{O}(\alpha_{\text{EWK}}) = 4$  and will be referred to as *QCD production*. The tree-level Feynman diagrams for VBS EWK, non-VBS EWK, and QCD  $VVjj$  production are found in Figures 5.1, 5.2, and 5.3, respectively.

### 5.0.3 Same-sign $W^\pm W^\pm$ scattering

Same-sign  $W^\pm W^\pm jj$  scattering is considered to be one of the best channels for studying VBS at the LHC due to its favorable ratio of EWK to QCD production [51]. Since the VBS events are the primary source of interest for an analysis, in practice the QCD production would be considered a background to the EWK signal. Therefore a higher EWK-to-QCD ratio results in better sensitivity

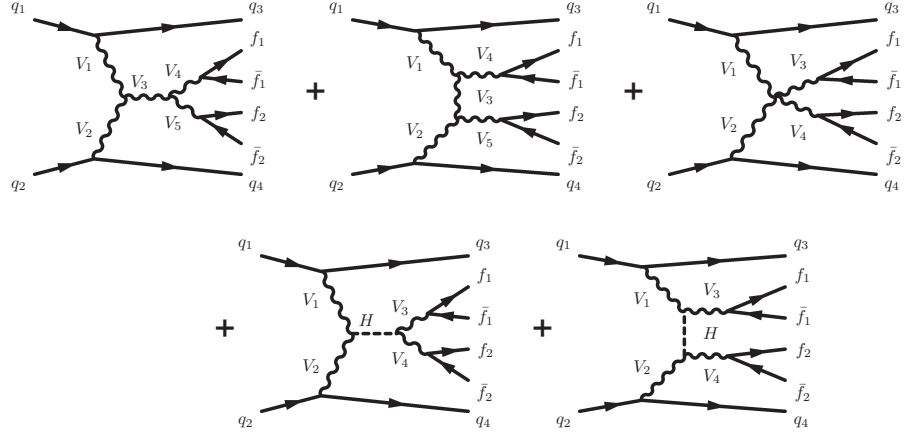


Figure 5.1: Tree-level Feynman diagrams for VBS EWK  $VVjj$  production including triple gauge couplings involving  $W$  and/or  $Z$  bosons (top left and top middle), quartic gauge coupling (top right), or the exchange of a Higgs boson ( $s$ -channel bottom left and  $t$ -channel bottom right). The labels are quarks ( $q$ ), fermions ( $f$ ), and gauge bosons ( $V = W, Z$ ).

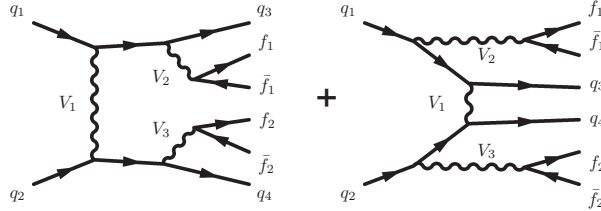


Figure 5.2: Tree-level Feynman diagrams for non-VBS EWK  $VVjj$  production. The labels are quarks ( $q$ ), fermions ( $f$ ), and gauge bosons ( $V = W, Z$ ).

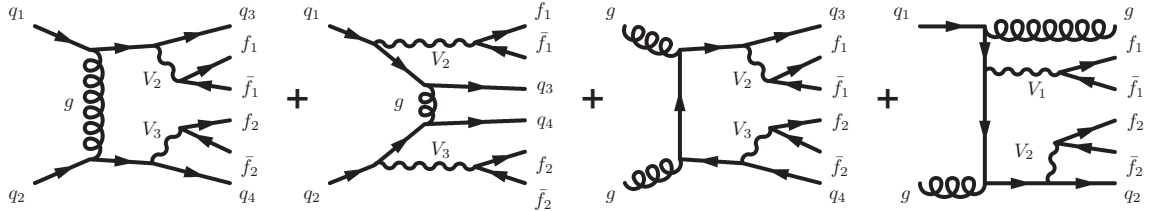


Figure 5.3: Tree-level Feynman diagrams for QCD  $VVjj$  production. The labels are quarks ( $q$ ), fermions ( $f$ ), and gauge bosons ( $V = W, Z$ ).

to VBS. A study at  $\sqrt{s} = 8$  TeV [54] was done using the **SHERPA** Monte Carlo (MC) generator to calculate EWK and QCD production cross sections at leading order for a variety of  $VVjj$  processes decaying to leptons and can be found in Table 5.1. Despite its lower cross section compared to other  $VVjj$  processes, the EWK to QCD ratio for  $W^\pm W^\pm jj$  is approximately one-to-one, whereas for opposite-sign  $W^\pm W^\mp jj$  the ratio is closer to 3%.

| Process       | Final state                   | $\sigma_{\text{EWK}}$ | $\sigma_{\text{QCD}}$ |
|---------------|-------------------------------|-----------------------|-----------------------|
| $W^\pm W^\pm$ | $l^\pm l^\pm \nu\nu jj$       | 19.5 fb               | 18.8 fb               |
| $W^\pm W^\mp$ | $l^\pm l^\mp \nu\nu jj$       | 91.3 fb               | 3030 fb               |
| $W^\pm Z$     | $l^\pm l^\pm l^\mp \nu\nu jj$ | 30.2 fb               | 687 fb                |
| $ZZ$          | $l^+ l^- \nu\nu jj$           | 2.4 fb                | 162 fb                |
| $ZZ$          | $l^+ l^- l^+ l^- jj$          | 1.5 fb                | 106 fb                |

Table 5.1: Predicted cross sections for EQK and QCD production of diboson processes relevant to VBS at  $\sqrt{s} = 8$  TeV using the **SHERPA** MC generator. Loose generator level cuts are applied on lepton  $p_T > 5$  GeV, dilepton invariant mass  $m_{ll} > 4$  GeV, and at least two jets with  $m_{jj} > 10$  GeV. Numbers taken from [54].

This analysis studies  $W^\pm W^\pm jj$  scattering where both  $W$  bosons decay leptonically to  $e\nu$  or  $\mu\nu$ <sup>9</sup>. The  $W^\pm W^\pm jj$  VBS final state consists of two leptons with the same electric charge, two neutrinos, and two high energy forward jets with a large invariant mass. Tree-level Feynman diagrams of VBS  $W^\pm W^\pm jj$  production can be found in Figure 5.4 and a visual representation of the VBS topology can be found in Figure 5.5. The two forward jets also serve as a powerful tool to suppress the QCD production mode. In EWK events, the two jets tend to have much higher separation and a larger combined invariant mass than the two leading jets in a QCD event. The two plots shown in Figure 5.6 highlight the differences in these dijet quantities between the two production modes. An ATLAS event display of a real  $W^\pm W^\pm jj$  candidate event is shown in Figure 5.7.

#### 5.0.4 Overview of backgrounds

In addition to QCD production of  $W^\pm W^\pm jj$  events, there are several other processes that can end up with a final state of two same-sign leptons, two neutrinos, and two jets. However, due to the  $\pm 2$  final state charge, there is a considerable reduction in SM backgrounds (such as  $Z$  boson events) when compared to an analysis like opposite-sign  $W^\pm W^\mp jj$ .

<sup>9</sup>Throughout the rest of this chapter,  $l$  denotes either electrons ( $e$ ) or muons ( $\mu$ ) unless stated otherwise. Additionally,  $e$ ,  $\mu$ , and  $\nu$  (neutrino) with no charge or anti-particle designation refer interchangeably to either the particle or anti-particle.

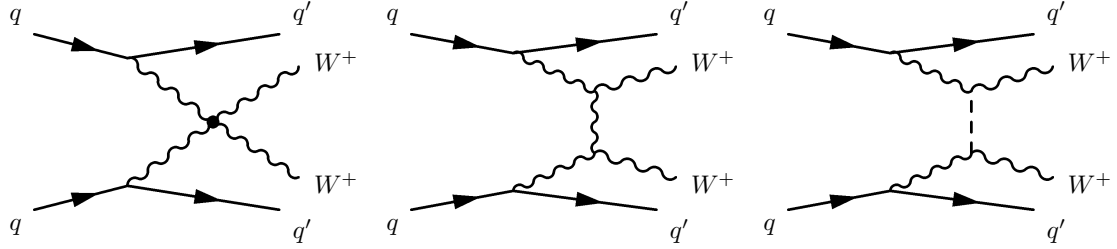


Figure 5.4: Feynman diagrams for VBS EWK production of  $W^\pm W^\pm jj$  events. The leftmost diagram contains a quartic gauge coupling vertex, and the rightmost diagram contains an exchange of a Higgs boson.

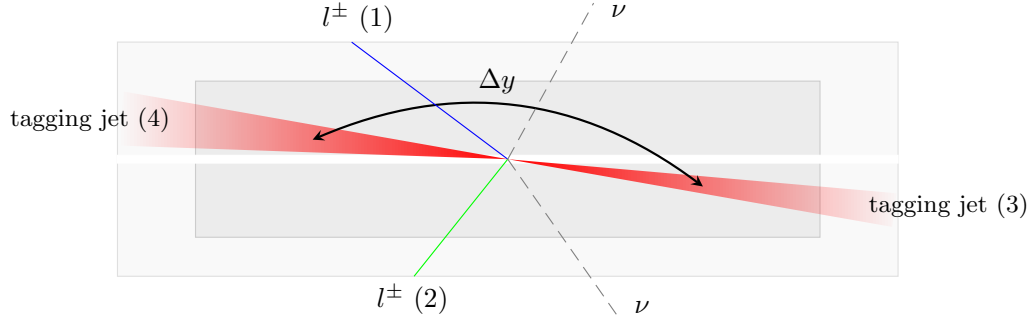


Figure 5.5:  $W^\pm W^\pm jj$  VBS event topology containing two leptons (1 and 2) with the same electric charge, two neutrinos, and two forward tagging jets (3 and 4) with large rapidity separation  $\Delta y$ .

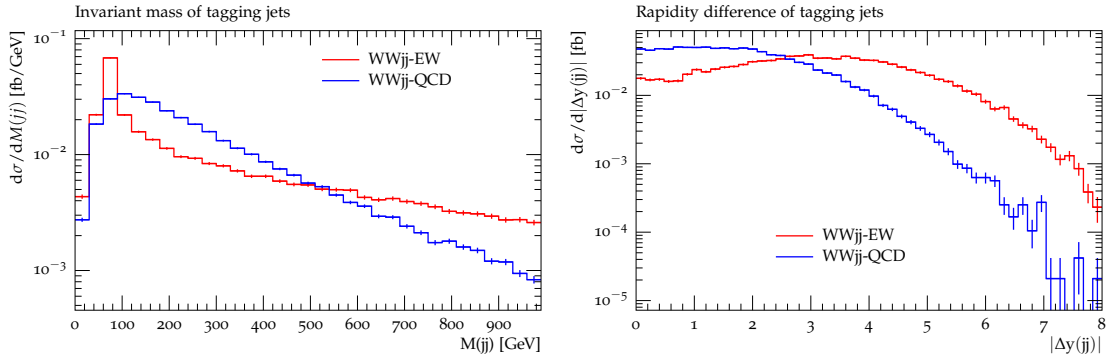


Figure 5.6: Generator level comparisons at  $\sqrt{s} = 8$  TeV of dijet invariant mass ( $m_{jj}$ , left) and dijet rapidity ( $\Delta y_{jj}$ , right) in EWK (red) and QCD (blue)  $W^\pm W^\pm jj$  events. Both data sets have been normalized to the same area. Plots taken from [54].

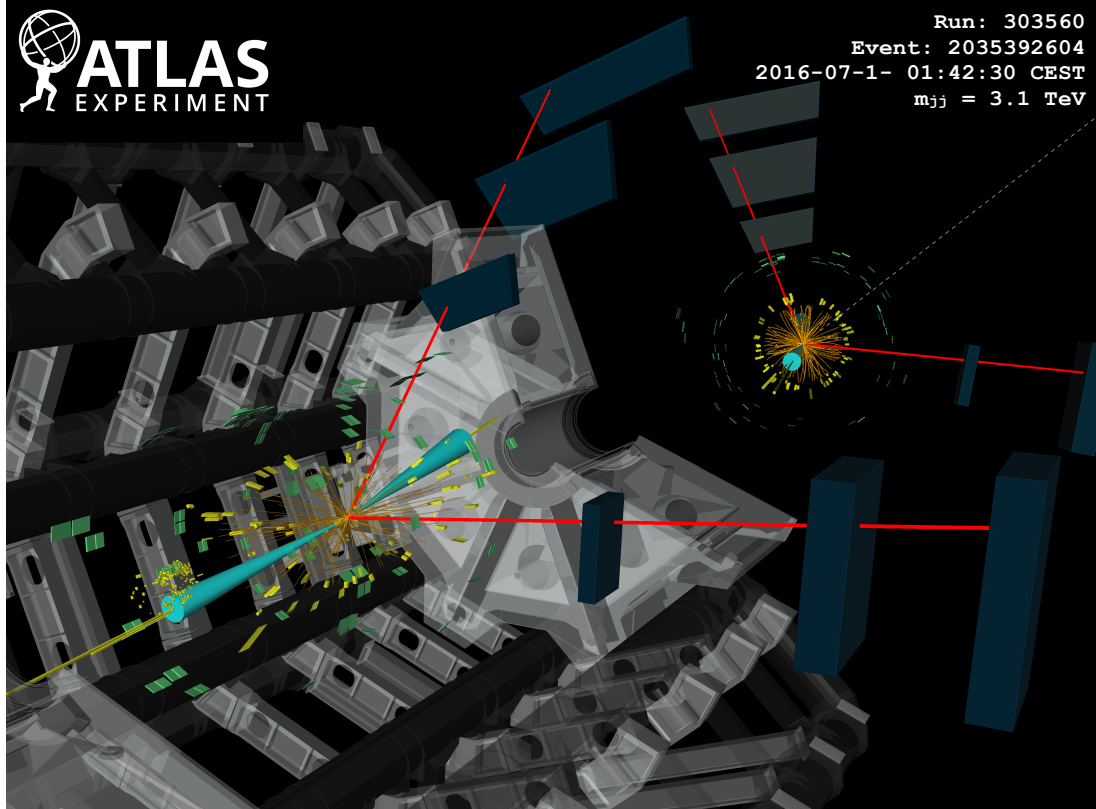


Figure 5.7: ATLAS event display of a  $pp \rightarrow W^+W^+ \rightarrow \mu^+\nu_\mu\mu^+\nu_\mu jj$  event. The muons are represented by the red lines travelling from the ID through the MS, and the forward jets are represented by the blue cones with yellow energy deposits in the calorimeters. The direction of the  $E_T^{\text{miss}}$  in the transverse plane is indicated by the gray dashed line in the inset image. Event display taken from [48].

1178 One of the largest sources of background involves processes with prompt leptons<sup>10</sup>. These are  
 1179 events that contain two leptons with the same electric charge and one or more additional leptons  
 1180 that are “lost”, either by failing the selection criteria or falling outside of the detector’s acceptance.  
 1181 The number of processes that can contribute is limited by the requirement of same-sign leptons, and  
 1182 as a result this background is dominated by processes involving two or more vector bosons, with the  
 1183 largest contribution coming from  $WZ$  events and smaller contributions from  $ZZ$  and  $t\bar{t}V$  events.  
 1184 Triboson events where one boson decays hadronically also contribute to this background; however,  
 1185 the jets are generally softer and more central than in a typical VBS event, and the cuts applied on

<sup>10</sup>Prompt leptons are those that are produced in the primary collision and are a direct decay product of the process of interest. Non-prompt leptons originate from some secondary process, such as a  $b$ -hadron decay, or are jets that get mis-reconstructed as a lepton.

1186 the forward jets suppress these contributions.

1187 The other dominant background comes from non-prompt, or “fake”, leptons. Here one or more  
 1188 leptons originate from the decay of another particle unrelated to the signal process, such as a  
 1189 heavy-flavor decay or photon conversion, or come from a jet that is misidentified as a lepton. This  
 1190 background is mostly made up of events from  $t\bar{t}$  and  $W+\text{jets}$  processes, with a much smaller contri-  
 1191 bution from  $V\gamma$  events. **TODO: check whether  $V\gamma$  really qualifies as non-prompt, we lump  $Z\gamma$  in**  
 1192 **with the charge flip background in the paper...**

1193 Finally, opposite-sign lepton pairs can enter the signal region if one of the leptons is reconstructed  
 1194 with the wrong charge (called *charge misidentification*<sup>11</sup>). In practice, this only affects events with  
 1195 electrons, as the charge misidentification rate for muons is negligible [55]. This is a major background  
 1196 in events with two electrons, but is a much smaller contribution for events with one electron and  
 1197 one muon.

## 1198 5.1 Data and Monte Carlo samples

1199 This analysis uses  $36.1 \text{ fb}^{-1}$  of  $\sqrt{s} = 13$  TeV proton-proton collision data recorded by ATLAS  
 1200 during 2015 and 2016. The uncertainty in the combined integrated luminosity is 2.1%. It is derived  
 1201 following a methodology similar to that detailed in [56] and using the LUCID-2 detector for the  
 1202 baseline luminosity measurements [57] from calibration of the luminosity scale using  $x$ - $y$  beam-  
 1203 separation scans.

### 1204 5.1.1 Monte Carlo samples

1205 A number of Monte Carlo (MC) simulations are employed to model signal and background pro-  
 1206 cesses. In order to model the real collision data as closely as possible, each MC has been run through  
 1207 a full simulation of the ATLAS detector [58] in GEANT4 [59], and events have been reconstructed  
 1208 using the same algorithms as the data. The simulation reproduces as closely as possible the momen-  
 1209 tum resolutions and calorimeter responses of the detector, and also includes the effects of pileup by  
 1210 including soft QCD interactions using PYTHIA v8.1 [60]. The MC samples used in this analysis are  
 1211 detailed in this section and summarized in Table 5.2.

1212 The  $W^\pm W^\pm jj$  samples are modeled using SHERPA v2.2.2 [61, 62, 63] with the NNPDF3.0 PDF  
 1213 set [64]. The EWK signal samples are generated by fixing the electroweak coupling constant to  
 1214  $\mathcal{O}(\alpha_W) = 6$ , and a QCD background sample was also generated with  $\mathcal{O}(\alpha_W) = 4$ . SHERPA includes

---

<sup>11</sup>Charge misidentification is also referred to interchangeably as *charge mis-ID* and *charge flip*.

| Process                | Generator         | Comments  |
|------------------------|-------------------|---|
| $W^\pm W^\pm jj$ (EWK) | SHERPA v2.2.2     | Signal sample   |
| $W^\pm W^\pm jj$ (EWK) | POWHEG-BOX v2     | Systematics sample  |
| $W^\pm W^\pm jj$ (QCD) | SHERPA v2.2.2     |   |
| Diboson                | SHERPA v2.2.2     | Both bosons decay leptonically ( $llll$ , $lll\nu$ , $ll\nu\nu$ ) |
| Triboson               | SHERPA v2.2.1     | One boson decays leptonically, the other hadronically             |
| $W+jets$               | SHERPA v2.2.1     |   |
| $Z+jets$               | Madgraph5_aMC@NLO |   |
| $V\gamma$              | SHERPA v2.1.1     |   |
| $V\gamma jj$ (EWK)     | SHERPA v2.2.4     |   |
| $t\bar{t}V$            | Madgraph5_aMC@NLO |   |
| $t\bar{t}$             | POWHEG-BOX v2     |   |
| Single top             | POWHEG-BOX v1     | EWK $t$ -, $s$ -, & $Wt$ -channels                                |

Table 5.2: Summary of MC samples used in the analysis.

1215 up to one parton at next-to-leading order (NLO) and up to three at leading order (LO) in the  
 1216 strong coupling constant  $\alpha_s$ . A second  $W^\pm W^\pm jj$  EWK sample is generated using POWHEG-BOX  
 1217 v2 [65] with the NNPDF3.0 PDF set and at NLO accuracy. This sample is only used for systematic  
 1218 studies, as POWHEG-BOX does not include resonant triboson contributions in its matrix element, which  
 1219 are non-negligible at NLO [66].

1220 Diboson processes ( $VV$  where  $V = W, Z$ ) are simulated with SHERPA v2.2.2 for mixed hadronic  
 1221 and leptonic decays and SHERPA v2.2.1 for fully leptonic decays of the bosons. Similarly, triboson  
 1222 ( $VVV$ ) and  $V\gamma$  processes are simulated using SHERPA v2.1.1 with up to one parton at NLO and up  
 1223 to three at LO.  $W+jets$  processes are simulated with SHERPA v2.2.1 with up to two partons at NLO  
 1224 and four at LO. All the above SHERPA samples use the NNPDF3.0 PDF set and SHERPA's own parton  
 1225 showering. The  $Z+jets$  events are generated with Madgraph5\_aMC@NLO [67] at LO and interfaced  
 1226 with PYTHIA v8.1 for parton showering.

1227  $t\bar{t}$  events are generated using POWHEG-BOX v2 with the CT10 PDF set [68].  $t\bar{t}V$  samples are  
 1228 generated at NLO with Madgraph5\_aMC@NLO and the NNPDF3.0 PDF set interfaced with PYTHIA v8  
 1229 for parton showering. Finally, single top events are generated with POWHEG-BOX v1 and the CT10f4  
 1230 PDF set interfaced with PYTHIA v6 [69] for parton showering.

## 1231 5.2 Object and event selection

1232 This section details the selection criteria for objects used in the analysis as well as the selection for  
 1233 signal events.

---

1234 **5.2.1 Object selection**

1235 Muons, electrons, and jets all must pass strict selection requirements to ensure that only high quality,  
 1236 well measured objects are used. For leptons, a baseline selection is defined (called the *preselection*),  
 1237 which all leptons must pass in order to be considered for the analysis. This preselection is an  
 1238 intentionally loose set of criteria in order to have high acceptance for rejecting backgrounds with  
 1239 additional leptons (i.e.  $WZ \rightarrow 3l\nu jj$ ). Signal leptons are then required to satisfy a much tighter  
 1240 *signal selection* aimed at suppressing backgrounds from non-prompt or fake leptons. A third set of  
 1241 lepton selection criteria, the *loose selection*, defines a sample enriched in non-prompt leptons, and  
 1242 it is used in the fake factor method for estimating the non-prompt background, discussed in detail  
 1243 in Section 5.3.4. Jets are only required to pass one set of selection criteria. These selections are  
 1244 detailed in the following sections and summarized in Table 5.3 for muons, Table 5.4 for electrons,  
 1245 and Table 5.5 for jets.

1246 **5.2.1.1 Muon candidate selection**

1247 Cuts on muon  $p_T$  serve to reject low momentum leptons from background processes and additional  
 1248 collisions from pileup events. Preselected muons must have  $p_T > 6$  GeV and signal muons  $p_T >$   
 1249 27 GeV. The  $p_T$  requirement for loose muons is lower than for signal muons,  $p_T > 15$  GeV, for  
 1250 reasons that are discussed in Section 5.3.4. Muons are required to fall within the detector's  $\eta$   
 1251 acceptance:  $|\eta| < 2.7$  for preselected muons, which is tightened to  $|\eta| < 2.5$  for the signal muons.

1252 Cuts on the transverse and longitudinal impact parameters are applied to ensure that the can-  
 1253 didate muon originated from the primary particle interaction and not some other source, such as a  
 1254 heavy flavor decay. The preselection and the loose selection both have looser requirements on the  
 1255 transverse impact parameter significance ( $d_0/\sigma_{d_0}$ ) than the signal selection; all three have the same  
 1256 requirement on the transverse impact parameter ( $|z_0 \times \sin \theta|$ ).

1257 Finally, the muon candidates are required to pass a particle identification and an isolation criteria  
 1258 as defined in [70]. The methods used in constructing the identification and isolation workingpoints  
 1259 are described in more detail in Section 3.2.4.2. The muon identification serves to select prompt muons  
 1260 with high efficiency and well measured momenta. This analysis uses two different workingpoints,  
 1261 **Loose** for preselected muons and **Medium** for loose and signal muons, where **Medium** muons are a  
 1262 tighter subset of those that pass the **Loose** requirement. Muon isolation is a measurement of detector  
 1263 activity around the muon candidate, and it is measured with both track-based and calorimeter-  
 1264 based variables. The isolation workingpoint used for the signal muons, **Gradient**, is defined such

that there is 90% or better background rejection efficiency for 25 GeV muons, and 99% efficiency at 60 GeV. There is no minimum isolation requirement for preselected or loose muons. Loose muons are additionally required to fail one or both of the signal transverse impact parameter cut and signal isolation requirement.

| Muon preselection             |                                     |
|-------------------------------|-------------------------------------|
| Momentum cut                  | $p_T > 6$ GeV                       |
| Angular acceptance            | $ \eta  < 2.7$                      |
| Longitudinal impact parameter | $ z_0 \times \sin \theta  < 0.5$ mm |
| Transverse impact parameter   | $d_0/\sigma_{d_0} < 10$             |
| Particle identification       | Loose                               |

| Muon signal selection         |                                     |
|-------------------------------|-------------------------------------|
| Momentum cut                  | $p_T > 27$ GeV                      |
| Angular acceptance            | $ \eta  < 2.5$                      |
| Longitudinal impact parameter | $ z_0 \times \sin \theta  < 0.5$ mm |
| Transverse impact parameter   | $d_0/\sigma_{d_0} < 3$              |
| Particle identification       | Medium                              |
| Particle isolation            | Gradient                            |

| Muon loose selection  |                                     |
|---|-------------------------------------|
| Momentum cut  | $p_T > 15$ GeV                      |
| Angular acceptance  | $ \eta  < 2.5$                      |
| Longitudinal impact parameter                                 | $ z_0 \times \sin \theta  < 0.5$ mm |
| Transverse impact parameter                                   | $d_0/\sigma_{d_0} < 10$             |
| Particle identification                                       | Medium                              |
| Fail signal transverse impact parameter and/or isolation cuts |                                     |

Table 5.3: Muon selection criteria. All muons are required to pass the preselection (top), and then either the signal (middle) or loose (bottom) criteria is applied to the preselected electrons.

### 5.2.1.2 Electron candidate selection

The electron candidate selections are very similar to those for muons. The  $p_T$  cut starts at  $p_T > 6$  GeV for the preselection, increases to  $p_T > 20$  GeV for loose electrons, and finally to  $p_T > 27$  GeV for signal electrons. The  $|\eta|$  cut for electrons requires  $|\eta| < 2.47$  for all electrons, with the region  $1.37 \leq |\eta| \leq 1.52$  removed from loose and signal electrons. This region is where the electromagnetic calorimeter transitions from the barrel to the endcaps and is not fully instrumented. Both the transverse and longitudinal impact parameter cuts are the same for all electron selections.

The electron particle identification uses a multivariate likelihood technique (LH) [71] detailed

in Section 3.2.4.3. Preselected electrons must pass the loosest LH workingpoint `LooseLH` with an additional requirement that there be a reconstructed track hit in the first layer of the pixel detector (a so-called *B*-layer hit). The LH requirement for the loose and signal electrons the tightness of the identification using `MediumLH` and `TightLH`, respectively. As for isolation, the `Gradient` workingpoint is required for signal electrons only. The loose electrons must fail one or both of the signal identification and isolation requirements.

| Electron preselection         |  |
|-------------------------------|--|
| Momentum cut                  | $p_T > 6$ GeV                              |
| Angular acceptance            | $ \eta  < 2.47$                            |
| Longitudinal impact parameter | $ z_0 \times \sin \theta  < 0.5$ mm        |
| Transverse impact parameter   | $d_0/\sigma_{d_0} < 5$                     |
| Particle identification       | <code>LooseLH</code> + <i>B</i> -layer hit |

| Electron signal selection     |  |
|-------------------------------|--|
| Momentum cut                  | $p_T > 27$ GeV   |
| Angular acceptance            | $ \eta  < 2.47$ , excluding $1.37 \leq  \eta  \leq 1.52$ |
| Longitudinal impact parameter | $ z_0 \times \sin \theta  < 0.5$ mm                      |
| Transverse impact parameter   | $d_0/\sigma_{d_0} < 5$                                   |
| Particle identification       | <code>TightLH</code>                                     |
| Particle isolation            | <code>Gradient</code>                                    |

| Electron loose selection                         |  |
|--|--|
| Momentum cut                                     | $p_T > 20$ GeV   |
| Angular acceptance                               | $ \eta  < 2.47$ , excluding $1.37 \leq  \eta  \leq 1.52$ |
| Longitudinal impact parameter                    | $ z_0 \times \sin \theta  < 0.5$ mm                      |
| Transverse impact parameter                      | $d_0/\sigma_{d_0} < 5$                                   |
| Particle identification                          | <code>MediumLH</code>                                    |
| Fail signal identification and/or isolation cuts |  |

Table 5.4: Electron selection criteria. All electrons are required to pass the preselection (top), and then either the signal (middle) or loose (bottom) criteria is applied to the preselected electrons.

### 5.2.1.3 Jet candidate selection

The final objects that need to pass selection are jets. Jets are clustered using the anti- $k_t$  algorithm [72] within a radius of  $\Delta R = 0.4$ . The jets are then calibrated using  $E_T$ - and  $\eta$ -dependent correction factors that are trained using MC simulations [73]. These calibrated jets are then required to have  $p_T > 30$  GeV if they lie in the forward regions of the detector ( $2.4 < |\eta| < 4.5$ ) and  $p_T > 25$  GeV in the central region ( $|\eta| \leq 2.4$ ). In order to suppress pileup jets, the so-called jet-

1289 vertex-tagger (JVT) discriminant associates a jet with the primary interaction vertex [74]; central  
 1290 jets with  $p_T > 60$  GeV are required to pass the Medium JVT workingpoint, which corresponds to  
 1291 an average efficiency of over 92%. Finally, the jets are required to be separated by selected prompt  
 1292 leptons by at least  $\Delta R(j, l) > 0.3$ .

| Jet selection         |  |
|-----------------------|--|
| Momentum cut          | $p_T > 30$ GeV for $2.4 <  \eta  < 4.5$<br>$p_T > 60$ GeV for $ \eta  < 2.4$ |
| JVT cut               | Medium   |
| Jet-lepton separation | $\Delta R(j, l) > 0.3$   |

Table 5.5: Jet selection criteria. All jets are required to pass the above selection in order to be used in the analysis.

#### 1293 5.2.1.4 Treatment of overlapping objects

1294 In the event that one or more objects are reconstructed very close to each other, there is the  
 1295 possibility for double-counting if both originated from the same object. The procedure by which  
 1296 this ambiguity is resolved is called *overlap removal* (OR). The standard ATLAS recommendation  
 1297 for OR is implemented in this analysis [75, 76] and is summarized in Table 5.6.

1298 Since electrons leave a shower in the EM calorimeter, every electron has a jet associated with  
 1299 it. Therefore, any jets close to an electron (within  $\Delta R(e, j) < 0.2$ ) are rejected due to the high  
 1300 probability that they are the same object. On the other hand, when jets and electrons overlap  
 1301 within a large radius of  $0.2 < \Delta R(e, j) < 0.4$ , it is likely that the electron and jet both are part of  
 1302 a heavy-flavor decay, and the electron is rejected.

1303 High energy muons can produce photons via bremsstrahlung radiation or collinear final state  
 1304 radiation which results in a nearby energy deposit in the calorimeters. Non-prompt muons from  
 1305 hadronic decays produce a similar signature; however, in this case the jet has a higher track multiplicity  
 1306 in the ID. It is possible to address both cases by rejecting the jet when the ID track multiplicity  
 1307 is less than three and otherwise rejecting the muon for jets and muons within  $\Delta R(\mu, j) < 0.4$ .

1308 In addition to the case above where muon bremsstrahlung results in a nearby reconstructed jet,  
 1309 the ID track from the muon and the calorimeter energy deposit can lead to it being reconstructed  
 1310 as an electron. In this case, if both a muon and an electron share a track in the ID, the muon is  
 1311 kept and the electron is rejected, unless the muon is calorimeter-tagged<sup>12</sup>, in which case the muon

---

<sup>12</sup>A calorimeter-tagged (CT) muon is a muon that is identified by matching an ID track to a calorimeter energy deposit. CT muons have relatively low reconstruction efficiency compared to those measured by the MS, but can be used to recover acceptance in regions of the detector where the MS does not have full coverage [70].

1312 is removed in favor of the electron.

| Overlap         | Check   | Result (remove → keep) |
|-----------------|---|------------------------|
| Electron & Jet  | $\Delta R(e, j) < 0.2$                                    | Jet → electron         |
|                 | $0.2 < \Delta R(e, j) < 0.4$                              | Electron → jet         |
| Muon & Jet      | $\Delta R(\mu, j) < 0.4$ and Jet $N_{ID}$ tracks $< 3$    | Jet → muon             |
|                 | $\Delta R(\mu, j) < 0.4$ and Jet $N_{ID}$ tracks $\geq 3$ | Muon → jet             |
| Electron & Muon | Shared ID track   | Electron → muon        |
|                 | Shared ID track & muon is calo-tagged                     | Muon → electron        |

Table 5.6: Summary of the overlap removal procedure used in the analysis. If the criteria in the “check” column is met, in the “result” column, the object on the left of the arrow is removed in favor of the object on the right.

### 1313 5.2.2 Signal event selection

1314 After the objects have been selected, cuts are applied on a per-event level to select  $W^\pm W^\pm jj$  signal  
 1315 events. The event selection is summarized in Table 5.8 and is detailed in this section. It includes  
 1316 the results of an optimization performed using a multidimensional grid scan.

1317 The initial event selection begins by choosing events that pass one or more of the trigger re-  
 1318 quirements listed in Table 5.7. At least one signal lepton is “matched” to a passed trigger in order  
 1319 to ensure that it was indeed a signal lepton that fired the trigger. A collection of *event cleaning*  
 1320 cuts must also be passed in order to remove events collected during periods in which one or more  
 1321 components of the detector was not operating optimally. Finally, the events are required to contain  
 1322 at least one interaction vertex. An event can have multiple reconstructed vertices from additional  
 1323 proton-proton collisions that occurred in the same bunch crossing. In this case, the *primary vertex*  
 1324 is determined by choosing the vertex with the largest sum of the  $p_T^2$  of its associated tracks.

|           | 2015 data                          | 2016 data                                       |
|-----------|------------------------------------|---|
| Electrons | $p_T > 24$ GeV and Medium ID       | $p_T > 26$ GeV and Tight ID and Loose isolation |
|           | $p_T > 60$ GeV and Medium ID       | $p_T > 60$ GeV and Medium ID                    |
|           | $p_T > 120$ GeV and Loose ID       | $p_T > 140$ GeV and Loose ID                    |
| Muons     | $p_T > 20$ GeV and Loose isolation | $p_T > 26$ GeV and Medium isolation             |
|           | $p_T > 50$ GeV                     | $p_T > 50$ GeV                                  |

Table 5.7: Summary of trigger requirements for electrons and muons for  $\sqrt{s} = 13$  TeV data collected in 2015 and 2016. At least one of the triggers must be satisfied.

1325 Events are then required to contain exactly two signal leptons with the same electric charge.  
 1326 The dilepton pair must have a combined invariant mass of  $m_{ll} \geq 20$  GeV in order to suppress low

mass Drell-Yan backgrounds. Two additional selections are applied to events in the  $ee$ -channel: both electrons are required to have  $|\eta| < 1.37$  with an invariant mass at least 15 GeV away from the  $Z$ -boson mass to reduce events where one electron is reconstructed with the wrong charge (this background will be discussed in more detail in Section 5.3.3). To suppress backgrounds from events with more than two leptons, events with more than two leptons passing the preselection are vetoed.

Missing transverse energy ( $E_T^{\text{miss}}$ ) represents any particles that escape the detector without being measured, such as neutrinos, and is defined as the magnitude of the vector sum of transverse momenta of all reconstructed objects. It can be difficult to calculate accurately, as it involves measurements from all subsystems within the detector, and it is sensitive to any corrections that may be applied to the reconstructed physics objects [77]. These corrections, including the momentum smearing for muons, energy scale and smearing for electrons, and jet calibrations, are propagated to the  $E_T^{\text{miss}}$  calculation. Events are required to contain  $E_T^{\text{miss}} > 30$  GeV in order to account for the two neutrinos from the  $W$  boson decays.

At least two jets are required. The leading and subleading jets must have  $p_T > 65$  GeV and  $p_T > 35$  GeV, respectively, and are referred to as the *tagging jets*. Events are vetoed if they contain one or more jets that have been tagged as a  $b$ -jet to suppress backgrounds from heavy flavor decays (especially top quark events). The  $b$ -tagging algorithm used by ATLAS is a boosted decision tree (BDT) called MV2c10, and this analysis uses a workingpoint with 85% efficiency [78].

Finally, cuts are applied on the VBS signature outlined in Section 5.0.3. The tagging jets are required to have a dijet invariant mass  $m_{jj} > 200$  GeV and be separated in rapidity by  $|\Delta y_{jj}| > 2.0$ . This preferentially selects the VBS EWK events over the QCD-produced  $W^\pm W^\pm jj$  events.

### 5.3 Background estimations

The major sources of background events are summarized in Section 5.0.4, and the methods used to estimate them are detailed in this section. Prompt backgrounds from  $ZZ$  and  $t\bar{t}V$  are estimated directly from MC simulations. The shape of the  $WZ$  and  $V\gamma$  backgrounds are taken from MC, and the predicted yeilds are normalized to the data predictions in dedicated control regions, as outlined in Sections 5.3.1 and 5.3.2, respectively. Opposite sign events with a charge misidentified electron are estimated by a data-driven background method which is summarized in Section 5.3.3. Finally, a *fake factor* method is used to estimate the contributions from non-prompt backgrounds and is the subject of Section 5.3.4.

| Event selection           |  |
|---------------------------|--|
| Event preselection        | Pass at least one trigger with a matched lepton<br>Pass event cleaning<br>At least one reconstructed vertex  |
| Lepton selection          | Exactly two leptons passing signal selection<br>Both signal leptons with the same electric charge<br>$ \eta  < 1.37$ and $ M_{ee} - M_Z  > 15$ GeV (ee-channel only)<br>Veto events with more than two preselected leptons |
| Missing transverse energy | $E_T^{\text{miss}} \geq 30$ GeV  |
| Jet selection             | At least two jets<br>Leading jet $p_T > 65$ GeV<br>Subleading jet $p_T > 35$ GeV<br>$m_{jj} > 200$ GeV<br>$N_{b\text{-jet}} = 0$<br>$ \Delta y_{jj}  > 2.0$  |

Table 5.8: The signal event selection.

1357 **5.3.1 Estimation of the  $WZ$  background**

1358 The dominant background involving prompt leptons comes from  $WZ + \text{jets}$  events. The contribution  
 1359 is estimated from MC simulation and normalized to data in a control region enriched in  $WZ$  events  
 1360 defined by the same event selection as Table 5.8 for the signal region, with the following changes  
 1361 applied to increase the purity of the  $WZ$  process:

- 1362 • The third lepton veto is inverted, requiring a third lepton with  $p_T > 15$  GeV  
 1363 • Two of the leptons must make a same-flavor opposite-sign pair. If more than one pair exists,  
 1364 the one with  $m_{ll}$  closest to the  $Z$  boson mass is chosen.  
 1365 • The trilepton invariant mass is required to be  $m_{lll} > 106$  GeV to reduce contributions from  
 1366  $Z\gamma$  and  $Z + \text{jets}$

1367 Once the event yields in the control region are calculated, they are propagated to the final signal  
 1368 region fit, detailed in Section 5.4.1, in a single bin combining all the lepton channels. The systematic  
 1369 uncertainties of the  $WZ$  background are also calculated at this time. The event yields for the  $WZ$   
 1370 control region are listed in Table 5.9, and distributions of the leading lepton  $p_T$  and  $\eta$  as well as  
 1371 trilepton invariant mass  $m_{lll}$  are found in Figures 5.9 and 5.8, respectively.

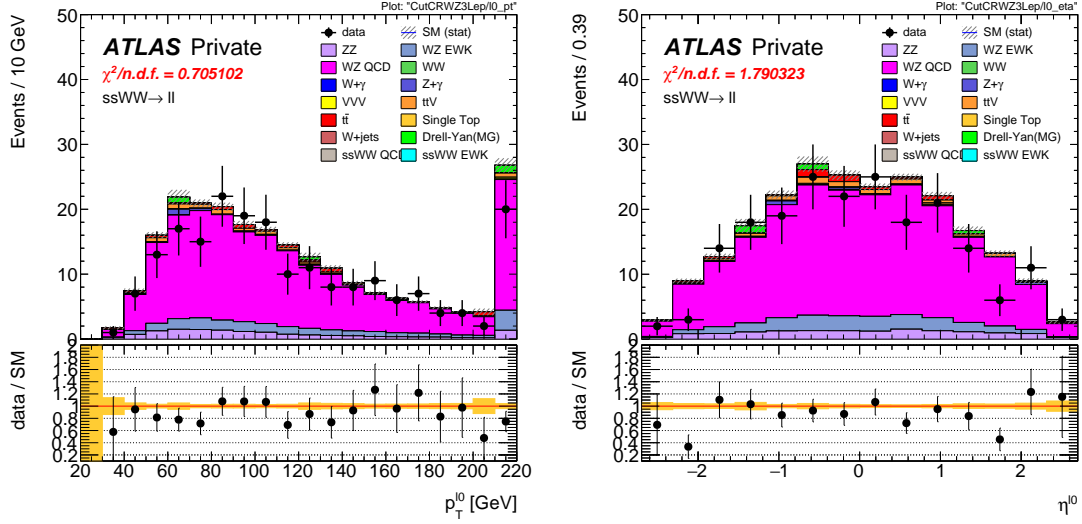


Figure 5.8: Leading lepton  $p_T$  (left) and  $\eta$  (right) distributions in the  $WZ$  control region before normalization. All lepton channels are combined.

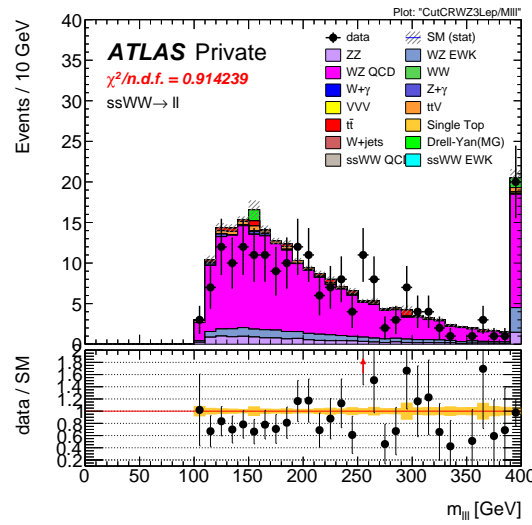


Figure 5.9: Trilepton invariant mass  $m_{lll}$  distribution in the  $WZ$  control region before normalization. All lepton channels are combined.

| Event yields in the $WZ$ control region |                 |
|---|-----------------|
| $WZ$                                    | $197.9 \pm 1.4$ |
| $ZZ$                                    | $14.1 \pm 0.3$  |
| Triboson                                | $1.26 \pm 0.1$  |
| top                                     | $10.8 \pm 1.1$  |
| $Z\gamma$                               | $3.1 \pm 1.1$   |
| $Z+jets$                                | $2.5 \pm 1.4$   |
| Total prediction                        | $229.7 \pm 2.5$ |
| Data                                    | $201 \pm 14.2$  |

Table 5.9: Event yields in the  $WZ$  control region before normalization. All lepton flavor channels are combined.

### 1372 5.3.2 Estimation of the $V\gamma$ background

1373 Events from  $V\gamma$  processes can pass selection if the photon converts into an  $e^+e^-$  pair and one of the  
 1374 electrons passes the selection criteria. The background is estimated from MC simulations which are  
 1375 then scaled by a normalization factor calculated from a control region enriched in  $Z(\mu^+\mu^-)\gamma$  events.  
 1376 This control region selects two opposite-sign muons and an additional electron that is assumed to  
 1377 come from the photon conversion. The full event selection is detailed in Table 5.10.

| $V\gamma$ control region  |
|---|
| Exactly two muons with $p_T > 27$ GeV and $p_T > 20$ GeV          |
| Exactly one additional electron with $p_T > 15$ GeV               |
| Remove overlap between $Z+jets$ and $Z\gamma$                     |
| Di-muon + photon invariant mass $75 < M_{\mu\mu\gamma} < 100$ GeV |
| $E_T^{\text{miss}} < 30$ GeV                                      |

Table 5.10: Selection criteria for the  $V\gamma$  control region.

1378 The  $Z\gamma$  MC samples available do not cover the full range of  $p_T^\gamma$  and  $\Delta R(\gamma, l)$ ; thus, additional  
 1379 Drell-Yan samples ( $Z+jets$ ) are used to fill out the phase space. Overlap between the two samples  
 1380 are removed based to avoid double counting. Events with final state photons at truth level are  
 1381 checked to ensure that the photon did not originate from a hadronic decay. Cuts on  $p_T^\gamma > 10$  GeV  
 1382 and  $\Delta R(\gamma, l) > 0.1$  are then applied at generator level, and  $Z\gamma$  events that fail and  $Z+jets$  events  
 1383 that pass this additional selection are removed.

1384 The normalization factor is calculated directly from the event yields in the  $V\gamma$  control region  
 1385 rather than in the signal fit, as is done for the  $WZ$  background. The event yields are listed in  
 1386 Table 5.11, and the normalization factor is determined to be 1.77. No MC events from  $Z\gamma$  processes  
 1387 survive the full event selection; thus, the scaling is only applied to the  $W\gamma$  background in the signal

region. A systematic uncertainty of 44% is assigned to the background based off of the uncertainties in the calculation of the normalization factor.

| Event yields in the $V\gamma$ control region |                |
|--|----------------|
| $Z\gamma$                                    | $24.6 \pm 3.3$ |
| $Z+jets$                                     | $3.0 \pm 1.5$  |
| diboson + triboson                           | $6.7 \pm 0.3$  |
| top  | $1.5 \pm 0.5$  |
| Total prediction                             | $35.8 \pm 3.7$ |
| Data   | $57 \pm 7.6$   |

Table 5.11: Event yields in the  $V\gamma$  control region. The  $V\gamma$  scale factor of 1.77 is calculated by scaling up the  $Z\gamma$  and  $Z+jets$  backgrounds to account for the difference between the data and predicted total background.

### 5.3.3 Estimation of backgrounds from charge misidentification

If an electron's charge is mis-reconstructed, it can lead to a real, opposite-sign lepton pair passing the same-sign requirement in the event selection. There are two primary reasons this can occur:

1. An electron emits a photon via bremsstrahlung which then converts into an electron-positron pair, and the conversion track with the wrong electric charge is matched to the original electron. This is the dominant process leading to charge flip, and it is highly dependent on the electron  $\eta$  due to the different amount of detector material the electron passes through.
2. The curvature of the electron's track is mismeasured, resulting in the wrong charge being assigned. This process is dependent on the momentum of the electron, as its track becomes more straight as the momentum of the electron increases.

In order to estimate this background, the rate at which an electron's charge is misidentified is calculated from  $Z \rightarrow e^+e^-$  MC simulation. It is known that the MC does not perfectly model the material effects leading to charge flip; as a result, scale factors are applied to the MC in order for it to better reflect the real performance. These scale factors are obtained from the ratio of charge mis-ID rates in data and uncorrected MC in [50] following the method outlined in [79]. Once the scale factors are applied, the charge misidentification rate  $\varepsilon$  can be extracted by comparing the electron's reconstructed charge with the charge of its truth particle:

$$\varepsilon(\eta, p_T) = \frac{N_{\text{wrong charge}}}{N_{\text{prompt electrons}}} \quad (5.1)$$

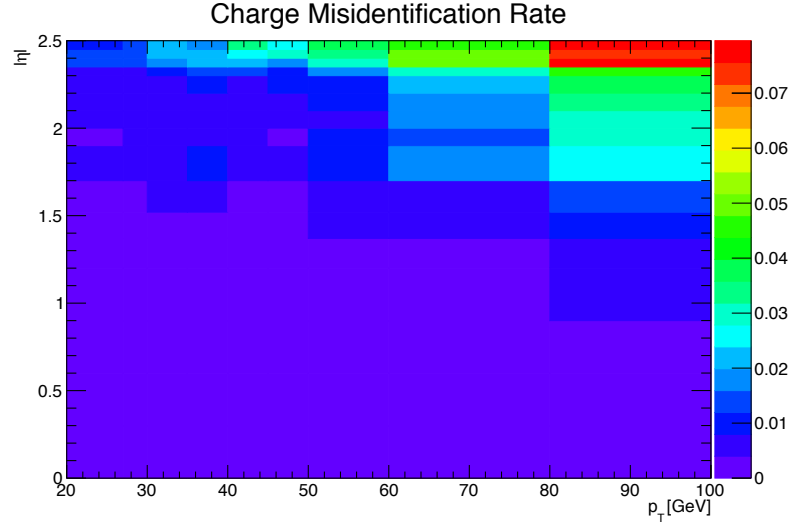


Figure 5.10: Charge misidentification rates for electrons as a function of  $|\eta|$  and  $p_T$ . Rates are calculated from  $Z \rightarrow e^+e^-$  MC after applying scale factors to approximate the charge mis-ID rates in data.

1407 The charge mis-ID rate is calculated in bins of electron  $|\eta|$  and  $p_T$  and varies from below 0.1% in the  
 1408 central region of the detector up to 8% in the forward regions for high  $p_T$  (above 90 GeV) electrons.  
 1409 A two-dimensional plot of  $\varepsilon$  can be found in Figure 5.10.

1410 Given the charge flip rate  $\varepsilon(\eta, p_T)$ , the rate at which an electron has its charge correctly recon-  
 1411 structed is  $(1 - \varepsilon)$ . Thus there are three possible combinations of charge identification, assuming a  
 1412 two-electron event:

- 1413    1. Both electrons are reconstructed correctly:  $(1 - \varepsilon)^2$
- 1414    2. Both electrons are mis-reconstructed:  $\varepsilon^2$
- 1415    3. Only one electron is mis-reconstructed:  $2\varepsilon(1 - \varepsilon)$

1416 In order to estimate the size of the background from charge misidentification, opposite-sign events  
 1417 are selected using the default event selection for a given signal or control region with the same-sign  
 1418 requirement inverted. These events are then weighted by the probability for one of the electrons to  
 1419 be reconstructed with the wrong charge:

$$\omega = \frac{\varepsilon_1(1 - \varepsilon_2) + \varepsilon_2(1 - \varepsilon_1)}{(1 - \varepsilon_1)(1 - \varepsilon_2) + \varepsilon_1\varepsilon_2} \quad (5.2)$$

1420 where the subscripts 1 and 2 refer to the leading and subleading electrons, respectively, and  $\varepsilon_i$  is a  
 1421 function of the  $\eta$  and  $p_T$  of the  $i^{\text{th}}$  electron. In the case of an event with only one electron and one

1422 muon, Equation 5.2 simplifies:

$$\omega = \frac{\varepsilon}{1 - \varepsilon} \quad (5.3)$$

1423 This method assumes that there is little contamination from fake electrons in the opposite-sign  
1424 sample, and this has been verified with MC simulation.

1425 Additionally, charge-flipped electrons tend to be reconstructed with lower energy when compared  
1426 to electrons with the correct charge. This is due to energy loss from the material interactions that  
1427 can cause the charge to be misidentified. A correction factor is calculated from MC simulations,  
1428 comparing the  $p_T$  of the truth electron to its reconstructed counterpart:

$$\alpha = \frac{\left( \frac{p_T^{\text{reco}}}{p_T^{\text{truth}}} - 1 \right)_{\text{correct charge}}}{\left( \frac{p_T^{\text{reco}}}{p_T^{\text{truth}}} - 1 \right)_{\text{wrong charge}}} \quad (5.4)$$

1429 The correction is then applied to the  $p_T$  of the charge-flipped electron via

$$p_T = p_T^0 / (1 + \alpha) + dE \quad (5.5)$$

1430 where  $p_T^0$  is the uncorrected  $p_T$  of the electron and  $dE$  is a gaussian smearing factor centered at  
1431 zero with a width related to the energy resolution. Since which electron is misreconstructed is never  
1432 determined in this method, in the case of a two-electron event, the energy correction is applied  
1433 randomly to one of the two electrons based on the probabilities for them to be charge-flipped. This  
1434 also determines the overall sign of the event; the charge of the electron that does not receive the  
1435 correction is taken to be the charge for both.

1436 Systematic uncertainties on the charge mis-ID rates are calculated by generating two additional  
1437 sets of rates with the uncertainties on the scale factors varied up and down. The size of the esti-  
1438 mated charge flip background without the energy correction applied is also taken as a systematic  
1439 uncertainty. These systematic uncertainties are estimated to be approximately  $\pm 15\%$ .

#### 1440 5.3.3.1 Validation of the charge misidentification estimate

1441 The performance of the charge misidentification estimation is tested in the same-sign inclusive  
1442 validation region (VR), defined in Table 5.12. For  $ee$  events, the mass of the dilepton pair is required  
1443 to lie within 15 GeV of the  $Z$  boson mass to increase the purity of the charge flip background.  
1444  $t\bar{t}$  production, which can contribute to both the charge mis-ID and fake lepton backgrounds, is  
1445 suppressed by the  $b$ -jet veto. The di-electron invariant mass is shown in Figure 5.11, and distributions  
1446 of the leading and subleading electron  $p_T$  in the  $ee$ -channel are shown in Figure 5.12 with the  $Z$

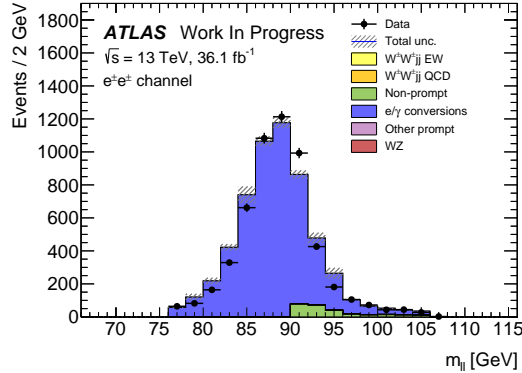


Figure 5.11: Dilepton invariant mass distribution  $m_{ll}$  for the  $ee$  channel in the same-sign inclusive VR.

mass cut inverted. Agreement between data and prediction is seen within the total statistical and systematic uncertainties in the VR.

| Same-sign inclusive VR                                   |  |
|--|--|
| Exactly 2 same-sign signal leptons                       |  |
| $p_T > 27$ GeV for both leptons                          |  |
| $m_{ll} > 20$ GeV  |  |
| $ m_{ee} - m_Z  > 15$ GeV ( $e^\pm e^\pm$ -channel only) |  |
| $N_{b\text{-jet}} = 0$                                   |  |

Table 5.12: Selection criteria for the same-sign inclusive validation region.

#### 5.3.4 Estimation of non-prompt backgrounds with the fake factor method

Events with one prompt lepton produced in association with hadronic jets can pass the event selection if a jet is misidentified as a charged lepton or if a non-prompt lepton from the decay of a heavy flavor particle (such as  $b$ - and  $c$ -hadrons) passes the signal lepton criteria. These misidentified jets and non-prompt leptons are collectively referred to as *fake leptons*, or simply *fakes*. The rate at which a fake lepton is misidentified is generally not modelled well enough by the MC to accurately estimate their contributions directly from simulation. Therefore, a data-driven technique called the *fake factor* is used to estimate the size and shape of background processes from fake leptons. In this analysis, a new modification to the fake factor is used involving the particle isolation variables; the method is outlined in the context of the *default* fake factor in Section 5.3.4.1, and the modified fake factor is outlined in Section 5.3.4.2.

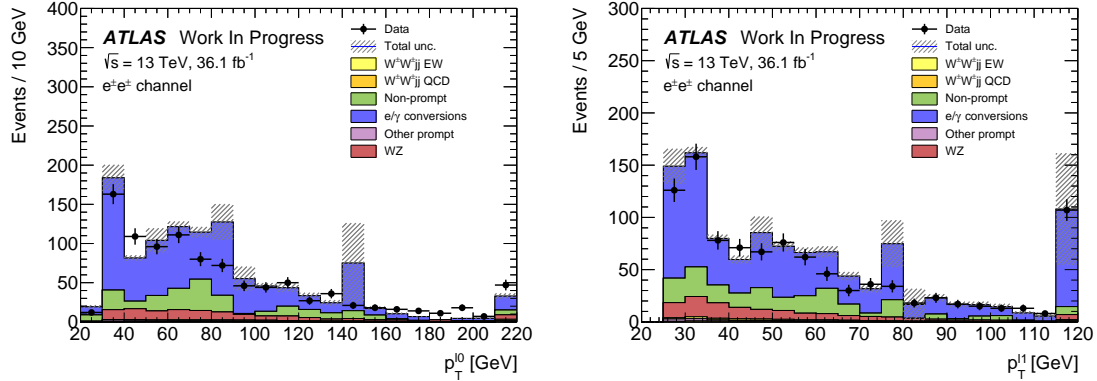


Figure 5.12:  $p_T$  distributions for the leading (left) and subleading (right) electron for the  $ee$  channel in the same-sign inclusive VR. In these plots, the cut requiring  $m_{ee}$  to fall within the  $Z$  mass window has been inverted in order to test the modelling away from the  $Z$  peak.

#### 1460 5.3.4.1 Overview of the default fake factor method

1461 The goal of the fake factor method is to measure the fake rate from real collision events in a region  
 1462 enriched in fake leptons and use it to estimate the size of the fake lepton background in a chosen  
 1463 signal or control region. This is done by creating two samples using different lepton definitions:

- 1464 1. The *nominal* sample is made up of leptons passing the signal selection.
- 1465 2. The *loose* sample is made up of leptons that fail the signal selection while still passing a  
 1466 loosened set of criteria. This sample is enriched in fake leptons and is orthogonal to the set of  
 1467 signal leptons.

1468 Using the sets of nominal and loose leptons, a fake factor  $f$  can be calculated in a region enriched  
 1469 in processes that are prone to producing fake leptons:

$$f = \frac{N_{\text{nominal}}}{N_{\text{loose}}} \quad (5.6)$$

1470 Since the fake rate is not expected to be constant over the entire phase space, the fake factor can  
 1471 be divided into bins:

$$f(b) = \frac{N_{\text{nominal}}(b)}{N_{\text{loose}}(b)} \quad (5.7)$$

1472 where  $b$  represents the bin number. In this analysis, the fake factor is binned in lepton  $p_T$ .

1473 In order to estimate the fake background contribution in a given signal or control region, the  
 1474 fake factor is applied to a second control region with a selection identical to the region of interest  
 1475 with one of the leptons required to satisfy the loose criteria. The region for which the background

1476 is estimated contains two nominal leptons and is referred to as *nominal+nominal* ( $NN$ ), and the  
 1477 associated control region where the fake factor is applied contains one nominal and one loose lepton  
 1478 and is referred to as *nominal+loose* ( $NL$ ). The fake background in a  $NN$  region can then be  
 1479 calculated as:

$$N_{NN}^{\text{fake bkg.}} = \sum_b f(b) N_{NL}(b) \quad (5.8)$$

1480 Backgrounds containing two prompt leptons can also enter the  $NL$  region if one of the leptons  
 1481 passes the nominal selection and the other passes the loose selection. Since the fake factor method  
 1482 estimates the fake background by scaling the amount of non-prompt events in the  $NL$  region, if these  
 1483 prompt contributions are not be removed, they will be included in the scaling and the background  
 1484 will be overpredicted. The final estimate of the fake background becomes:

$$N_{NN}^{\text{fake bkg.}} = \sum_b f(b) (N_{NL}(b) - N_{NL}^{\text{prompt}}(b)) \quad (5.9)$$

1485 **5.3.4.2 The fake factor with  $p_T^{\text{cone}}$**

1486 When a jet produces a non-prompt lepton, that lepton only carries a fraction of the underlying jet's  
 1487 total momentum. Due to the isolation cut applied to the nominal leptons, they typically carry a  
 1488 much larger percentage of the underlying jet momentum<sup>13</sup> than the loose leptons (which are allowed  
 1489 to fail this criteria).

1490 This discrepancy in the underlying jet momentum fraction can cause problems in the calculation  
 1491 of the fake factor  $f$ . Consider the case where two separate events have jets of identical momentum,  
 1492 but one produces a non-prompt lepton that passes the nominal selection, and the other produces a  
 1493 non-prompt lepton that passes the loose selection. The loose lepton on average will have lower  $p_T$   
 1494 than the nominal lepton despite both originating from jets with the same momentum. This can be  
 1495 seen explicitly when comparing the  $p_T$  of a muon to its associated truth jet:

$$\Delta p_T(\mu, j) = \frac{p_T(j) - p_T(\mu)}{p_T(j) + p_T(\mu)} \quad (5.10)$$

1496 Since muons are not included in the jet reconstruction algorithm,  $\Delta p_T$  approximates the momentum  
 1497 of the muon compared to the rest of the jet. For muons that carry more than 50% of the jet's  
 1498 momentum,  $\Delta p_T$  will be negative and vice-versa. The  $\Delta p_T$  distributions for nominal and loose  
 1499 muons in  $t\bar{t}$  MC events is shown Figure 5.13, where a 50 GeV jet on average corresponds to a  
 1500 35 GeV nominal muon and a 20 GeV loose muon<sup>14</sup>.

<sup>13</sup>Since the isolation variables are a measure of detector activity around the lepton, if other nearby particles carried a significant portion of the jet's momentum, the lepton would likely fail this cut.

<sup>14</sup>To better illustrate the point, here the muon is added back into the jet  $p_T$ , and the corresponding muon  $p_T$  is

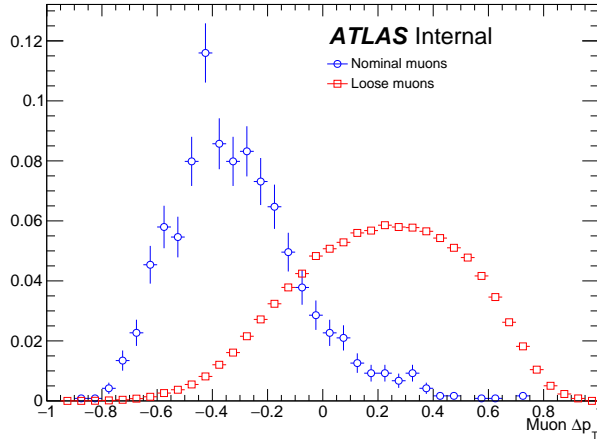


Figure 5.13:  $\Delta p_T$  distributions for nominal (blue) and loose (red) muons in simulated  $t\bar{t}$  events. Each muon has been matched to a truth-level jet. Both distributions are normalized to unit area.

1501 Since the default fake factor defined in Equation 5.7 is binned in lepton  $p_T$ , within a given bin,  
 1502 the underlying jet  $p_T$  spectrum can differ substantially between the numerator and the denominator.  
 1503 Additionally, these differences can vary depending on the process producing the non-prompt leptons  
 1504 or on the specific kinematic selections of the signal or control regions where the fake factor is applied.

1505 Fortunately, the majority of the jet momentum not carried by the non-prompt lepton (excluding  
 1506 neutrinos) can be recovered using isolation variables. A track-based isolation is chosen, referred to  
 1507 as  $p_T^{\text{cone}}$ , and it contains the sum of the  $p_T$  of all particle tracks originating from the primary vertex  
 1508 within a cone of  $\Delta R < 0.3$  around the lepton. Thus, the sample of loose leptons in the denominator  
 1509 of the fake factor calculation is binned in  $p_T + p_T^{\text{cone}}$  rather than simply lepton  $p_T$ . Adding the  
 1510 isolation cone greatly reduces the difference in the fraction of the underlying jet momentum carried  
 1511 by the nominal and loose leptons. To check this, a new  $\Delta p_T$  is calculated between a lepton and its  
 1512 matched truth jet, where the truth jet  $p_T$  has been corrected to include all muons within a cone of  
 1513  $\Delta R < 0.4$ :

$$p_T(j) = p_T(j_{\text{truth}}) + \sum_{\Delta R < 0.4} p_T(\mu_{\text{truth}}) \quad (5.11)$$

1514 The  $\Delta p_T$  distributions comparing  $p_T$  and  $p_T + p_T^{\text{cone}}$  for nominal and loose leptons using the corrected  
 1515 jet  $p_T$  are found in Figure 5.14, and better agreement is seen between the numerator (nominal) and  
 1516 denominator (loose with  $p_T + p_T^{\text{cone}}$ ) distributions.

---

obtained via  $\Delta p_T(\mu, j) = \frac{(p_T(j) - p_T\mu) - p_T(\mu)}{(p_T(j) - p_T\mu) + p_T(\mu)} = \frac{p_T(j) - 2p_T(\mu)}{p_T(j)}$ .

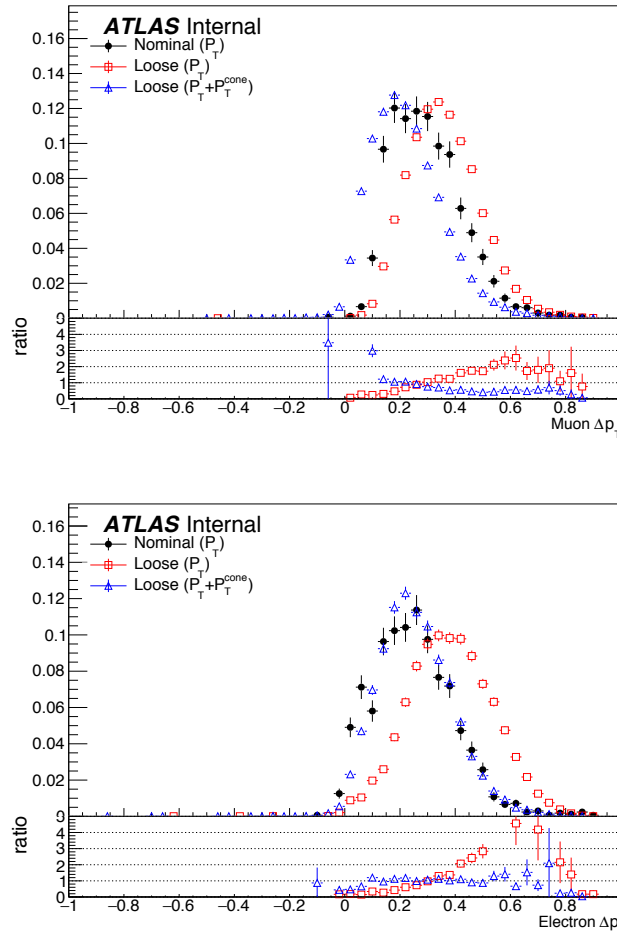


Figure 5.14:  $\Delta p_T$  distributions for muons (top) and electrons (bottom) in simulated  $t\bar{t}$  events. Each lepton has been matched to a truth-level jet, and that truth jet has had its  $p_T$  corrected to include all truth muons within a cone of  $\Delta R < 0.4$ . The nominal leptons are in black.  $\Delta p_T$  is calculated for the loose leptons using  $p_T$  (red) and  $p_T + p_T^{\text{cone}}$  (blue).

1517 The numerator remains binned in lepton  $p_T$ , due to the fact that it is meant to mirror the signal  
 1518 region as closely as possible, and the signal lepton selection does not use  $p_T + p_T^{\text{cone}}$ . The impact of  
 1519 this is expected to be negligible due to the  $p_T^{\text{cone}}$  isolation being small for signal leptons, as shown  
 1520 for muons in Figure 5.15. Finally, the fake factor  $f$  becomes:

$$f(b) = \frac{N_{\text{nominal}}(b(p_T))}{N_{\text{loose}}(b(p_T + p_T^{\text{cone}}))} \quad (5.12)$$

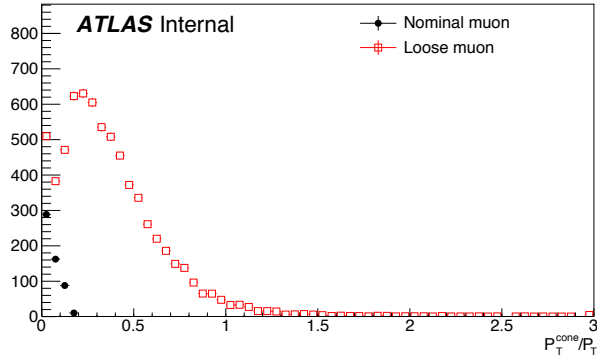


Figure 5.15: Distributions of  $p_T^{\text{cone}}/p_T$  for nominal (black) and loose (red) muons in simulated  $t\bar{t}$  events.

#### 1521 5.3.4.3 Application of the fake factor

1522 The fake factor itself is measured from a sample of events passing a dijet selection requiring  
 1523 exactly one lepton (either passing the nominal or loose selections) and at least one jet. The leading  
 1524 jet must also be  $b$ -tagged and approximately back-to-back with the lepton in order to enhance non-  
 1525 prompt lepton contributions while reducing contributions from processes involving  $W$  and  $Z$  bosons.  
 1526  $W$  boson events are further suppressed by requiring the sum of the  $E_T^{\text{miss}}$  and the transverse mass  
 1527 of the lepton and  $E_T^{\text{miss}}$  to be less than 50 GeV. The full event selection for the dijet region is  
 1528 summarized in Table 5.13.

1529 The numerator sample is constructed from dijet events in which the lepton passes the nominal  
 1530 (signal) selection and is binned in the lepton  $p_T$ . Similarly, the denominator sample is made up of  
 1531 the remaining dijet events where the lepton passes the loose selection and is binned in the lepton  
 1532  $p_T + p_T^{\text{cone}}$ . The nominal and loose leptons pass the signal selection<sup>15</sup> and loose selection, respectively,

<sup>15</sup>The  $p_T > 27$  GeV cut in the signal lepton selection is dropped in favor of the  $p_T > 15$  GeV requirement in the dijet selection.

| Dijet event selection                                    |
|--|
| Event preselection                                       |
| Exactly one lepton with $p_T > 15$ GeV                   |
| $N_{\text{jet}} > 0$                                     |
| Leading jet is $b$ -tagged                               |
| $p_T^{\text{lead. jet}} > 25$ GeV                        |
| $p_T^{\text{lead. jet}} > 30$ GeV if $ \eta_j  > 2.5$    |
| $ \Delta\phi(l, \text{lead. jet})  > 2.8$                |
| $m_T(l, E_T^{\text{miss}}) + E_T^{\text{miss}} < 50$ GeV |

Table 5.13: Event selection for the dijet region used for calculating the fake factor. The selected lepton can pass either the nominal (signal) or loose selections. In the case of the nominal leptons, the  $p_T > 27$  GeV requirement is replaced with  $p_T > 15$  GeV.

1533 defined earlier in Table 5.3 for muons and Table 5.4 for electrons. Backgrounds from  $W+\text{jets}$ ,  $Z+\text{jets}$ ,  
 1534  $t\bar{t}$ , and single top processes are estimated from MC simulations requiring one lepton to be prompt  
 1535 using the truth information; these contributions are subtracted from the dijet data. The fake factor  
 1536 is then calculated using Equation 5.12 for muons and for central and forward electrons separately.  
 1537 The muon fake factor is shown in Figure 5.16, and the two electron fake factors are shown in  
 1538 Figure 5.17. The numerical values of the fake factors, including their systematic uncertainties which  
 1539 will be discussed in Section 5.3.4.4, are listed in Table 5.14.

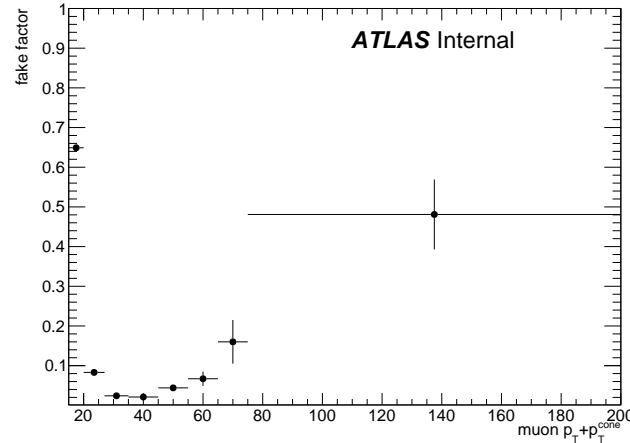


Figure 5.16: The measured fake factor as a function of muon  $p_T + p_T^{\text{cone}}$ . The error bars represent the statistical uncertainty only.

1540 In order to properly account for the denominator being binned in  $p_T + p_T^{\text{cone}}$ , special care needs  
 1541 to be taken when estimating the fake background from the  $NL$  regions. For the purposes of the

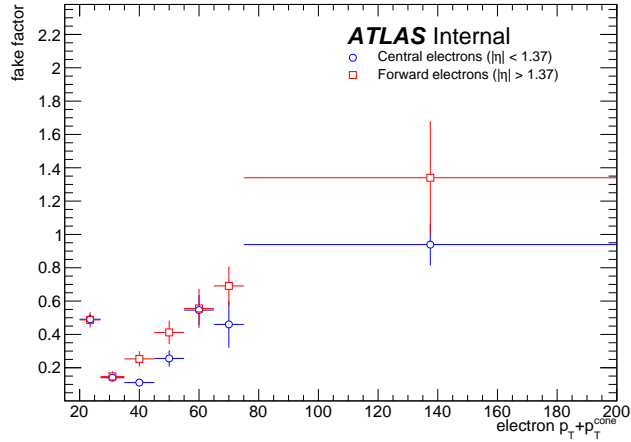


Figure 5.17: The measured fake factor as a function of electron  $p_T + p_T^{\text{cone}}$  in the central ( $|\eta| < 1.37$ , blue) and forward ( $|\eta| > 1.37$ , red) regions of the detector. The error bars represent the statistical uncertainty only.

1542 fake factor calculation, it is perhaps more intuitive to consider a loose *object* with  $p_T = p_T + p_T^{\text{cone}}$   
 1543 instead of simply a loose *lepton*, as the lepton and the underlying jet are treated as a whole with this  
 1544 method. When the lepton  $p_T$  cuts required by a particular signal or control region are applied to  
 1545 nominal and loose leptons, the cut is applied to the  $p_T$  of the nominal lepton and to the  $p_T + p_T^{\text{cone}}$   
 1546 of the loose object. Similarly, when looking up the fake factor weight for a given *NL* event, the  
 1547 value taken from the bin corresponding to the  $p_T + p_T^{\text{cone}}$  of the loose object. Finally, when applying  
 1548 the weight to the event,  $p_T + p_T^{\text{cone}}$  is assigned as the  $p_T$  of the loose object. Figure 5.18 contains a  
 1549 graphical representation of this procedure.

1550 Finally, it should be noted that the addition of  $p_T^{\text{cone}}$  to the loose object may cause the loose  
 1551 leptons in the denominator sample to migrate into higher bins. This results in an overall decrease in  
 1552 the number of loose objects in the lower  $p_T + p_T^{\text{cone}}$  bins due to there not being additional leptons at  
 1553 lower  $p_T$  to replace them. Since the fake factor is a ratio of the number of events in a bin, this effect  
 1554 causes the first few bins of the fake factor to increase, as can be seen clearly in Figure 5.16. However,  
 1555 the signal and control regions (and their corresponding *NL* regions) contain a  $p_T > 27$  GeV cut that  
 1556 prevents these migrations from negatively impacting the fake estimation.

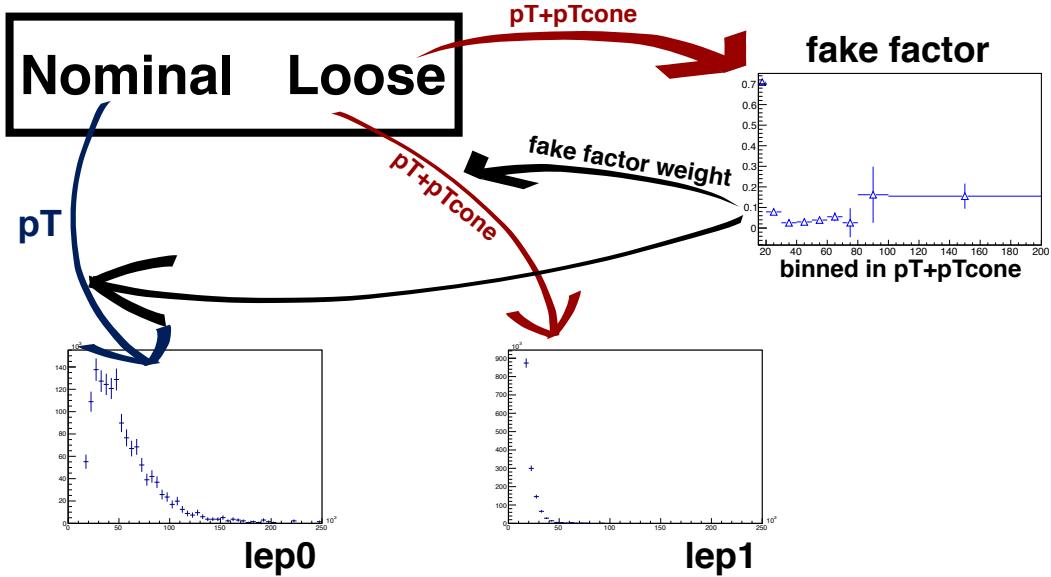


Figure 5.18: Graphical representation of the fake factor application using  $p_T + p_{T\text{cone}}$ . The value of  $p_T + p_{T\text{cone}}$  for the loose lepton is used to “look up” the fake factor weight which is then applied to the event. The loose lepton’s  $p_T$  becomes  $p_T + p_{T\text{cone}}$  for the purpose of the fake background estimation.

#### 1557 5.3.4.4 Systematic uncertainties

1558 Four sources of systematic uncertainty are considered: the dijet event selection, the prompt back-  
 1559 ground subtraction, the jet flavor composition, and residual dependence on the underlying jet  $p_T$   
 1560 spectrum. In order to measure the impact of these systematics, new fake factors are computed  
 1561 with each of the systematic variations and the differences from the nominal values are taken as the  
 1562 uncertainty.

- 1563 1. In order to estimate uncertainties due to the dijet selection, the cut on  $M_T + E_T^{\text{miss}}$  is varied  
 1564 by  $\pm 5$  GeV,  $\Delta\phi(l, j)$  by  $\pm 0.1$ , and the jet  $p_T$  cut by  $+5$  GeV.
- 1565 2. To estimate the systematic uncertainty on the prompt background subtraction, the MC pre-  
 1566 diction in a  $W$ +jets control region is compared to data. The discrepancy between data and  
 1567 MC is found to be approximately 10% [50]. Therefore, the prompt background used for the  
 1568 subtraction is scaled up and down by  $\pm 10\%$ .
- 1569 3. The difference in the jet flavor composition between the dijet events and the events in the  
 1570  $NL$  regions can affect the accuracy of the fake background estimation. The dijet sample is

1571 dominated by light jets, while the  $NL$  regions tend to be dominated by heavy flavor from  $t\bar{t}$ .  
 1572 To account for this, the fake factor is computed with a  $b$ -jet veto.

1573 4. To measure any residual dependence on the underlying jet  $p_T$  spectrum, the leading jet  $p_T$   
 1574 distribution is reweighted to match the  $p_T$  spectrum of truth jets that produce fake leptons  
 1575 in MC simulations. This results in an increase in the number of nominal and loose leptons at  
 1576 high momentum [50].

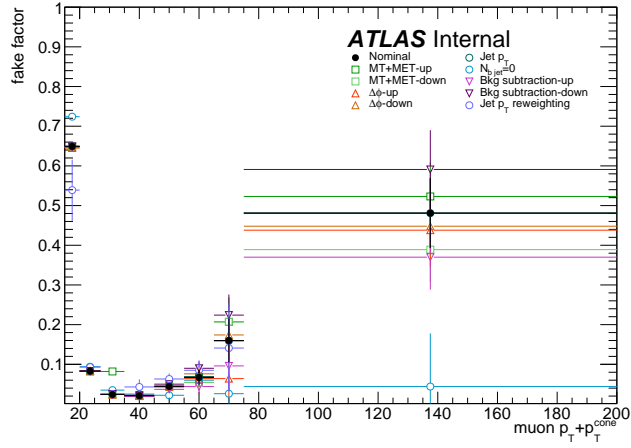


Figure 5.19: Systematic variations in the fake factor as a function of muon  $p_T + p_T^{\text{cone}}$ . The individual fake factors obtained for each systematic variation are displayed with their statistical uncertainties.

#### 1577 5.3.4.5 Results of the fake factor

1578 The fake background contribution in the signal region is estimated by applying the fake factors  
 1579 to the equivalent  $NL$  region using Equation 5.9, where the fake factor used corresponds to the  
 1580 flavor of the loose lepton in the event. As usual, the prompt background is subtracted from the  
 1581  $NL$  events using MC simulation. Charge misidentification is handled using the same method as  
 1582 in Section 5.3.3, with an additional set of charge flip rates calculated for loose leptons. The fake  
 1583 background yields in the signal region are listed in Table 5.15. An overall uncertainty of 50% is  
 1584 assigned to the fake background estimation in  $\mu^\pm\mu^\pm$  events, and between 40% to 90% for  $e^\pm e^\pm$  and  
 1585  $\mu^\pm e^\pm$  events, including both statistical and systematic effects.

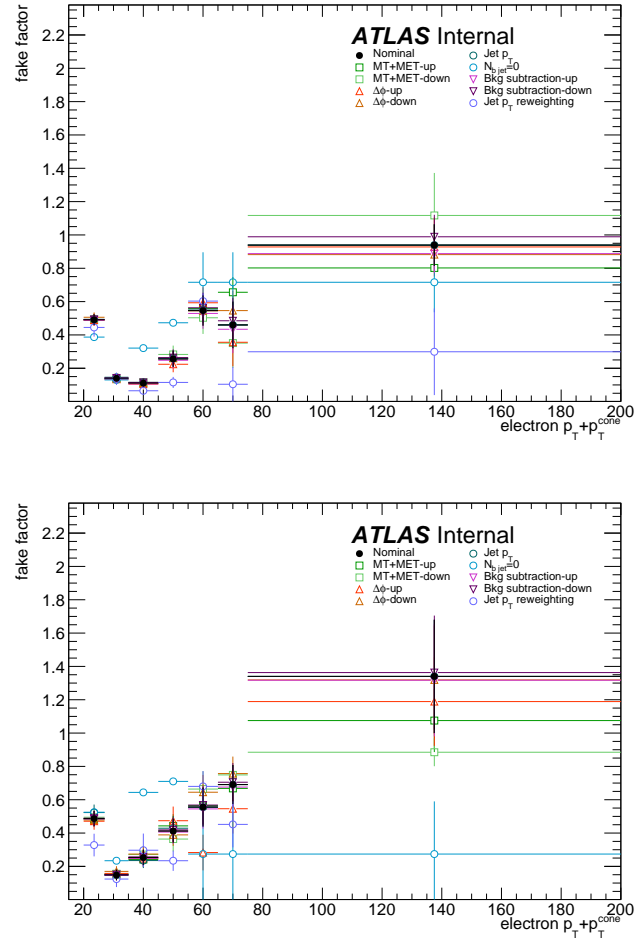


Figure 5.20: Systematic variations in the fake factor as a function of electron  $p_T + p_T^{\text{cone}}$  in the central ( $|\eta| < 1.37$ , top) and forward ( $|\eta| > 1.37$ , bottom) regions of the detector. The individual fake factors obtained for each systematic variation are displayed with their statistical uncertainties.

| fake factor            | $p_T[15, 20]$     | $p_T[20, 27]$     | $p_T[27, 35]$     | $p_T[35, 45]$     | $p_T[45, 55]$     | $p_T[55, 65]$     | $p_T[65, 75]$     | $p_T[75, 200]$    |
|------------------------|-------------------|-------------------|-------------------|-------------------|-------------------|-------------------|-------------------|-------------------|
| nominal                | $0.649 \pm 0.007$ | $0.083 \pm 0.002$ | $0.024 \pm 0.002$ | $0.021 \pm 0.003$ | $0.044 \pm 0.007$ | $0.067 \pm 0.018$ | $0.160 \pm 0.055$ | $0.481 \pm 0.088$ |
| MT+MET                 | $0.649 \pm 0.007$ | $0.082 \pm 0.002$ | $0.082 \pm 0.002$ | $0.020 \pm 0.003$ | $0.045 \pm 0.007$ | $0.068 \pm 0.018$ | $0.207 \pm 0.062$ | $0.523 \pm 0.086$ |
| $\Delta\phi(\ell, j)$  | $0.645 \pm 0.008$ | $0.083 \pm 0.003$ | $0.024 \pm 0.002$ | $0.021 \pm 0.004$ | $0.045 \pm 0.008$ | $0.064 \pm 0.021$ | $0.064 \pm 0.058$ | $0.438 \pm 0.092$ |
| Jet $p_T$              | $0.650 \pm 0.007$ | $0.083 \pm 0.002$ | $0.024 \pm 0.002$ | $0.021 \pm 0.003$ | $0.045 \pm 0.007$ | $0.069 \pm 0.018$ | $0.159 \pm 0.018$ | $0.481 \pm 0.088$ |
| $N_{b\text{-jet}} = 0$ | $0.724 \pm 0.003$ | $0.094 \pm 0.001$ | $0.035 \pm 0.001$ | $0.025 \pm 0.002$ | $0.022 \pm 0.004$ | $0.060 \pm 0.015$ | $0.026 \pm 0.053$ | $0.044 \pm 0.134$ |
| Bkg. subtraction       | $0.648 \pm 0.007$ | $0.083 \pm 0.002$ | $0.024 \pm 0.002$ | $0.019 \pm 0.003$ | $0.037 \pm 0.007$ | $0.044 \pm 0.019$ | $0.096 \pm 0.062$ | $0.370 \pm 0.082$ |
| Jet $p_T$ Reweighting  | $0.649 \pm 0.007$ | $0.083 \pm 0.002$ | $0.025 \pm 0.002$ | $0.022 \pm 0.003$ | $0.050 \pm 0.007$ | $0.090 \pm 0.017$ | $0.224 \pm 0.052$ | $0.591 \pm 0.099$ |
|                        | $0.539 \pm 0.077$ | $0.093 \pm 0.007$ | $0.025 \pm 0.004$ | $0.043 \pm 0.019$ | $0.063 \pm 0.014$ | $0.085 \pm 0.025$ | $0.141 \pm 0.110$ | $1.962 \pm 0.492$ |

(a) Fake factor for muons.

| fake factor            | $p_T[20, 27]$     | $p_T[27, 35]$     | $p_T[35, 45]$     | $p_T[45, 55]$     | $p_T[55, 65]$     | $p_T[65, 75]$     | $p_T[75, 200]$    |
|------------------------|-------------------|-------------------|-------------------|-------------------|-------------------|-------------------|-------------------|
| nominal                | $0.491 \pm 0.031$ | $0.140 \pm 0.020$ | $0.111 \pm 0.023$ | $0.256 \pm 0.049$ | $0.546 \pm 0.091$ | $0.460 \pm 0.140$ | $0.939 \pm 0.125$ |
| MT+MET                 | $0.493 \pm 0.030$ | $0.138 \pm 0.019$ | $0.115 \pm 0.022$ | $0.261 \pm 0.045$ | $0.559 \pm 0.084$ | $0.656 \pm 0.091$ | $0.802 \pm 0.016$ |
| $\Delta\phi(\ell, j)$  | $0.488 \pm 0.032$ | $0.137 \pm 0.020$ | $0.110 \pm 0.025$ | $0.283 \pm 0.053$ | $0.503 \pm 0.097$ | $0.351 \pm 0.149$ | $1.117 \pm 0.255$ |
| Jet $p_T$              | $0.489 \pm 0.035$ | $0.134 \pm 0.021$ | $0.105 \pm 0.025$ | $0.224 \pm 0.048$ | $0.593 \pm 0.093$ | $0.356 \pm 0.144$ | $0.928 \pm 0.177$ |
| $N_{b\text{-jet}} = 0$ | $0.506 \pm 0.029$ | $0.140 \pm 0.018$ | $0.111 \pm 0.022$ | $0.260 \pm 0.046$ | $0.545 \pm 0.084$ | $0.546 \pm 0.120$ | $0.882 \pm 0.103$ |
| Jet $p_T$              | $0.493 \pm 0.032$ | $0.146 \pm 0.021$ | $0.115 \pm 0.024$ | $0.259 \pm 0.049$ | $0.550 \pm 0.091$ | $0.460 \pm 0.140$ | $0.939 \pm 0.125$ |
| $N_{b\text{-jet}} = 0$ | $0.387 \pm 0.009$ | $0.130 \pm 0.008$ | $0.321 \pm 0.012$ | $0.473 \pm 0.015$ | $0.716 \pm 0.180$ | $0.716 \pm 0.180$ | $0.716 \pm 0.180$ |
| Bkg. subtraction       | $0.488 \pm 0.031$ | $0.138 \pm 0.020$ | $0.106 \pm 0.023$ | $0.248 \pm 0.049$ | $0.529 \pm 0.092$ | $0.434 \pm 0.143$ | $0.888 \pm 0.115$ |
| Jet $p_T$ Reweighting  | $0.493 \pm 0.031$ | $0.142 \pm 0.020$ | $0.115 \pm 0.023$ | $0.264 \pm 0.049$ | $0.563 \pm 0.090$ | $0.485 \pm 0.136$ | $0.989 \pm 0.132$ |
|                        | $0.445 \pm 0.055$ | $0.137 \pm 0.037$ | $0.065 \pm 0.023$ | $0.115 \pm 0.033$ | $0.603 \pm 0.047$ | $0.104 \pm 0.105$ | $0.299 \pm 0.260$ |

(b) Fake factor for central electrons ( $|\eta| < 1.37$ ).

| fake factor            | $p_T[20, 27]$     | $p_T[27, 35]$     | $p_T[35, 45]$     | $p_T[45, 55]$     | $p_T[55, 65]$     | $p_T[65, 75]$     | $p_T[75, 200]$    |
|------------------------|-------------------|-------------------|-------------------|-------------------|-------------------|-------------------|-------------------|
| nominal                | $0.487 \pm 0.046$ | $0.148 \pm 0.031$ | $0.253 \pm 0.046$ | $0.412 \pm 0.071$ | $0.556 \pm 0.117$ | $0.691 \pm 0.117$ | $1.340 \pm 0.340$ |
| MT+MET                 | $0.483 \pm 0.045$ | $0.152 \pm 0.031$ | $0.241 \pm 0.043$ | $0.443 \pm 0.070$ | $0.565 \pm 0.106$ | $0.668 \pm 0.117$ | $1.075 \pm 0.189$ |
| $\Delta\phi(\ell, j)$  | $0.495 \pm 0.047$ | $0.156 \pm 0.033$ | $0.271 \pm 0.052$ | $0.364 \pm 0.074$ | $0.664 \pm 0.107$ | $0.749 \pm 0.056$ | $0.885 \pm 0.084$ |
| Jet $p_T$              | $0.471 \pm 0.051$ | $0.158 \pm 0.035$ | $0.247 \pm 0.051$ | $0.474 \pm 0.085$ | $0.283 \pm 0.107$ | $0.546 \pm 0.149$ | $1.189 \pm 0.266$ |
| $N_{b\text{-jet}} = 0$ | $0.478 \pm 0.042$ | $0.170 \pm 0.031$ | $0.274 \pm 0.046$ | $0.389 \pm 0.066$ | $0.645 \pm 0.104$ | $0.757 \pm 0.102$ | $1.319 \pm 0.326$ |
| Jet $p_T$              | $0.523 \pm 0.048$ | $0.149 \pm 0.033$ | $0.235 \pm 0.045$ | $0.429 \pm 0.073$ | $0.555 \pm 0.117$ | $0.691 \pm 0.117$ | $1.340 \pm 0.340$ |
| $N_{b\text{-jet}} = 0$ | $0.525 \pm 0.011$ | $0.234 \pm 0.013$ | $0.644 \pm 0.016$ | $0.710 \pm 0.014$ | $0.274 \pm 0.316$ | $0.274 \pm 0.316$ | $0.274 \pm 0.316$ |
| Bkg. subtraction       | $0.484 \pm 0.046$ | $0.146 \pm 0.031$ | $0.248 \pm 0.046$ | $0.406 \pm 0.071$ | $0.545 \pm 0.118$ | $0.676 \pm 0.118$ | $1.317 \pm 0.337$ |
| Jet $p_T$ Reweighting  | $0.489 \pm 0.046$ | $0.151 \pm 0.031$ | $0.257 \pm 0.046$ | $0.419 \pm 0.071$ | $0.568 \pm 0.117$ | $0.705 \pm 0.115$ | $1.363 \pm 0.342$ |
|                        | $0.328 \pm 0.068$ | $0.124 \pm 0.048$ | $0.297 \pm 0.100$ | $0.234 \pm 0.061$ | $0.680 \pm 0.092$ | $0.452 \pm 0.138$ | $2.385 \pm 1.729$ |

(c) Fake factor for forward electrons ( $1.37 < |\eta|$ ).Table 5.14: Values of the fake factor in each  $p_T$  bin and for each individual systematic source.

|                   | estimated yield  | $f_e$ stat. up | $f_e$ stat. dn | $f_e$ syst. up | $f_e$ syst. dn | $f_\mu$ stat. up | $f_\mu$ stat. dn | $f_\mu$ syst. up | $f_\mu$ syst. dn |
|-------------------|------------------|----------------|----------------|----------------|----------------|------------------|------------------|------------------|------------------|
| $e^\pm e^\pm$     | $11.42 \pm 3.13$ | —              | —              | —              | —              | —                | —                | —                | —                |
| $\mu^\pm \mu^\pm$ | $4.82 \pm 0.77$  | —              | —              | —              | —              | $0.65$           | $-0.65$          | $3.64$           | $-0.61$          |
| $\mu^\pm e^\pm$   | $37.08 \pm 5.16$ | $4.90$         | $-4.90$        | $5.59$         | $-14.34$       | $1.39$           | $-1.39$          | $16.10$          | $-1.98$          |

Table 5.15: Estimated yields for the fake lepton background. The estimated yield is shown in the first column together with the statistical uncertainty followed by the systematic uncertainties from variations of the the fake factors within their statistical (stat.) and systematic (syst.) uncertainties. The labels  $f_e$  and  $f_\mu$  indicate the fake factors for electrons and muons, respectively.

1586 **5.3.4.6 Validation of the fake factor**

1587 The accuracy of the fake factor method is tested in several validation regions, the most sensitive  
 1588 of which is the same-sign top fakes VR (SS top VR), defined in Table 5.16. This region inverts  
 1589 the signal region's  $b$ -jet veto to accept events with exactly one  $b$ -jet. Due to this requirement, the  
 1590 dominant source of events comes from the  $t\bar{t}$  process where a  $b$ -jet fakes an isolated lepton. The  
 1591 distribution of the subleading lepton  $p_T$  in this VR is shown in Figure 5.21 for all lepton flavor  
 1592 combinations. There is good agreement between the data and the prediction, even when only taking  
 1593 into account the statistical uncertainty and not the large systematic uncertainties assigned to the  
 1594 fake estimation.

| Same-sign inclusive VR                                   |
|--|
| Exactly 2 same-sign signal leptons                       |
| $p_T > 27$ GeV for both leptons                          |
| $m_{ll} > 20$ GeV  |
| $ m_{ee} - m_Z  > 15$ GeV ( $e^\pm e^\pm$ -channel only) |
| $N_{b\text{-jet}} = 1$                                   |
| $N_{\text{jet}} \geq 2$                                  |
| Leading jet $p_T > 65$ GeV                               |
| Subleading jet $p_T > 35$ GeV                            |

Table 5.16: Selection criteria for the same-sign top fakes validation region.

1595 **5.3.5 Reduction of  $WZ$  background using custom overlap removal**

1596 The dominant source of prompt background in this analysis comes from  $WZ$  events where both  
 1597 bosons decay leptonically. Traditionally, the background is dealt with by imposing a veto on any  
 1598 event with a third lepton passing some loose identification criteria (the so-called *trilepton veto*). In  
 1599 the case of this analysis, if one or more leptons (in addition to the two signal leptons) passed the  
 1600 preselection criteria, the event would be rejected. However,  $WZ$  events can still enter the signal  
 1601 region if one of the leptons fails the veto selection or falls outside of the detector's acceptance.

1602 In order to understand the sources of  $WZ$  events that are not removed by the trilepton veto,  
 1603 a study was performed on truth-level leptons<sup>16</sup> on  $W^\pm W^\pm jj$  and  $WZ$  MC samples. Events with  
 1604 three truth leptons were selected, and each was matched to its reconstruction-level partner by finding  
 1605 the closest  $\Delta R(\text{truth}, \text{reco})$  and  $\Delta p_{T,\text{truth},\text{reco}}$  match. For events surviving the trilepton veto, the  
 1606 two signal leptons were removed, and the remaining leptons represent real leptons that failed to

<sup>16</sup>Truth particles are the particles produced directly by the MC generator before being passed through the full detector simulation, at which point they are considered *reconstruction-level* (or *reco-level*) particles.

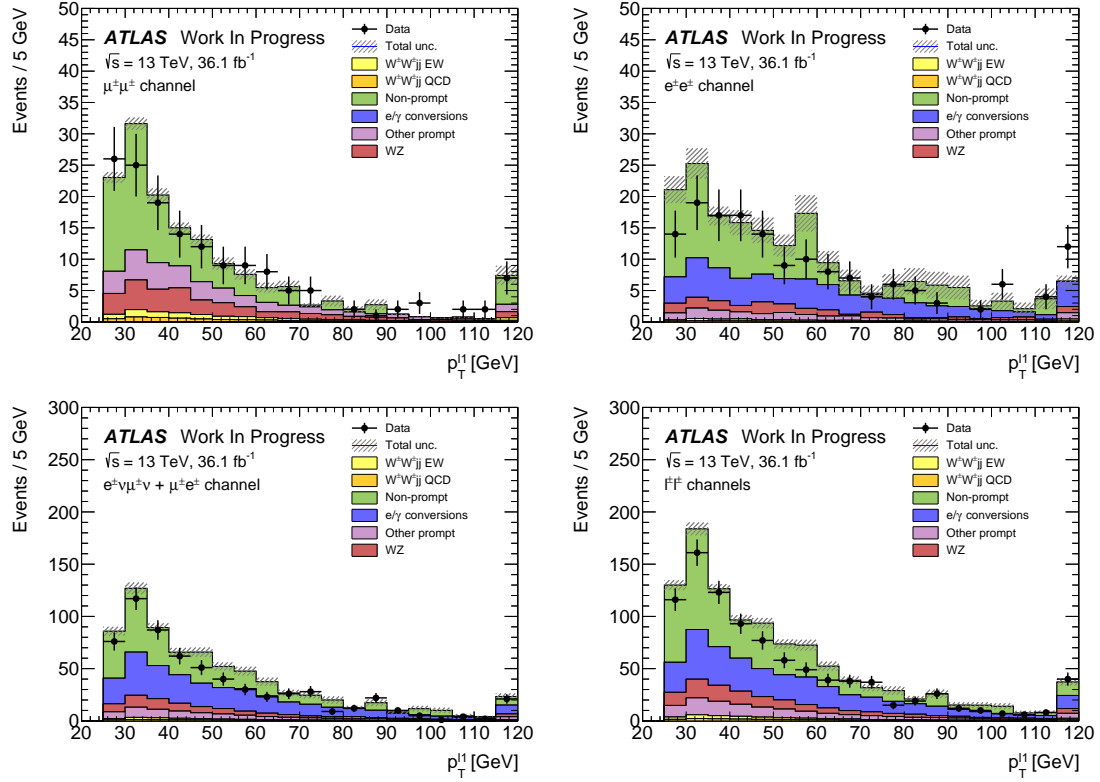


Figure 5.21: Distributions of the subleading lepton  $p_T$  in the same-sign top fakes VR for  $\mu^\pm\mu^\pm$  events (top right),  $e^\pm e^\pm$  events (top left),  $\mu^\pm e^\pm$  events (bottom left), and all events combined (bottom right). All errors are statistical only.

be selected for the veto. Between 40-50% of these leptons fell outside of the eta acceptance of the analysis (see Figure 5.22) and were unrecoverable. The second largest source of leptons failing the preselection was the OR, defined in Section 5.2.1.4. The standard OR procedure appeared to be too aggressive in removing leptons in favor of jets, causing many three lepton events to “lose” their third lepton and pass the trilepton veto. Therefore a *custom OR* was investigated which would replace the standard OR in the preselection and allow for better  $WZ$  rejection by removing fewer third leptons.

In order to construct this custom OR, a new quantity is defined between a lepton ( $l$ ) and a nearby jet ( $j$ )

$$p_{T,\text{ratio}}(l, j) = \frac{p_{Tl}}{p_{Tj}} \quad (5.13)$$

which, along with  $\Delta R(l, j)$ , will allow for more third leptons to pass the preselection. The idea behind including  $p_{T,\text{ratio}}$  is to be able to preferentially remove background leptons originating from

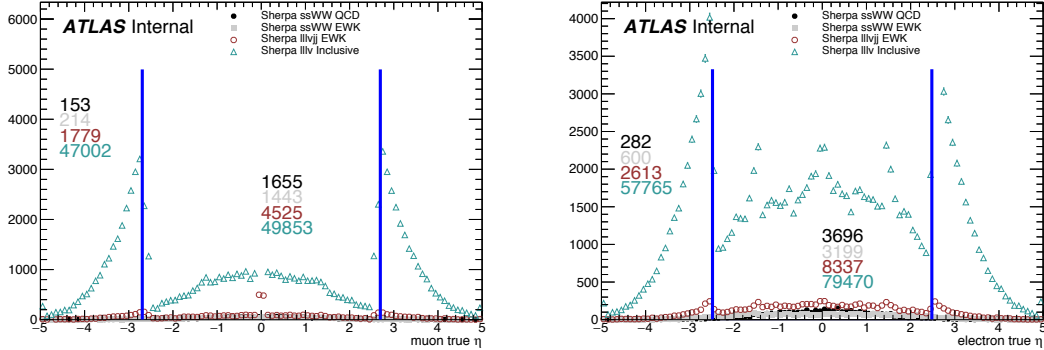


Figure 5.22: Pseudorapidity ( $\eta$ ) distributions of truth muons (top) and electrons (bottom) for Sherpa  $W^\pm W^\pm jj$  and  $WZ$  MC samples. The blue vertical lines represent the allowed  $\eta$  range for each lepton flavor. The numbers correspond to the number of raw MC events that fall within and outside of the allowed  $\eta$  range for each MC sample.

1618 jets (i.e. those that carry a low percentage of the total jet momentum) instead of removing *any*  
 1619 lepton near a jet. The distributions of  $p_{T,\text{ratio}}$  and the associated efficiency curves for muons and  
 1620 electrons can be found in Figures 5.23 and 5.25, respectively, and the distributions for  $\Delta R(\mu, j)$  for  
 1621 muons can be found in Figure 5.24. Since all electrons have an associated jet in the calorimeters,  
 1622 the  $\Delta R(e, j)$  variable is not a good quantity to use for this custom OR.

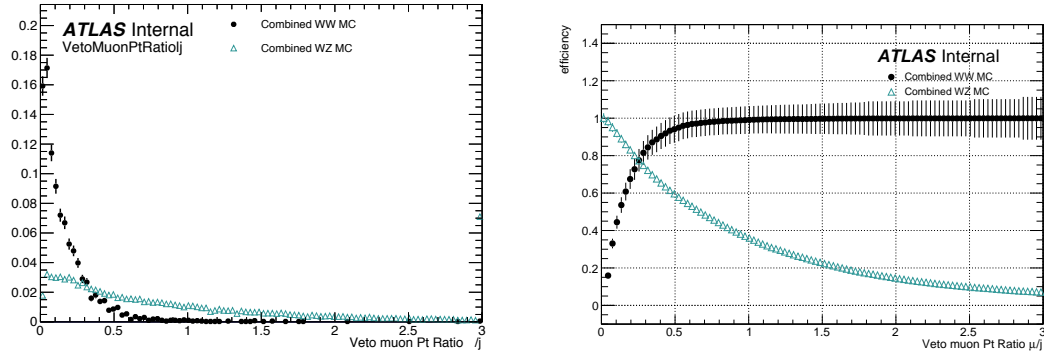


Figure 5.23: Distributions of  $p_{T,\text{ratio}}(\mu, j)$  for EWK and QCD  $W^\pm W^\pm jj$  signal (black) and  $WZ$  background (teal) for truth-matched third muons in events that pass the trilepton veto. Both distributions are normalized to unit area. The associated efficiency curves are on the right where efficiency is defined as the percentage of total events that would pass a cut on  $p_{T,\text{ratio}}(\mu, j)$  at a given value on the  $x$ -axis.

1623 A workingpoint for the Custom OR was chosen by requiring 90% signal retention for muons  
 1624 and 90% background rejection for electrons. The cut on electrons was allowed to be much tighter

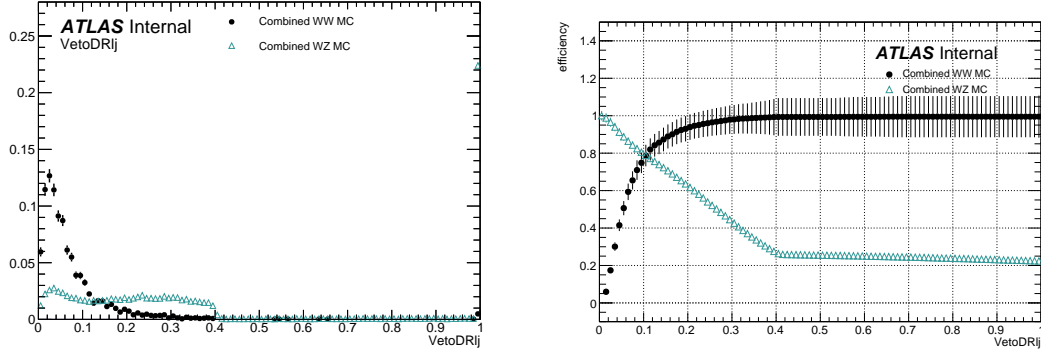


Figure 5.24: Distributions of  $\Delta R(\mu, j)$  for EWK and QCD  $W^\pm W^\pm jj$  signal (black) and  $WZ$  background (teal) for truth-matched third muons in events that pass the trilepton veto. Both distributions are normalized to unit area. The associated efficiency curves are on the right where efficiency is defined as the percentage of total events that would pass a cut on  $\Delta R(\mu, j)$  at a given value on the  $x$ -axis.

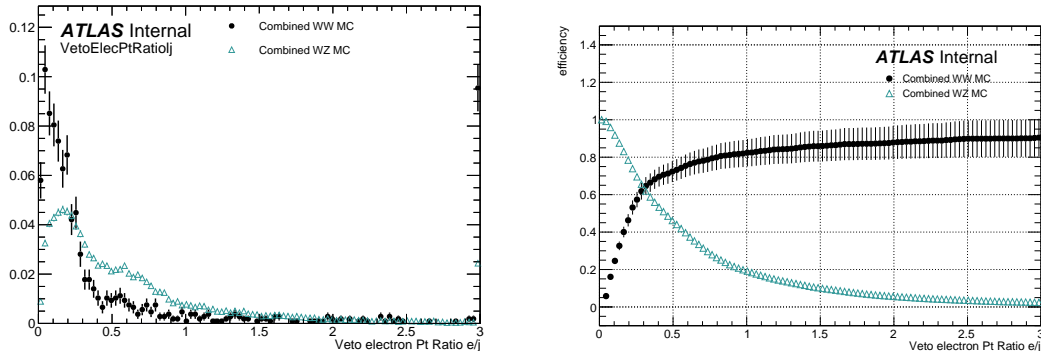


Figure 5.25: Distributions of  $p_{T,\text{ratio}}(e, j)$  for EWK and QCD  $W^\pm W^\pm jj$  signal (black) and  $WZ$  background (teal) for truth-matched third electrons in events that pass the trilepton veto. Both distributions are normalized to unit area. The associated efficiency curves are on the right where efficiency is defined as the percentage of total events that would pass a cut on  $p_{T,\text{ratio}}(e, j)$  at a given value on the  $x$ -axis.

because the number of signal events with a third electron is considerably smaller than for muons. It should be emphasized that the signal events present in Figures 5.23-5.25 do not represent the full set of signal events, but only those with a real third lepton (which must come from some source other than the signal  $W^\pm W^\pm jj$  process). For muons, a logical ‘or’ of  $p_{T,\text{ratio}}(\mu, j)$  and  $\Delta R(\mu, j)$  is used to maximize the third lepton acceptance due to correlations between the quantities, as shown in Figure 5.26; for electrons, only a cut on  $p_{T,\text{ratio}}(e, j)$  is used. The Custom OR workingpoint is outlined in Table 5.17.

| Custom OR Definition |  |
|----------------------|--|
| Muons                | $p_{T,\text{ratio}}(\mu, j) > 0.40$ or $\Delta R(\mu, j) > 0.15$ |
| Electrons            | $p_{T,\text{ratio}}(e, j) > 0.18$                                |

Table 5.17: Custom OR definition. Leptons must pass this selection in order to be counted for the trilepton veto.

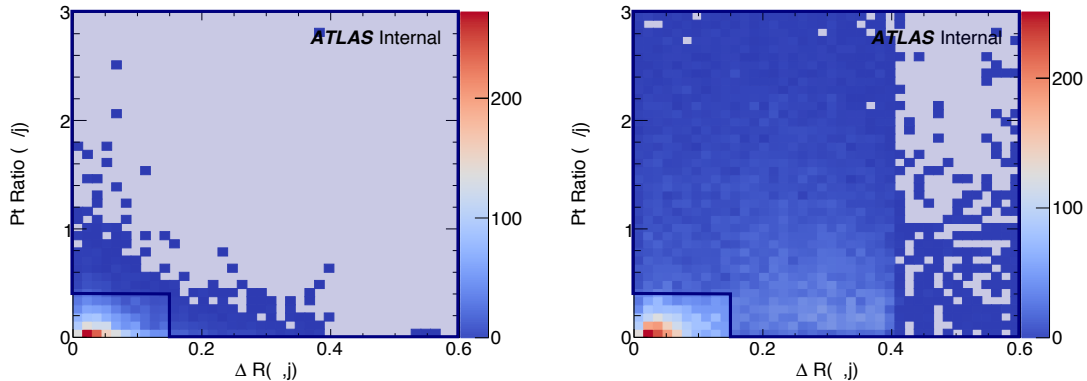


Figure 5.26: Two-dimensional plots of  $p_{T,\text{ratio}}(\mu, j)$  vs  $\Delta R(\mu, j)$  for truth-matched third muons in events that pass the trilepton veto for EWK and QCD  $W^\pm W^\pm jj$  signal (left) and  $WZ$  background (right). The blue overlay indicates the area in which the third leptons will pass the custom OR and result in the event failing the trilepton veto.

Tests of the performance of the Custom OR yield promising results, with approximately 20% reduction in  $WZ$  background compared to less than 2% signal loss in the signal region. Unfortunately, due to differences between the primary analysis framework and the one used for testing, in practice the gains in  $WZ$  rejection are not nearly as substantial, and ultimately the Custom OR is not included in the final analysis. However, it is still a potentially useful tool for improving background rejection via lepton number vetoes in analyses with overly aggressive OR procedures.

---

1638 **5.4 Cross section measurement**

1639 The  $W^\pm W^\pm jj$  EWK cross section is extracted from the signal region using a maximum-likelihood  
1640 fit applied simultaneously to four  $m_{jj}$  bins in the signal region as well as to the low- $m_{jj}$  and  $WZ$   
1641 control regions. For the fit and cross section extraction, the signal region is defined as in Table 5.8  
1642 with the dijet invariant mass requirement raised to  $m_{jj} > 500$  GeV. The low- $m_{jj}$  region is defined  
1643 to mirror the signal region exactly with the dijet invariant mass inverted to  $200 < m_{jj} < 500$  GeV,  
1644 and the  $WZ$  control region is defined previously in Section 5.3.1.

1645 The signal and low- $m_{jj}$  regions are split into six channels based on the flavor and charge of  
1646 the dilepton pair:  $\mu^+\mu^+$ ,  $\mu^-\mu^-$ ,  $\mu^+e^+$ ,  $\mu^-e^-$ ,  $e^+e^+$ , and  $e^-e^-$ . This split by charge increases the  
1647 sensitivity of the measurement due to the  $W^+/W^-$  charge asymmetry at hadron colliders favoring  
1648 the production of  $W^+$  bosons [80]. Since the signal events contain two  $W$  bosons, the signal strength  
1649 compared to charge-symmetric backgrounds is much greater in the  $++$  channels for both charges  
1650 combined. The  $WZ$  control region is included in the fit as a single bin ( $l^\pm l^\pm l^\pm$ ).

1651 The maximum likelihood fit and cross section extractions are outlined in Sections 5.4.1 and  
1652 5.4.3, respectively. The results of the cross section measurement and of the analysis as a whole are  
1653 presented in Section 5.6.

1654 **5.4.1 Maximum likelihood fit**

1655 TODO: This section is very similar to what is written in the support note... May need to put  
1656 some work into flushing it out so it's not so close to copy-paste The number of predicted signal  
1657 events in each channel  $c$  and  $m_{jj}$  bin  $b$  can be calculated from the SM predicted signal cross section  
1658  $\sigma_{\text{theo}}^{\text{tot}}$ , the total integrated luminosity  $\mathcal{L}$ , the signal acceptance  $\mathcal{A}$ , and the efficiency corrections  $\mathcal{C}(\theta)$ ,  
1659 where  $\theta$  represents the set of nuisance parameters that parameterize the effects of each systematic  
1660 uncertainty on the signal and background expectations. The acceptance and efficiency corrections  
1661 will be covered in more detail in Section 5.4.2.

$$N_{cb}^{\text{sig}}(\theta) = \sigma_{\text{theo}}^{\text{tot}} \mathcal{A}_b \mathcal{C}_b(\theta) \mathcal{L} \quad (5.14)$$

1662 A signal strength parameter  $\mu$  is defined as the ratio of the measured cross section to the SM  
1663 predicted cross section. The expected number of events in a given channel and bin can then be  
1664 expressed as the sum of the estimated background ( $N_{cb}^{\text{bkg}}(\theta)$ ) and the number of predicted signal

1665 events scaled by  $\mu$ :

$$\begin{aligned} N_{cb}^{\text{exp}}(\theta) &= \mu N_{cb}^{\text{sig}}(\theta) + N_{cb}^{\text{bkg}}(\theta) \\ &= \mu \sigma_{\text{theo}}^{\text{tot}} \mathcal{A}_b \mathcal{C}_b(\theta) \mathcal{L} + N_{cb}^{\text{bkg}}(\theta) \end{aligned} \quad (5.15)$$

1666 The nuisance parameters are constrained by Gaussian probability distribution functions, and  
 1667 the normalization of the  $WZ$  background mentioned in Section 5.3.1 is included in the fit as a free  
 1668 parameter. The expected yields for signal and background processes are adjusted by the set of  
 1669 nuisance parameters within the constraints of the systematic uncertainties. The yields after the fit  
 1670 correspond to the value that best matches the observed data.

1671 The number of events per channel and bin after the fit can be written as a sum of the predicted  
 1672 event yields for each sample  $s$ :

$$\nu_{cb}(\phi, \theta, \gamma_{cb}) = \gamma_{cb} \sum_s [\eta_{cs}(\theta) \phi_{cs}(\theta) \lambda] h_{cbs}(\theta) \quad (5.16)$$

1673 In this equation, the fitted number of events in a given channel and bin is obtained by weighting  
 1674 the histogram of predicted yields  $h_{cbs}$  by the product of a given luminosity  $\lambda$  and any normalization  
 1675 factors  $\phi_{cs}$  that may be given for each channel and sample. The input histogram and the normaliza-  
 1676 tion factors may depend on the nuisance parameters  $\theta$  taking into account sources of systematic  
 1677 uncertainty. Uncertainties on the normalization factors  $\eta_{cs}(\theta)$  are also included. Finally, bin-by-bin  
 1678 scale factors  $\gamma_{cb}$  are included to parameterize the statistical uncertainties of the MC predictions.

1679 The binned likelihood function is given by a product of Gaussian functions for the luminosity  
 1680 and for the background uncertainties and a product of Poisson functions for the number of observed  
 1681 events in each bin and channel:

$$L(\mu|\theta) = \mathcal{G}(\mathcal{L}|\theta_{\mathcal{L}}, \sigma_{\mathcal{L}}) \cdot \prod_c \prod_b \mathcal{P}(N_{cb}^{\text{meas.}}|\nu_{cb}(\mu)) \prod_p \mathcal{G}(\theta_p^0|\theta_p) \quad (5.17)$$

1682 where  $\mathcal{G}$  and  $\mathcal{P}$  are the Gaussian and Poisson functions, respectively. As before,  $\mathcal{L}$  represents the  
 1683 integrated luminosity with uncertainty  $\sigma_{\mathcal{L}}$  and associated nuisance parameter  $\theta_{\mathcal{L}}$ . The number of  
 1684 measured events in a given bin and channel is represented by  $N_{cb}^{\text{meas.}}$ , and  $\nu_{cb}(\mu)$  is the predicted  
 1685 number of events defined in Equation 5.16 expressed as a function of the signal strength  $\mu$ . Finally,  
 1686 the set of nuisance parameters  $\theta$  and any auxiliary measurements used to constrain them  $\theta^0$  are  
 1687 multiplied for each parameter  $p$ .

1688 The profile likelihood ratio is defined as

$$q_{\mu} = -2 \ln \frac{L(\mu, \hat{\theta}_{\mu})}{L(\hat{\mu}, \hat{\theta})} \quad (5.18)$$

1689 with  $\hat{\mu}$  and  $\hat{\theta}$  as the unconditional maximum likelihood estimates and  $\hat{\hat{\theta}}$  as the conditional maximum  
 1690 likelihood estimate for a given value of  $\mu$ . The fitted signal strength  $\hat{\mu}$  is obtained by maximizing  
 1691 the likelihood function with respect to all parameters. The compatibility of the observed data  
 1692 with the background-only hypothesis can then be calculated by setting  $\mu = 0$ . Observation of the  
 1693  $W^\pm W^\pm jj$  EWK process is claimed if the data is found to be inconsistent with the background-only  
 1694 hypothesis by more than  $5\sigma$ .

#### 1695 5.4.2 Definition of the fiducial volume

1696 Before extracting the cross section, it is necessary to define the fiducial volume, or the phase space  
 1697 of measureable events. It is a subset of the total phase space defined by selection requirements  
 1698 designed to mirror those applied in the analysis as closely as possible. The selection criteria for the  
 1699 fiducial volume are listed in Table 5.18.

| Fiducial region selection |  |
|---------------------------|--|
| Lepton selection          | Two prompt leptons ( $e, \mu$ )<br>$p_T > 27$ GeV and $ \eta  < 2.5$ for both leptons<br>Both leptons with the same electric charge<br>Dilepton invariant mass $m_{ll} > 20$ GeV<br>Dilepton separation $\Delta R(ll) > 0.3$                                       |
| Missing transverse energy | Two neutrino system with $p_T^{\nu\nu} > 30$ GeV   |
| Jet selection             | At least two jets<br>Leading jet $p_T > 65$ GeV<br>Subleading jet $p_T > 35$ GeV<br>Leading and subleading jet $ \eta  < 4.5$<br>Jet-lepton separation $\Delta R(l, j) > 0.3$<br>Dijet invariant mass $m_{jj} > 500$ GeV<br>Dijet separation $\Delta y_{jj} > 2.0$ |

Table 5.18: Definition of the fiducial volume.

1700 In MC simulations, the total phase space is generated, providing the total theoretical cross section  
 1701  $\sigma_{\text{theo}}^{\text{tot}}$  and the total number of signal events  $\mathcal{N}_{\text{sig}}^{\text{tot}}$ <sup>17</sup>. After applying the fiducial selection at truth  
 1702 level, the total number of signal events in the fiducial region  $\mathcal{N}_{\text{sig}}^{\text{fid}}$  is obtained. An acceptance factor  
 1703  $\mathcal{A}$  is used to represent the efficiency of events falling in the fiducial region at truth level:

$$\mathcal{A} = \frac{\mathcal{N}_{\text{sig}}^{\text{fid}}}{\mathcal{N}_{\text{sig}}^{\text{tot}}} \quad (5.19)$$

<sup>17</sup>For the purpose of clarity, the number of events at truth level is represented by a script  $\mathcal{N}$ , and the number of events at reconstruction level uses a regular  $N$ .

1704 A correction factor  $\mathcal{C}$  is also necessary to translate from the truth level fiducial volume to the  
 1705 reconstruction level signal region and is defined in terms of the number of reconstruction level MC  
 1706 events in the signal region  $N_{\text{sig},\text{MC}}^{\text{SR}}$ :

$$\mathcal{C} = \frac{N_{\text{sig},\text{MC}}^{\text{SR}}}{N_{\text{sig}}^{\text{fid}}} \quad (5.20)$$

1707 Since the fit is binned in  $m_{jj}$ , the acceptance and efficiency correction factors need to be as well.  
 1708 Therefore,  $\mathcal{A}_i$  and  $\mathcal{C}_{ij}$  are written in terms of truth  $m_{jj}$  bins  $i$  and reconstruction  $m_{jj}$  bins  $j$ . A  
 1709 graphical representation of these regions and the use of the acceptance and correction factors can  
 1710 be seen in Figure 5.27.

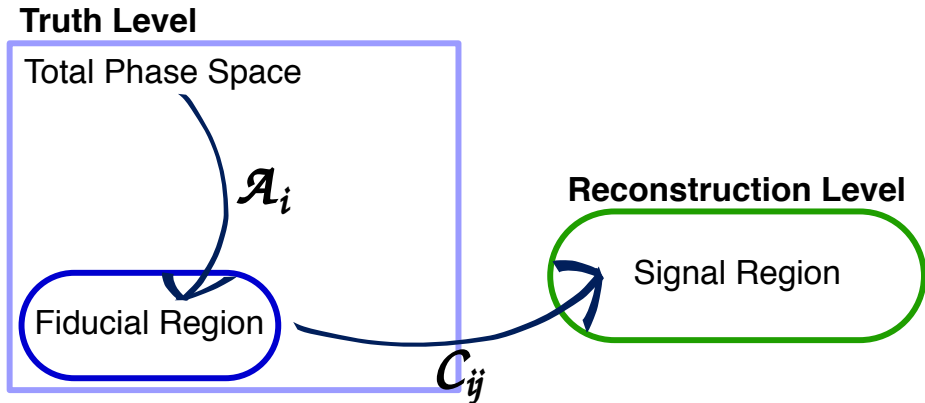


Figure 5.27: Visual representation of the different kinematic regions relevant to the cross section measurement. The acceptance factor  $\mathcal{A}$  converts from the truth level total phase space to the truth level fiducial region, and the efficiency correction  $\mathcal{C}$  translates the fiducial region into the reconstruction level signal region.

#### 1711 5.4.3 Cross section extraction

1712 The  $W^\pm W^\pm jj$  EWK fiducial cross section is measured using the signal strength parameter  $\mu$  that is  
 1713 determined by the maximum likelihood fit. This parameter is dependent on the nuisance parameters  
 1714  $\theta$  and can be written explicitly in terms of the measured and theoretical cross sections as:

$$\mu(\theta) = \frac{\sigma_{\text{meas}}^{\text{SR}}}{\sigma_{\text{theo}}^{\text{SR}}} \quad (5.21)$$

1715 In the simple case with only one bin, the equation for the total number of expected events in the  
 1716 signal region first introduced in Equation 5.15 can be written as:

$$N_{\text{exp}}^{\text{SR}}(\theta) = \mu(\theta) \cdot \sigma_{\text{theo}}^{\text{tot}} \cdot \mathcal{L} \cdot \mathcal{A} \cdot \mathcal{C}(\theta) + N_{\text{bkg}}^{\text{SR}}(\theta) \quad (5.22)$$

1717 with the non-binned versions of  $\mathcal{A}$  and  $\mathcal{C}$  defined in Equations 5.19 and 5.20, respectively.

1718 If the measured fiducial cross section is written as:

$$\sigma_{\text{meas}}^{\text{fid}} = \mu \cdot \mathcal{A} \cdot \sigma_{\text{theo}}^{\text{tot}} \quad (5.23)$$

1719 then Equation 5.22 can be rearranged to read:

$$\sigma_{\text{meas}}^{\text{fid}} = \frac{N_{\text{exp}}^{\text{SR}}(\theta) - N_{\text{bkg}}^{\text{SR}}(\theta)}{\mathcal{L} \cdot \mathcal{C}(\theta)} \quad (5.24)$$

1720 The measured fiducial cross section can finally be rewritten in terms of  $\hat{\mu}$ , which is the best estimator  
1721 of the signal strength as extracted from the fit:

$$\begin{aligned} \sigma_{\text{meas}}^{\text{fid}} &= \hat{\mu}(\theta) \cdot \sigma_{\text{theo}}^{\text{tot}} \cdot \mathcal{A} \\ &= \hat{\mu}(\theta) \cdot \sigma_{\text{theo}}^{\text{fid}} \end{aligned} \quad (5.25)$$

1722 In practice, however, the cross section is not extracted from a single bin, and Equation 5.22  
1723 becomes for a single channel in truth and reconstruction level  $m_{jj}$  bins  $i$  and  $j$ , respectively:

$$N_{\text{exp}}^{\text{SR}}(\theta) = \mu(\theta) \cdot \sigma_{\text{theo}}^{\text{tot}} \cdot \mathcal{L} \cdot \sum_i \mathcal{A}_i \cdot \sum_j \mathcal{C}_{ij} + \sum_j N_{\text{bkg},j}^{\text{SR}}(\theta) \quad (5.26)$$

1724 where now the binned versions of  $\mathcal{A}_i$  and  $\mathcal{C}_{ij}$  are used. This equation can be extended to include all  
1725 the analysis channels by increasing the number of bins  $i$  and  $j$ . Additionally, it can be shown that  
1726 Equation 5.25 holds for this more complex case as well [50], provided care is taken to ensure that  
1727 all the uncertainties are handled properly.

## 1728 5.5 Summary of uncertainties

1729 Systematic uncertainties enter the final fit as nuisance parameters which can impact the estimated  
1730 signal and background yields and the shapes of the  $m_{jj}$  distributions. These uncertainties can arise  
1731 from the experimental methods or from the theoretical calculations used in the analysis. This section  
1732 summarizes the systematic uncertainties; the experimental uncertainties are detailed in Section 5.5.1,  
1733 and the theoretical uncertainties are covered in Section 5.5.2. The impacts of the systematic uncer-  
1734 tainties on the final cross section measurement are summarized in Table 5.19.

### 1735 5.5.1 Experimental uncertainties

1736 Experimental uncertainties include detector effects as well as uncertainties on the background es-  
1737 timation methods. Sources of systematic uncertainty on the measurement of physics objects are

| Source                          | Impact [%] |
|---------------------------------|------------|
| Reconstruction                  | $\pm 4.0$  |
| Electrons                       | $\pm 0.5$  |
| Muons                           | $\pm 1.2$  |
| Jets and $E_T^{\text{miss}}$    | $\pm 2.8$  |
| $b$ -tagging                    | $\pm 2.0$  |
| Pileup                          | $\pm 1.5$  |
| Background                      | $\pm 5.0$  |
| Misid. leptons                  | $\pm 3.9$  |
| Charge misrec.                  | $\pm 0.3$  |
| $WZ$                            | $\pm 1.3$  |
| $W^\pm W^\pm jj$ QCD            | $\pm 2.8$  |
| Other                           | $\pm 0.8$  |
| Signal                          | $\pm 3.6$  |
| Interference                    | $\pm 1.0$  |
| EW Corrections                  | $\pm 1.3$  |
| Shower, Scale, PDF & $\alpha_s$ | $\pm 3.2$  |
| Total                           | $\pm 7.4$  |

Table 5.19: Impact of various systematic effects on the fiducial cross section measurement. The impact of a given source of uncertainty is computed by performing the fit with the corresponding nuisance parameter varied up or down by one standard deviation from its nominal value.

1738 listed in Table 5.20, grouped by the relevant object type. For backgrounds estimated from MC  
 1739 simulations, variations in these sources of uncertainty are propagated through the analysis to obtain  
 1740 the corresponding uncertainties on the event yields. Additional experimental uncertainties include  
 1741 the integrated luminosity, the photon conversion rate from Section 5.3.2, and the data driven charge  
 1742 misidentification and fake lepton background estimations from Sections 5.3.3 and 5.3.4.5, respec-  
 1743 tively.

1744 The largest sources of experimental uncertainty on the MC estimations come from the jet-related  
 1745 uncertainties and the  $b$ -tagging efficiency, while the largest uncertainty on the background estimation  
 1746 comes from the fake factor. The effects of the uncertainties on the  $W^\pm W^\pm jj$  EWK signal and the  
 1747 dominant MC estimated background,  $WZ$ , are listed in Tables 5.21 and 5.22, respectively. Since  
 1748 the overall contributions from other processes estimated with MC are small, the uncertainties on  
 1749 these backgrounds have a lesser impact on the final measurement; these tables can be found in  
 1750 Appendix A.1.

| Experimental uncertainties |                                 |
|----------------------------|---------------------------------|
| Electrons                  | Energy resolution               |
|                            | Energy scale                    |
|                            | Identification efficiency       |
|                            | Isolation efficiency            |
|                            | Reconstruction efficiency       |
|                            | Trigger efficiency              |
| Muons                      | Energy scale                    |
|                            | Identification efficiency       |
|                            | Inner detector track resolution |
|                            | Muon spectrometer resolution    |
|                            | Trigger efficiency              |
| $E_T^{\text{miss}}$        | Resolution                      |
|                            | Scale                           |
| Jets                       | Energy resolution               |
|                            | Energy scale                    |
|                            | JVT cut efficiency              |
|                            | $b$ -tagging efficiency         |
|                            | Jets from pileup                |

Table 5.20: List of sources of experimental uncertainties on the reconstruction of physics objects.

| $W^\pm W^\pm jj$ EWK      | $e^\pm e^\pm$ % Yield | $\mu^\pm e^\pm$ % Yield | $\mu^\pm \mu^\pm$ % Yield |
|---------------------------|-----------------------|-------------------------|---------------------------|
| Jet-related Uncertainties | 2.28                  | 2.22                    | 2.28                      |
| $b$ -tagging efficiency   | 1.81                  | 1.76                    | 1.74                      |
| Pile-up                   | 0.48                  | 0.97                    | 2.42                      |
| Trigger efficiency        | 0.02                  | 0.08                    | 0.47                      |
| Lepton reconstruction/ID  | 1.45                  | 1.14                    | 1.83                      |
| MET reconstruction        | 0.26                  | 0.17                    | 0.21                      |

Table 5.21: Impact of experimental uncertainties for the  $W^\pm W^\pm jj$  EWK processes in all channels.

| $WZ$                      | $e^\pm e^\pm$ % Yield | $\mu^\pm e^\pm$ % Yield | $\mu^\pm \mu^\pm$ % Yield |
|---------------------------|-----------------------|-------------------------|---------------------------|
| Jet-related Uncertainties | 9.58                  | 5.03                    | 8.45                      |
| $b$ -tagging efficiency   | 2.49                  | 2.23                    | 2.40                      |
| Pile-up                   | 2.99                  | 3.49                    | 3.33                      |
| Trigger efficiency        | 0.03                  | 0.09                    | 0.43                      |
| Lepton reconstruction/ID  | 1.52                  | 1.24                    | 3.07                      |
| MET reconstruction        | 0.93                  | 0.79                    | 1.63                      |

Table 5.22: Impact of experimental uncertainties for the  $WZ$  process in all channels.

---

1751    **5.5.2 Theoretical uncertainties**

1752    It is also necessary to consider uncertainties on the theoretical predictions in the fiducial region. They  
 1753    include the choice of PDF set, the value of the strong coupling constant  $\alpha_s$ , the renormalization  
 1754    scale  $\mu_R$ , the factorization scale  $\mu_F$ , and the parton showering. The size of these uncertainties are  
 1755    measured by generating new samples with variations in a chosen parameters and comparing them  
 1756    to samples using the nominal choice of the parameter. Internal variations on the PDF sets or using  
 1757    a different set entirely results in a relative uncertainty of up to 2.25% on the nominal sample. The  
 1758    impact from varying  $\alpha_s$  is very small, on the order of < 0.01%. The factorization and renormalization  
 1759    scales are independently varied between 0.5-2.0 from their nominal values of 1.0. This results in  
 1760    relative uncertainties on the prediction of up to 15%. Finally, varying the parameters in the parton  
 1761    showering results in up to 8% uncertainty.

1762    **5.5.2.1 Uncertainties from EWK-QCD interference**

1763    As mentioned in Section 5.0.2,  $W^\pm W^\pm jj$  production consists of both EWK processes. The two  
 1764    production modes cannot be naively separated due to cross terms in the matrix element calculation.  
 1765    These cross terms are referred to as *interference* terms. Since the  $W^\pm W^\pm jj$  EWK production is  
 1766    the focus of the analysis, and the signal region is designed to preferentially select those events, it is  
 1767    important to measure the size of the EWK-QCD interference contributions.

1768       The interference effects are estimated using the `MadGraph` MC generator, as it has a feature that  
 1769       allows direct modelling of the interference term. This allows four samples to be generated:

- 1770        1. Inclusive: All available diagrams are used in the matrix element calculation
- 1771        2. EWK only: Only EWK diagrams ( $\mathcal{O}(\alpha_{\text{EWK}}) = 4$ ) are used
- 1772        3. QCD only: Only QCD diagrams ( $\mathcal{O}(\alpha_s) = 2 \otimes \mathcal{O}(\alpha_{\text{EWK}}) = 2$ ) are used
- 1773        4. Interference: Only the interference terms are used

1774       A minimal set of generator level cuts, listed in Table 5.23, is applied in order to avoid biasing the  
 1775       sample towards either production mode. The cross sections for each of the four channels can be  
 1776       found in Table 5.24. The size of the interference is found to be approximately 6% of the total cross  
 1777       section and is taken as a systematic uncertainty.

| Generator level cuts   |
|------------------------|
| $\Delta\eta_{jj} < 10$ |
| Jet $p_T > 20$ GeV     |
| $M_{jj} > 10$ GeV      |

Table 5.23: The set of generator level cuts used for generating the interference samples with `MadGraph`.

| Sample       | $\sigma$ (fb)      |
|--------------|--------------------|
| Inclusive    | $3.646 \pm 0.0012$ |
| EWK only     | $2.132 \pm 0.0005$ |
| QCD only     | $1.371 \pm 0.0008$ |
| Interference | $0.227 \pm 0.0002$ |

Table 5.24: Cross sections for each different  $W^\pm W^\pm jj$  production mode (inclusive, EWK only, QCD only, and interference only) generated using `MadGraph`. The cross sections are calculated using a minimal set of generator level cuts from events where the  $W$  decays to a muon.

## 1778 5.6 Results

1779 After running the full analysis chain, the event yields in the signal region, low- $m_{jj}$  control region,  
 1780 and  $WZ$  control region as well as associated nuisance parameters representing the uncertainties are  
 1781 passed to the maximum likelihood fit. From this fit, the normalization factor for the  $WZ$  control  
 1782 region  $\mu_{WZ}$  and the signal strength parameter in the signal region  $\mu_{\text{obs}}$  are determined, and the  
 1783 predicted yields in each input bin have been shifted according to the process detailed in Section 5.4.1.

1784 The  $WZ$  normalization factor is measured to be:

$$\mu_{WZ} = 0.88^{+0.07}_{-0.07}(\text{stat})^{+0.31}_{-0.21}(\text{theory})^{+0.22}_{-0.11}(\text{sys}) \quad (5.27)$$

1785 and is constrained primarily by the number of data events in the  $WZ$  control region. The observed  
 1786 signal strength of  $W^\pm W^\pm jj$  EWK production, defined in Equation 5.21, is extracted from the fit  
 1787 and measured with respect to the prediction of the **SHERPA v2.2.2** MC generator:

$$\mu_{\text{obs}} = 1.45^{+0.25}_{-0.24}(\text{stat})^{+0.06}_{-0.08}(\text{theory})^{+0.27}_{-0.22}(\text{sys}) \quad (5.28)$$

1788 This corresponds to a rejection of the background-only hypothesis with a significance of  $6.9\sigma$ .

1789 The observed number of data events are compared to the predicted signal and background yields  
 1790 in the signal region in Table 5.25 before applying the fit and in Table 5.26 after the fit. The  $m_{jj}$   
 1791 distributions for data and prediction are shown in Figure 5.28 after the fit, and the fitted event  
 1792 yields in the low- $m_{jj}$  and  $WZ$  control regions are shown in Figure 5.29. Additional distributions  
 1793 can be found in Appendix A.

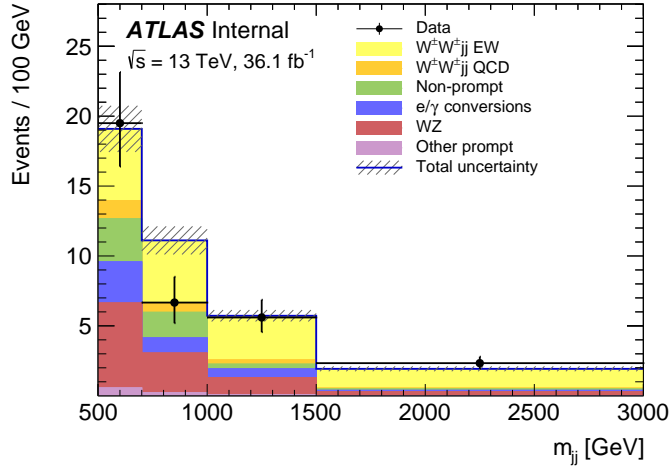


Figure 5.28: The dijet invariant mass  $m_{jj}$  distributions for data and predicted signal and background in the signal region after the fit. The shaded band represents the statistical and systematic uncertainties added in quadrature. Note that the bins have been scaled such that they represent the number of events per 100 GeV in  $m_{jj}$ . The background estimations from the fake factor are included in the “Non-prompt” category, and backgrounds from  $V\gamma$  production and electron charge misidentification are combined in the “ $e/\gamma$  conversions” category. Finally,  $ZZ$ ,  $VVV$ , and  $t\bar{t}V$  backgrounds are combined in the “Other prompt” category.

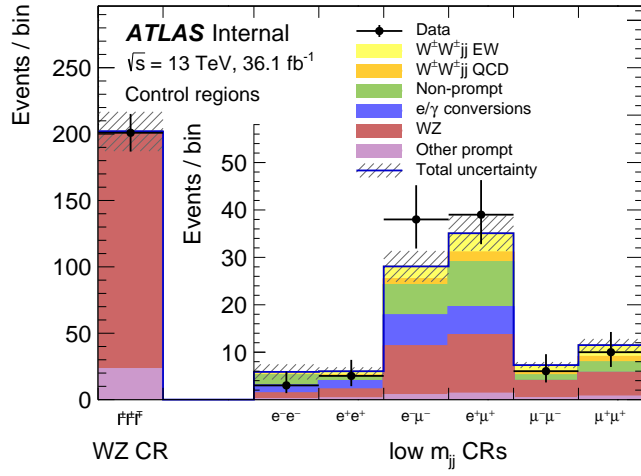


Figure 5.29: The event yields for data and predicted signal and background in the  $WZ$  and low- $m_{jj}$  control regions after the fit. The shaded band represents the statistical and systematic uncertainties added in quadrature. The background estimations from the fake factor are included in the “Non-prompt” category, and backgrounds from  $V\gamma$  production and electron charge misidentification are combined in the “ $e/\gamma$  conversions” category. Finally,  $ZZ$ ,  $VVV$ , and  $t\bar{t}V$  backgrounds are combined in the “Other prompt” category.

|                        | $e^+e^+$        | $e^-e^-$        | $\mu^+e^+$      | $\mu^-e^-$      | $\mu^+\mu^+$    | $\mu^-\mu^-$    | combined       |
|------------------------|-----------------|-----------------|-----------------|-----------------|-----------------|-----------------|----------------|
| $WZ$                   | $1.9 \pm 0.6$   | $1.3 \pm 0.4$   | $14 \pm 4$      | $8.9 \pm 2.6$   | $5.5 \pm 1.6$   | $3.6 \pm 1.1$   | $35 \pm 10$    |
| Non-prompt             | $4.1 \pm 2.3$   | $2.3 \pm 1.7$   | $9 \pm 5$       | $6 \pm 4$       | $0.57 \pm 0.15$ | $0.67 \pm 0.25$ | $23 \pm 10$    |
| $e/\gamma$ conversions | $1.74 \pm 0.29$ | $1.8 \pm 0.4$   | $6.1 \pm 1.6$   | $3.7 \pm 0.8$   | —               | —               | $13.4 \pm 2.5$ |
| Other prompt           | $0.17 \pm 0.05$ | $0.14 \pm 0.04$ | $0.90 \pm 0.19$ | $0.60 \pm 0.14$ | $0.36 \pm 0.10$ | $0.19 \pm 0.05$ | $2.4 \pm 0.5$  |
| $W^\pm W^\pm jj$ QCD   | $0.38 \pm 0.13$ | $0.16 \pm 0.05$ | $3.0 \pm 1.0$   | $1.2 \pm 0.4$   | $1.8 \pm 0.6$   | $0.76 \pm 0.25$ | $7.3 \pm 2.5$  |
| Expected background    | $8.2 \pm 2.4$   | $5.7 \pm 1.8$   | $33 \pm 7$      | $21 \pm 5$      | $8.2 \pm 1.8$   | $5.3 \pm 1.2$   | $81 \pm 14$    |
| $W^\pm W^\pm jj$ EWK   | $3.8 \pm 0.6$   | $1.49 \pm 0.22$ | $16.5 \pm 2.5$  | $6.5 \pm 1.0$   | $9.1 \pm 1.4$   | $3.5 \pm 0.5$   | $41 \pm 6$     |
| Data                   | 10              | 4               | 44              | 28              | 25              | 11              | 122            |

Table 5.25: Table of the data and prediction event yields in the signal region before the fit. Numbers are shown for the six lepton flavor and charge channels and for all channels combined. Here the  $WZ$  background yields are normalized to the data in the  $WZ$  control region. The background estimations from the fake factor are included in the “Non-prompt” category, and backgrounds from  $V\gamma$  production and electron charge misidentification are combined in the “ $e/\gamma$  conversions” category. Finally,  $ZZ$ ,  $VVV$ , and  $t\bar{t}V$  backgrounds are combined in the “Other prompt” category.

|                        | $e^+e^+$        | $e^-e^-$        | $\mu^+e^+$      | $\mu^-e^-$      | $\mu^+\mu^+$    | $\mu^-\mu^-$    | combined       |
|------------------------|-----------------|-----------------|-----------------|-----------------|-----------------|-----------------|----------------|
| $WZ$                   | $1.49 \pm 0.30$ | $1.10 \pm 0.26$ | $11.7 \pm 1.7$  | $8.0 \pm 1.3$   | $5.0 \pm 0.6$   | $3.5 \pm 0.6$   | $31 \pm 4$     |
| Non-prompt             | $2.2 \pm 1.3$   | $1.2 \pm 0.7$   | $5.7 \pm 2.8$   | $4.5 \pm 1.8$   | $0.57 \pm 0.06$ | $0.65 \pm 0.14$ | $15 \pm 6$     |
| $e/\gamma$ conversions | $1.6 \pm 0.4$   | $1.6 \pm 0.5$   | $6.3 \pm 1.6$   | $4.3 \pm 1.1$   | —               | —               | $13.8 \pm 2.9$ |
| Other prompt           | $0.16 \pm 0.04$ | $0.14 \pm 0.04$ | $0.90 \pm 0.19$ | $0.63 \pm 0.13$ | $0.39 \pm 0.09$ | $0.22 \pm 0.05$ | $2.4 \pm 0.5$  |
| $W^\pm W^\pm jj$ QCD   | $0.35 \pm 0.13$ | $0.15 \pm 0.05$ | $2.9 \pm 1.0$   | $1.2 \pm 0.4$   | $1.8 \pm 0.6$   | $0.76 \pm 0.25$ | $7.2 \pm 2.4$  |
| Expected background    | $5.8 \pm 1.5$   | $4.1 \pm 1.1$   | $27 \pm 4$      | $18.7 \pm 2.6$  | $7.7 \pm 0.8$   | $5.1 \pm 0.6$   | $69 \pm 7$     |
| $W^\pm W^\pm jj$ EWK   | $5.6 \pm 1.0$   | $2.2 \pm 0.4$   | $24 \pm 5$      | $9.4 \pm 1.8$   | $13.5 \pm 2.5$  | $5.2 \pm 1.0$   | $60 \pm 11$    |
| Data                   | 10              | 4               | 44              | 28              | 25              | 11              | 122            |

Table 5.26: Table of the data and prediction event yields in the signal region after the fit. Numbers are shown for the six lepton flavor and charge channels and for all channels combined. The background estimations from the fake factor are included in the “Non-prompt” category, and backgrounds from  $V\gamma$  production and electron charge misidentification are combined in the “ $e/\gamma$  conversions” category. Finally,  $ZZ$ ,  $VVV$ , and  $t\bar{t}V$  backgrounds are combined in the “Other prompt” category.

1794     The last ingredient necessary to measure the  $W^\pm W^\pm jj$  EWK cross section is the theory predicted  
 1795     cross section in the fiducial region defined in Table 5.18. SHERPA v2.2.2 is used for the calculation,  
 1796     and the cross section in the total generator phase space is  $40.81 \pm 0.05$  fb, and the fiducial cross section  
 1797     is  $2.01 \pm 0.02$  fb. This corresponds to an acceptance factor of  $\mathcal{A} = 0.0493 \pm 0.0002$ . Uncertainties on  
 1798     the simulation are estimated using variations of the scale, parton shower, and PDF set. The final  
 1799     prediction used in the cross section measurement including uncertainties from Section 5.5.2 is:

$$\sigma_{\text{SHERPA}}^{\text{fid}} = 2.01 \pm 0.02(\text{stat}) \quad {}^{+0.29}_{-0.23}(\text{scale}) \quad {}^{+0.16}_{-0.02}(\text{parton shower}) \quad {}^{+0.05}_{-0.03}(\text{PDF}) \text{ fb} \quad (5.29)$$

1800     Combining this SHERPA prediction with the measured signal strength  $\mu_{\text{obs}}$  from Equation 5.28,  
 1801     the measured fiducial cross section  $\sigma_{\text{meas}}^{\text{fid}}$  can be calculated using Equation 5.25:

$$\sigma_{\text{meas}}^{\text{fid}} = 2.91 \pm 0.51(\text{stat}) \quad {}^{+0.12}_{-0.16}(\text{theory}) \quad {}^{+0.24}_{-0.23}(\text{sys}) \quad {}^{+0.08}_{-0.06}(\text{luminosity}) \text{ fb} \quad (5.30)$$

1802 A plot comparing the measured fiducial cross section to two theoretical calculations is shown in  
 1803 Figure 5.30. The measured value is compared to the **SHERPA v2.2.2** prediction used to calculate  
 1804  $\mu_{\text{obs}}$  as well as to **POWHEG-BOX v2**. As mentioned in Section 5.1.1, this **POWHEG** sample does not  
 1805 include the resonant triboson diagrams and is only used here for a visual comparison.

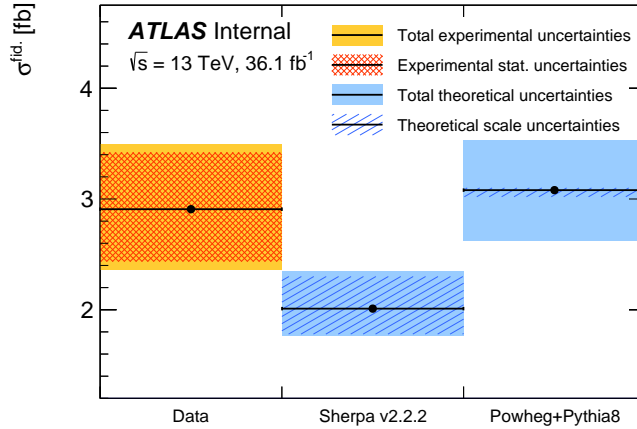


Figure 5.30: Comparison of the measured  $W^\pm W^\pm jj$  EWK fiducial cross section with theoretical calculations from **SHERPA v2.2.2** and **POWHEG-BOX v2**. The light orange band represents the total experimental uncertainty on the measured value, and the dark orange hashed band is the statistical uncertainty. For the simulations, the light blue band represents the total theoretical uncertainty, and the dark blue hashed band are the scale uncertainties. The theory predictions do not include the interference between the EWK and QCD production.

1806

## CHAPTER 6

1807

# Prospects for same-sign $WW$ at the High 1808 Luminosity LHC

1809 On December 3, 2018, Run 2 of the LHC officially ended, and the collider was shut down to begin  
1810 the first of two scheduled extended maintenance periods [81]. During these two long shutdowns,  
1811 the Phase-I and Phase-II upgrades of the LHC and ATLAS will occur in order to prepare for the  
1812 High-Luminosity LHC (HL-LHC) which is scheduled to begin operation in 2026 [82].

1813 The HL-LHC is planned to run at a center-of-mass energy of  $\sqrt{s} = 14$  TeV with an instantaneous  
1814 luminosity of  $\mathcal{L} = 5 \times 10^{34}$  cm $^{-2}$ s $^{-1}$  with up to 200 collisions per beam-crossing. Over the course  
1815 of operation, the HL-LHC is expected to collect a total integrated luminosity of  $\mathcal{L} = 3000$  fb $^{-1}$  by  
1816 2035 [83].

1817 These run conditions will be much harsher than what ATLAS has experienced so far, and there  
1818 are several upgrades planned for the detector to operate in the high luminosity environment. Most  
1819 notably, the entire ID will be replaced with an all-silicon tracker which will extend the coverage from  
1820  $|\eta| \leq 2.7$  up to  $|\eta| \leq 4.0$ . This will allow for reconstruction of charged particle tracks which can  
1821 in turn be matched to clusters in the calorimeters for electron identification or forward jet tagging  
1822 [84].

1823 The upgraded detector, the higher beam energy, and the increased volume of data to be collected  
1824 provides the opportunity to measure rarer processes with a much higher precision than what was  
1825 possible in Run 1. Same-sign  $W^\pm W^\pm jj$  production, is one such process. With greater statistics,  
1826 the accuracy of the cross section measurement can be improved over the 13 TeV analysis detailed in  
1827 Chapter 5, and it also will allow for more detailed physics studies, such as measuring the polarization  
1828 of the  $W$  bosons. A measurement of the longitudinal polarization of the scattered  $W$  bosons has

not yet been possible, but it remains of great interest due to its sensitivity to electroweak symmetry breaking [85]. The analysis detailed in this chapter is based off of the 2018 ATLAS HL-LHC  $W^\pm W^\pm jj$  prospects study [86] which extends upon the results of the previous year’s study [87].

### 6.0.1 Analysis Overview

The experimental signature of interest is identical to the 13 TeV analysis: two prompt leptons (either electrons or muons) with the same charge, missing transverse energy, and two high energy, forward jets. These jets are again required to have a large angular separation and a high combined invariant mass to preferentially select EWK- over QCD-produced  $W^\pm W^\pm jj$  events.

Background processes are again similar to the 13 TeV analysis and are summarized again here. The dominant source of prompt background from  $WZ + \text{jets}$  events where both bosons decay leptonically. If the lepton from the  $Z$ -decay with opposite charge from the  $W$  falls outside of the detector acceptance or is not identified, the remainder could appear to be a  $W^\pm W^\pm jj$  signal event. To a lesser extent,  $ZZ + \text{jets}$  events can enter the signal region in much the same way provided two leptons are “lost”. Other prompt sources include  $t\bar{t} + V$  and multiple parton interactions, however these processes do not contribute much. These prompt backgrounds are expected to contribute less than in Run 2 with the addition of forward tracking in the upgraded ATLAS detector. Jets mis-reconstructed as leptons or leptons from hadronic decays (such as  $t\bar{t}$  and  $W + \text{jets}$  production) comprise the non-prompt lepton background. Lastly, events with two prompt, opposite-charge electrons can appear as a same-sign event provided one of the electrons is mis-reconstructed as the wrong charge.

In this analysis, the EWK production of  $W^\pm W^\pm jj$  is studied in the context of the planned HL-LHC run conditions and upgraded ATLAS detector. An optimized event selection (referred to as the *optimized selection*) is also explored in an effort to gain increased signal significance over the *default selection*. The cross section of the inclusive EWK production is measured for both the default and optimized selections, and the extraction of the longitudinal scattering significance is measured with the optimized selection.

## 6.1 Theoretical motivation

The theoretical motivation for studying the ssWW process—and VBS in general—is detailed in Section 5.0.2. Since it is specifically the scattering of *longitudinally polarized* vector bosons that

1858 violates unitarity without a SM Higgs boson, a direct measurement of this cross section will be very  
 1859 useful for understanding how the Higgs unitarizes the process [85].

### 1860 6.1.1 Experimental sensitivity to longitudinal polarization

1861 **TODO:** mention that since there are so many polarization possibilities, a large integrated luminosity  
 1862 is needed to measure just one of them individually **TODO:** Paragraph about polarization vector and  
 1863 what it means physically There are three possible polarization states for a massive vector boson:  
 1864 two transverse (+ or -) and one longitudinal (0). Therefore, in a system with two  $W$  bosons, the  
 1865 overall polarization can be purely longitudinal (00), purely transverse (++, --, and +−), or mixed  
 1866 (+0 and −0). The three combinations will be referred to as *LL*, *TT*, and *LT* respectively.

1867 In order extract the longitudinal scattering component, it is necessary to find variables that can  
 1868 help distinguish the LL from the TT and LT events. Several were studied, and those with the best  
 1869 discriminating power between the polarizations are the leading and subleading lepton  $p_T$  as well as  
 1870 the azimuthal separation ( $|\Delta\phi_{jj}|$ ) of the two VBS jets. Both leptons in LL events tend to be softer  
 1871 than the TT and LT events (see Figure 6.1), which motivates keeping cuts on these quantities as  
 1872 low as possible in the event selection. In the case of  $|\Delta\phi_{jj}|$ , the LL events generally had a larger  
 1873 dijet separation (see Figure 6.2), and this variable is used in a binned likelihood fit to extract the  
 1874 longitudinal scattering significance.

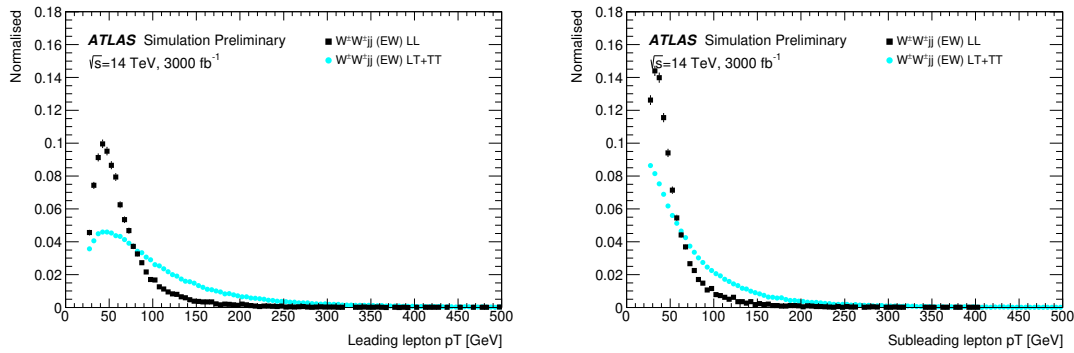


Figure 6.1: Comparison of the leading (left) and subleading (right) lepton  $p_T$  distributions for purely longitudinal (LL, black) and mixed polarization (LT+TT, cyan)  $W^\pm W^\pm jj$  events.

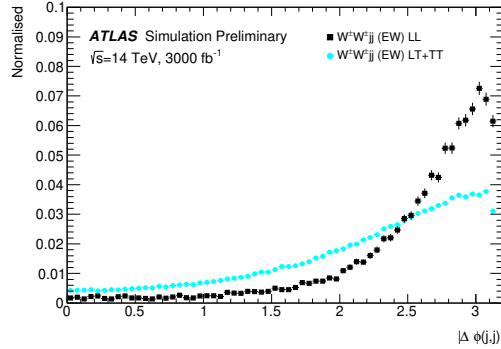


Figure 6.2: Comparison of the azimuthal dijet separation ( $|\Delta\phi_{jj}|$ ) for purely longitudinal (LL, black) and mixed polarization (LT+TT, cyan)  $W^\pm W^\pm jj$  events.

## 6.2 Monte Carlo samples

As no real HL-LHC data will be available for many years, all signal and background processes are modeled using MC simulations generated at  $\sqrt{s} = 14$  TeV, with the event yields scaled to the anticipated HL-LHC integrated luminosity of  $\mathcal{L} = 3000 \text{ fb}^{-1}$ . The MC samples used in the analysis are generated at particle-level and have not been run through the typical full simulation of the ATLAS detector. Instead, smearing functions derived from a **GEANT4** simulation of the upgraded ATLAS detector are used to estimate detector effects such as momentum resolution. In addition, pileup events are fully simulated. The MC samples used in this analysis are summarized in Table 6.1.

The signal sample consists of both VBS and non-VBS electroweak (EWK)  $W^\pm W^\pm jj$  production, and it is simulated with the **Madgraph5\_aMC@NLO** generator using the **NNPDF3.0** PDF set and interfaced with **PYTHIA v8** [88] for hadronization and parton showering. To study the longitudinal polarization more directly, two additional **Madgraph5\_aMC@NLO**  $W^\pm W^\pm jj$  samples are used: one containing only the longitudinal contribution (LL) and a second containing the transverse (TT) and mixed (LT) contributions.

There are many other processes that can produce the same final state as the  $W^\pm W^\pm jj$  and must also be accounted for using MC simulations.  $WZ$  events are generated using **SHERPA v2.2.0**, which includes up to one parton at NLO in the strong coupling constant and up to three additional partons at LO. Both EWK and QCD production are included in these samples.  $ZZ$  and triboson  $VVV$  ( $V = W, Z$ ) events are generated using **SHERPA v2.2.2** with up to two additional partons in the final state. For the triboson backgrounds, the bosons can decay leptonically or hadronically.  $W+jets$  backgrounds are generated for electron, muon, and tau final states at LO

| Process                  | Generator         | Comments                                 |
|--------------------------|-------------------|--|
| $W^\pm W^\pm jj$ (EWK)   | Madgraph5_aMC@NLO | Signal sample                            |
| $W^\pm W^\pm jj$ (QCD)   | Madgraph5_aMC@NLO |  |
| $W^\pm W^\pm jj$ (LL)    | Madgraph5_aMC@NLO | Pure longitudinal polarization sample    |
| $W^\pm W^\pm jj$ (TT+LT) | Madgraph5_aMC@NLO | Mixed and transverse polarization sample |
| Diboson                  | SHERPA v2.2.0     | $WZ$ events                              |
|                          | SHERPA v2.2.2     | $ZZ$ events                              |
| Triboson                 | SHERPA v2.2.2     |  |
| $W+jets$                 | Madgraph5_aMC@NLO |  |
| $Z+jets$                 | POWHEG-BOX v2     |  |
| $t\bar{t}$               | POWHEG-BOX        |  |
| Single top               | POWHEG-BOS        |  |

Table 6.1: Summary of MC samples used in the analysis.

1896 with Madgraph5\_aMC@NLO and the NNPDF3.0 set with showering from PYTHIA v8.  $Z+jets$  events are  
 1897 produced using POWHEG-BOX v2 and the CT10 PDF set interfaced with PYTHIA v8. Finally,  $t\bar{t}$  and  
 1898 single-top events are generated using POWHEG-BOX with showering from PYTHIA v6.

### 1899 6.3 Background estimations

1900 In this analysis, all background contributions are estimated using MC simulations. Backgrounds such  
 1901 as electron charge misidentification and fake electrons from jets (which are traditionally estimated  
 1902 using data-driven techniques) are estimated using a set of parameterization functions applied to the  
 1903 MC. These functions calculate the probability that an electron is assigned the wrong charge or a  
 1904 jet is mis-reconstructed as an electron parameterized by the  $p_T$  and  $\eta$  of the electron or jet. The  
 1905 probabilities are derived from studies on expected electron performance with the upgraded ATLAS  
 1906 detector [89].

1907 Processes involving two  $W$  and  $Z$  bosons are grouped together as *diboson* backgrounds, with the  
 1908 exception of  $W^\pm W^\pm jj$  events produced via QCD interactions, which are kept separate. Similarly,  
 1909 all backgrounds with three vector bosons are combined and labeled as *triboson*. Any  $W+jets$  or top  
 1910 events that pass selection and do not contain a fake electron, as well as any  $Z+jets$  events without an  
 1911 electron identified as having its charge misidentified are combined as *other non-prompt* backgrounds.

#### 1912 6.3.1 Truth-based isolation

1913 To properly calculate particle isolation, it requires information from several detector subsystems  
 1914 including tracking and calorimeter responses. Since the MC samples used in this analysis have not

been run through a full detector simulation, it is not possible to construct the canonical isolation variables used in analyses. At truth-level, this is generally not a serious concern as  $p_T$  signal leptons tend to be well isolated to begin with. However, isolation is one of the most powerful tools for rejecting leptons from non-prompt sources such as top events, which are produced in association with additional nearby particles from  $b$  and  $c$  quark decays. In this analysis, with the absence of any sort of isolation requirement, contributions from top backgrounds (including single top,  $t\bar{t}$  and  $t\bar{t} + V$ ) are more than an order of magnitude higher than expected.

As a result, it is necessary to find one or more quantities that are comparable to the isolation information that is available in fully-simulated samples. Analogues to track- and calorimeter-based isolation variables are constructed by summing the momentum and energy, respectively, of stable truth particles with  $p_T > 1$  GeV within a specified radius of each signal lepton. For the track-based isolation, only charged truth particles are used; both charged and neutral particles (excluding neutrinos) are included for the calorimeter-based isolation. Ultimately, a set of isolation cuts are chosen that are similar to those recommended by ATLAS for Run 2 analyses. The truth-based isolation requirements are listed in Table 6.2.

|   | Electron Isolation      | Muon Isolation            |
|---|-------------------------|---------------------------|
| Track-based isolation cone size         | $\Delta R < 0.2$        | $\Delta R < 0.3$          |
| Track-based isolation requirement       | $\sum p_T/p_T^e < 0.06$ | $\sum p_T/p_T^\mu < 0.04$ |
| Calorimeter-based isolation cone size   | $\Delta R < 0.2$        | $\Delta R < 0.2$          |
| Calorimeter-based isolation requirement | $\sum E_T/p_T^e < 0.06$ | $\sum E_T/p_T^\mu < 0.15$ |

Table 6.2: Truth-based isolation requirements for electrons and muons.

The truth-based isolation requirement reduces the top background by over 99%, and the percentage of the total background consisting of top events is reduced from 83% to 2%. Additional details on the truth-based isolation studies are presented in Appendix B.1.

## 6.4 Object and event selection

### 6.4.1 Object selection

Electrons and muons are preselected to have  $p_T > 7$  and 6 GeV, respectively, and  $|\eta| \leq 4.0$ . The likelihood of a given lepton to pass the trigger and identification requirements is estimated by calculating an efficiency dependent on the  $p_T$  and  $\eta$  of the lepton. The leptons are also required to pass the isolation criteria detailed in Table 6.2. Jets that have been tagged as a fake electron by the functions described in Section 6.3 are treated as electrons for the purpose of the object selection and

1940 are subject to the same criteria. In order to be considered a signal lepton, an additional requirement  
 1941 of  $p_T > 25$  GeV is applied on top of the preselection. The two highest  $p_T$  leptons passing this  
 1942 selection are chosen to be the leading and subleading signal leptons.

1943 Jets are clustered using the anti- $k_t$  algorithm [72] from final-state particles within a radius of  
 1944  $\Delta R = 0.4$  (excluding muons and neutrinos). Jets are required to have  $p_T > 30$  GeV and lie within  
 1945  $|\eta| < 4.5$ , with an additional cut of  $p_T > 70$  GeV for jets above  $|\eta| \geq 3.8$  in order to suppress jets  
 1946 from pileup interactions. Jets overlapping with a preselected electron within  $\Delta R(e, j) < 0.05$  are  
 1947 removed in order to prevent double counting. The two highest  $p_T$  jets are defined as the leading  
 1948 and subleading *tag jets*.

1949 **6.4.2 Event selection**

1950 The default event selection is summarized in Table 6.3 and described here. Exactly two signal  
 1951 leptons are required with the same electric charge and separated from each other by  $\Delta R(l l) > 0.3$ .  
 1952 In order to suppress contributions from Drell-Yan backgrounds, the two signal leptons must have  
 1953 an invariant mass  $m_{ll}$  greater than 20 GeV. Additionally, if both signal leptons are electrons, their  
 1954 mass must be at least 10 GeV from the  $Z$ -boson mass in order to reduce background from  $Z$ -boson  
 1955 decays<sup>18</sup>. The event is required to have at least 40 GeV of missing transverse energy ( $E_T^{\text{miss}}$ ) to  
 1956 account for the two neutrinos from the  $W$  decays. Events with additional preselected leptons are  
 1957 vetoed, which greatly reduces  $WZ$  and  $ZZ$  backgrounds.

1958 Each event must have at least two jets, and both tag jets are required to not overlap with the  
 1959 signal leptons, and there is a veto on events with one or more  $b$ -jets. In order to preferentially select  
 1960 EWK production, the tag jets are also required to have a large separation between them and a large  
 1961 invariant mass. Finally, a cut on the lepton centrality<sup>19</sup>,  $\zeta$ , defined in Equation 6.1 enhances the  
 1962 EWK  $W^\pm W^\pm jj$  signal.

$$\zeta = \min[\min(\eta_{\ell 1}, \eta_{\ell 2}) - \min(\eta_{j 1}, \eta_{j 2}), \max(\eta_{j 1}, \eta_{j 2}) - \max(\eta_{\ell 1}, \eta_{\ell 2})] \quad (6.1)$$

---

<sup>18</sup>The electron charge misidentification rate in the upgraded ATLAS detector is estimated to be high enough that contributions from  $Z \rightarrow ee$  backgrounds are non-negligible.

<sup>19</sup> $\zeta$  is a measurement of whether the two signal leptons lie between the two tagging jets in  $\eta$ , as is preferred by the VBS topology.

| Selection requirement | Selection value   |
|-----------------------|---|
| Lepton kinematics     | $p_T > 25 \text{ GeV}$<br>$ \eta  \leq 4.0$   |
| Jet kinematics        | $p_T > 30 \text{ GeV}$ for $ \eta  \leq 4.5$<br>$p_T > 70 \text{ GeV}$ for $ \eta  > 3.8$ |
| Dilepton charge       | Exactly two signal leptons with same charge   |
| Dilepton separation   | $\Delta R_{l,l} \geq 0.3$   |
| Dilepton mass         | $m_{ll} > 20 \text{ GeV}$   |
| $Z$ boson veto        | $ m_{ee} - m_Z  > 10 \text{ GeV}$ ( $ee$ -channel only)                                   |
| $E_T^{\text{miss}}$   | $E_T^{\text{miss}} > 40 \text{ GeV}$  |
| Jet selection         | At least two jets with $\Delta R_{l,j} > 0.3$   |
| $b$ jet veto          | $N_{\text{b-jet}} = 0$  |
| Dijet separation      | $\Delta \eta_{jj} > 2.5$  |
| Trilepton veto        | No additional preselected leptons   |
| Dijet mass            | $m_{jj} > 500 \text{ GeV}$  |
| Lepton-jet centrality | $\zeta > 0$   |

Table 6.3: Summary of the signal event selection.

## 1963 6.5 Selection optimization

1964 An upgraded detector along with an increase in center of mass energy and integrated luminosity  
 1965 provides an opportunity to study whether the event selection can be optimized to improve the signal  
 1966 to background ratio.

### 1967 6.5.1 Random grid search algorithm

1968 The chosen method for optimizing the event selection is a cut-based algorithm known as the Random  
 1969 Grid Search (RGS) [90]. Consider a simple case of two variables  $x$  and  $y$  chosen to differentiate signal  
 1970 from background. In order to be considered a signal event, a given event would be required to pass  
 1971 a set of selection criteria, called a *cut point*:  $c = \{x > x_c, y > y_c\}$ . A simple method to choose the  
 1972 optimal cut point (i.e. the “best” values of the cuts  $x_c$  and  $y_c$ ) would be to construct an  $n \times m$   
 1973 rectangular grid in  $x$  and  $y$  consisting of points  $(x_0, y_0), (x_1, y_1), \dots, (x_n, y_m)$ , as in the left plot of  
 1974 Figure 6.3. One can then choose a cut point  $c_k = \{x > x_i, y > y_j\}$  that maximizes the signal  
 1975 significance as measured by a chosen metric. This would be considered a *rectangular grid search*.

1976 While effective in principle, a rectangular grid search comes with two major drawbacks:

- 1977 1. The algorithm scales exponentially as the number of variables to be optimized increases, as  
 1978 this is effectively increasing the dimensionality of the grid. In the simple case of a square grid  
 1979 with  $N$  bins per variable  $v$ , the number of cut points to be evaluated grows as  $N^v$ .

1980     2. Signal and background samples are rarely evenly distributed over the entire grid, resulting  
 1981       in many cut points being sub-optimal and evaluating them would be a waste of computing  
 1982       resources.

1983     To combat these limitations, the RGS algorithm constructs a grid of cut points directly from  
 1984       the signal sample itself. In the two-dimensional example, this means that the variables  $x_i$  and  $y_j$   
 1985       making up the cut point  $c_k = \{x > x_i, y > y_j\}$  take their values directly from a given signal event.  
 1986     This has the benefit of creating a *random grid* of cut points that is biased towards regions of high  
 1987       signal concentration by construction. This reduces the need for exponentially increasing numbers of  
 1988       cut points while ensuring that computing resources are not wasted in regions with few to no signal  
 1989       events. An example of a two-dimensional random grid is shown in the right-hand plot in Figure 6.3.

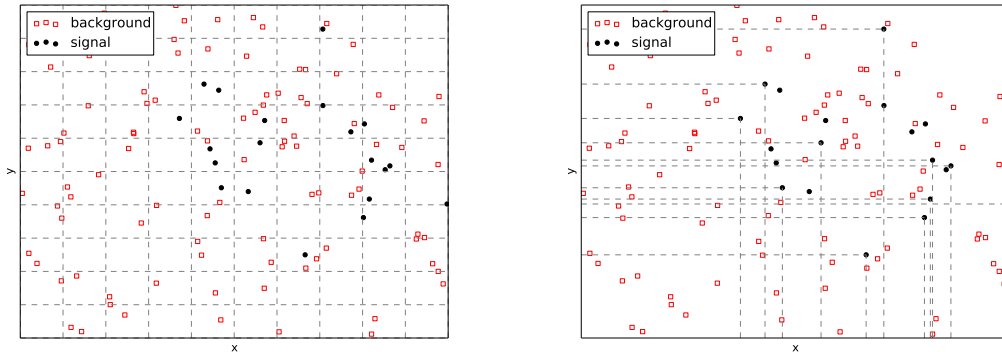


Figure 6.3: A visual representation of a two-dimensional rectangular grid (left) and a random grid (right) in variables  $x$  and  $y$ . The signal events are the black circles, and the red squares are the background events. Each intersection of gray dashed lines represents a cut point to be evaluated by the optimization.

1990     Once the random grid of cut points is constructed, the optimal cut point can be chosen using any  
 1991       number of metrics, such as signal to background ratio. For the purpose of the  $W^\pm W^\pm jj$  upgrade  
 1992       study, the optimal cut point is chosen to be the one that maximizes the signal significance  $Z$  as  
 1993       defined in Equation 6.2 [91].

$$Z = \sqrt{2 \left[ (s + b) \ln \left( \frac{s + b}{b_0} \right) + b_0 - s - b \right] + \frac{(b - b_0)^2}{\sigma_b^2}} \quad (6.2)$$

1994     where  $s$  and  $b$  are the number of signal and background events, respectively,  $\sigma_b$  is the total uncertainty  
 1995       on the background, and  $b_0$  is defined as:

$$b_0 = \frac{1}{2} \left( b - \sigma_b^2 + \sqrt{(b - \sigma_b^2)^2 + 4(s + b)\sigma_b^2} \right) \quad (6.3)$$

1996 In the case where the background is known precisely (i.e.  $\sigma_b = 0$ ), Equation 6.2 simplifies to

$$Z = \sqrt{2 \left( b[(1 + s/b) \ln(1 + s/b) - s/b] \right)} \quad (6.4)$$

1997 which further reduces to the familiar  $Z = s/\sqrt{b}$  for the case when  $s \ll b$ .

### 1998 6.5.2 Inputs to the optimization

1999 In order to train the RGS, signal and background samples are prepared from events passing the  
 2000 event selection outlined in Table 6.3 up through the  $b$ -jet veto. The signal sample is chosen to be  
 2001 the longitudinally polarized  $W^\pm W^\pm jj$  EWK events, and the transverse and mixed polarizations  
 2002 are treated as background along with  $W^\pm W^\pm jj$  events from QCD interactions and the traditional  
 2003 backgrounds listed in Section 6.3. Splitting the inclusive  $W^\pm W^\pm jj$  EWK events by polarization  
 2004 allows the optimization to favor the longitudinally polarized events as much as possible, even though  
 2005 they both contribute to the EWK signal.

2006 The following variables are chosen for optimization:

- 2007 • Leading lepton  $p_T$
- 2008 • Dilepton invariant mass ( $m_{ll}$ )
- 2009 • Leading and subleading jet  $p_T$
- 2010 • Dijet invariant mass ( $m_{jj}$ )
- 2011 • Lepton-jet centrality ( $\zeta$ )

2012 Subleading lepton  $p_T$  is omitted as it is desirable to keep the cut value as low as possible due to  
 2013 its sensitivity to the longitudinal polarization (as discussed in Section 6.1.1). Additionally, the dijet  
 2014 separation  $\Delta\eta_{jj}$  was included in the optimization originally, however it was dropped from the list due  
 2015 to the cut value being motivated by differences between EWK and QCD produced  $W^\pm W^\pm jj$  events.

2016 Two additional constraints were imposed when selecting the optimal cut point:

- 2017 1. At least 1000 signal events must survive in order to prevent the optimization from being too  
 2018 aggressive and unnecessarily reducing signal statistics.
- 2019 2. The dijet invariant mass may only vary within a 50 GeV range of the default value (from  
 2020 450 – 550 GeV) due to the cut being physically motivated by the VBS event topology (see  
 2021 Section 5.0.3).

2022     Lastly, the signal significance is calculated without taking into account the uncertainty of the  
 2023 background using Equation 6.4. This is due to the fact that the statistical uncertainties of the fake  
 2024 electron and charge misidentification backgrounds are quite large, owing to poor MC statistics in a  
 2025 few of the samples. If Equation 6.2 were used instead, the optimization will cut unreasonably hard  
 2026 against these backgrounds. Since Monte Carlo statistics is not expected to be a limiting factor when  
 2027 this analysis is performed at the HL-LHC, it is more realistic to simply ignore these large statistical  
 2028 uncertainties for the purpose of the optimization.

### 2029    6.5.3 Results of the optimization

2030    Ultimately, the random grid is constructed from over 38,000 LL-polarized  $W^\pm W^\pm jj$  events in the  
 2031 six variables listed above. After applying the constraints, the optimal cut point reduces the total  
 2032 background from 9900 to 2310 while reducing the signal from 3489 to 2958. This corresponds to  
 2033 an increase in signal significance from  $Z = 33.26$  to  $Z = 52.63$  as calculated by Equation 6.4. The  
 2034 updates to the event selection are listed in Table 6.4.

2035    The large reduction in the background is primarily a result of the increase in the leading and  
 2036 subleading jet  $p_T$  from 30 GeV to 90 GeV and 45 GeV, respectively. As can be seen in Figure 6.4,  
 2037 this increase removes a significant portion of the backgrounds from jets faking electrons and charge  
 2038 mis-ID. Additionally, the loosening of the lepton-jet centrality cut  $\zeta$  allows more signal events to  
 2039 survive the event selection (see Figure 6.5). Other changes to the event selection are minor and  
 2040 do not individually have a large impact on the signal or background yields; similar distributions of  
 2041 these variables are shown in Appendix B.2.

2042    The full event yields after optimization as well as the cross section measurement are detailed  
 2043 alongside those using the default selection in Section 6.6.

| Selection requirement | Selection value   |
|-----------------------|---|
| Lepton kinematics     | $p_T > 28$ GeV (leading lepton only)                            |
| Jet kinematics        | $p_T > 90$ GeV (leading jet)<br>$p_T > 45$ GeV (subleading jet) |
| Dilepton mass         | $m_{ll} > 28$ GeV   |
| Dijet mass            | $m_{jj} > 520$ GeV  |
| Lepton-jet centrality | $\zeta > -0.5$  |

Table 6.4: Updates to the  $W^\pm W^\pm jj$  event selection criteria after optimization. Cuts not listed remain unchanged from the default selection in Table 6.3.

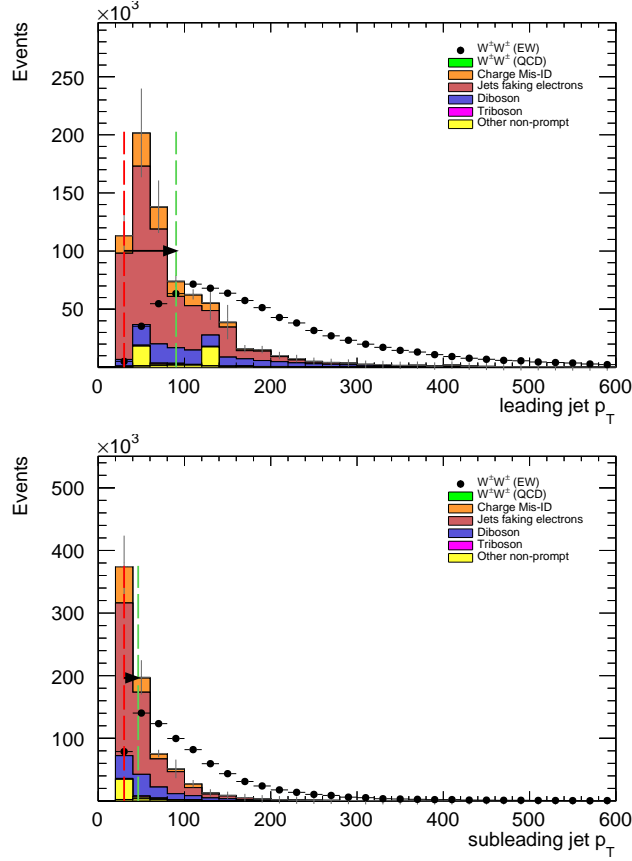


Figure 6.4: Leading (top) and subleading (bottom) jet  $p_T$  distributions. The default and optimized cuts are represented by the red and green dashed lines, respectively. The  $W^{\pm}W^{\pm}jj$  EWK signal (black points) is normalized to the same area as the sum of the backgrounds (colored histogram).

## 2044 6.6 Results

### 2045 6.6.1 Event yields

2046 After applying the full event selection, the analysis is broken down into four channels based off of  
 2047 the flavor of the signal leptons:  $\mu\mu$ ,  $ee$ ,  $\mu e$ , and  $e\mu$ . The full signal and background event yields are  
 2048 shown in Table 6.5 for each channel separately and combined using the default event selection. 3489  
 2049 EWK  $W^{\pm}W^{\pm}jj$  events are expected compared to 9900 background events. The dominant sources  
 2050 of background are jets faking electrons followed by charge misidentification and diboson processes.  
 2051 Triboson events, QCD  $W^{\pm}W^{\pm}jj$ , and other non-prompt sources make up approximately 5% of the  
 2052 total background combined.

2053 The event yields for the optimized selection detailed in Section 6.5.3 are listed in Table 6.6. After

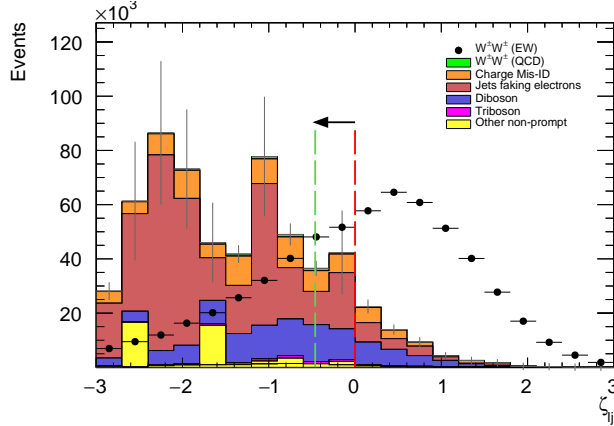


Figure 6.5: Lepton-jet centrality distribution. The default and optimized cuts are represented by the red and green dashed lines, respectively. The  $W^\pm W^\pm jj$  EWK signal (black points) is normalized to the same area as the sum of the backgrounds (colored histogram).

|                               | All channels | $\mu\mu$ | $ee$ | $\mu e$ | $e\mu$ |
|-------------------------------|--------------|----------|------|---------|--------|
| $W^\pm W^\pm jj$ (QCD)        | 206.4        | 91.1     | 22.8 | 38.4    | 54.1   |
| Charge Misidentification      | 2300         | 0.0      | 2100 | 90      | 160    |
| Jets faking electrons         | 5000         | 0.0      | 3400 | 1200    | 340    |
| $WZ + ZZ$                     | 2040         | 500      | 438  | 423     | 680    |
| Tribosons                     | 115          | 47       | 15.4 | 21.6    | 31.2   |
| Other non-prompt              | 210          | 110      | 20   | 60      | 27     |
| Total Background              | 9900         | 750      | 6000 | 1900    | 1290   |
| Signal $W^\pm W^\pm jj$ (EWK) | 3489         | 1435     | 432  | 679     | 944    |

Table 6.5: Signal and background event yields using the default event selection for an integrated luminosity of  $\mathcal{L} = 3000 \text{ fb}^{-1}$ . Events containing a fake or charge-flipped electron are removed from their respective sources and combined into a single entry each.

optimization, 2958 signal events and just 2310 background events are expected. Diboson events are now the primary source of background, as the optimization greatly reduces the fake and charge misidentification backgrounds. As discussed earlier, the increase in the leading and subleading jet  $p_T$  cuts as well as the loosening of the centrality cut are most responsible for the changes in the signal and background yields; distributions of these quantities using the default and the optimized event selections can be found in Figures 6.6, 6.7, and 6.8, respectively.

It is important to note, however, that the MC sample used to estimate  $Z+jets$  events suffers from poor statistics which results in large per-event weights once scaled to  $\mathcal{L} = 3000 \text{ fb}^{-1}$ . This sample contributes heavily to the fake and charge misidentification backgrounds, and a handful of these events being cut out by the optimization contributes has a large effect on the dramatic reduction

|                               | All channels | $\mu\mu$ | $ee$ | $\mu e$ | $e\mu$ |
|-------------------------------|--------------|----------|------|---------|--------|
| $W^\pm W^\pm jj$ (QCD)        | 168.7        | 74.6     | 19.7 | 32.2    | 42.2   |
| Charge Misidentification      | 200          | 0.0      | 11   | 30      | 160    |
| Jets faking electrons         | 460          | 0.0      | 130  | 260     | 70     |
| $WZ + ZZ$                     | 1286         | 322      | 289  | 271     | 404    |
| Tribosons                     | 76           | 30.1     | 9.6  | 15.1    | 21.6   |
| Other non-prompt              | 120          | 29       | 16.6 | 50      | 19     |
| Total Background              | 2310         | 455      | 480  | 660     | 710    |
| Signal $W^\pm W^\pm jj$ (EWK) | 2958         | 1228     | 380  | 589     | 761    |

Table 6.6: Signal and background event yields using the optimized event selection for an integrated luminosity of  $\mathcal{L} = 3000 \text{ fb}^{-1}$ . Events containing a fake or charge-flipped electron are removed from their respective sources and combined into a single entry each.

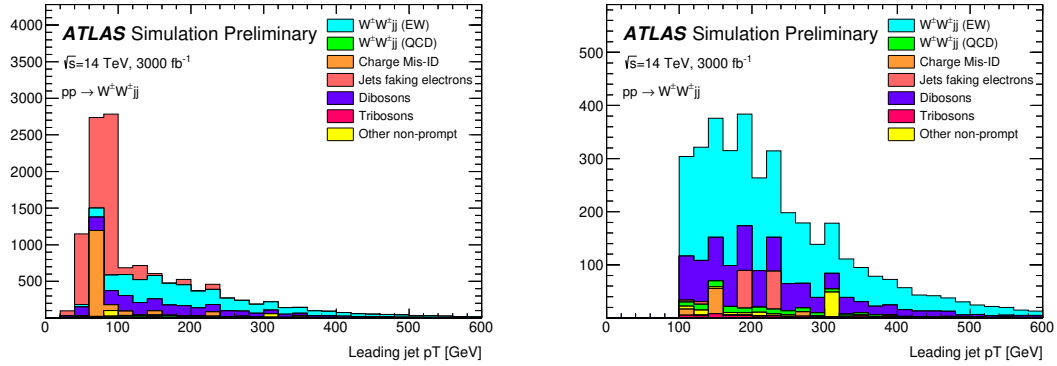


Figure 6.6:  $p_T$  distributions for the leading jet using the default (left) and optimized (right) event selections for all channels combined.

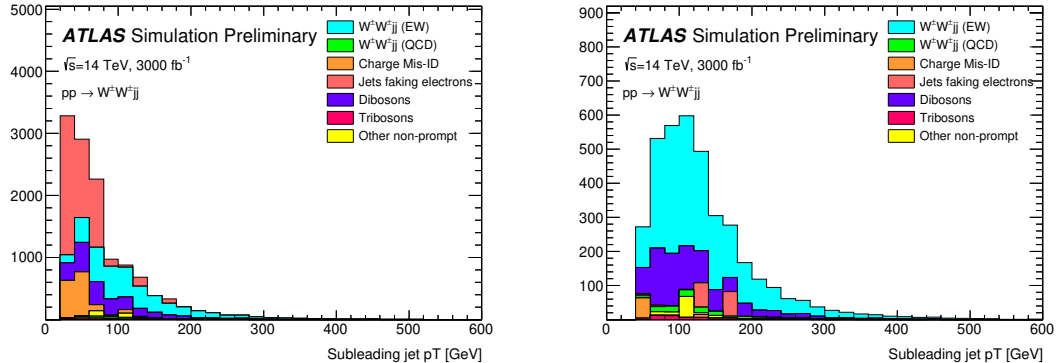


Figure 6.7:  $p_T$  distributions for the subleading jet using the default (left) and optimized (right) event selections for all channels combined.

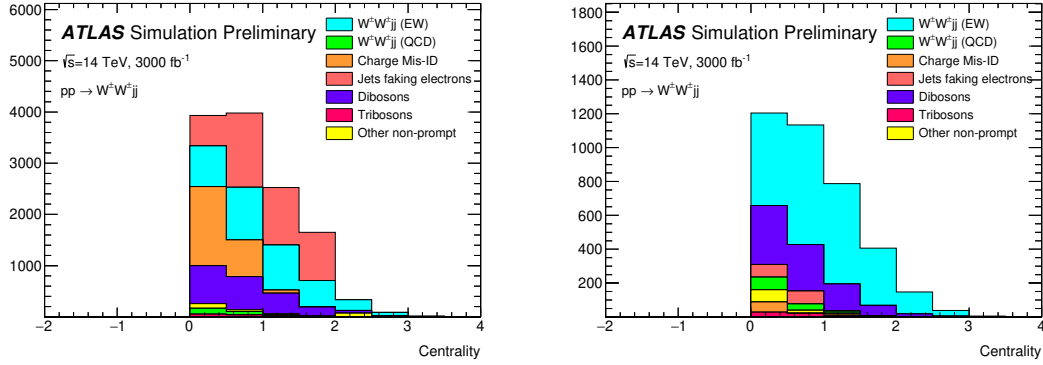


Figure 6.8:  $p_T$  distributions for lepton-jet centrality  $\zeta$  using the default (left) and optimized (right) event selections for all channels combined.

of these backgrounds. As a result, these particular optimized results are likely overly optimistic. However, given proper MC statistics, it is still expected that the optimization will outperform the default selection.

### 6.6.2 Uncertainties

**TODO:** Ask for details on how some of these uncertainties were calculated – specifically the fakes and charge mis-ID The uncertainties considered for the analysis are summarized in Table 6.7. Values for experimental systematics on the trigger efficiency, lepton and jet reconstruction, and flavor tagging are taken directly from the 13 TeV analysis [48]. The rate uncertainties for the background processes are halved from the 13 TeV values according to ATLAS recommendations.

| Source                                   | Uncertainty (%) |
|--|-----------------|
| $W^\pm W^\pm jj$ (EWK)                   | 3               |
| Luminosity                               | 1               |
| Trigger efficiency                       | 0.5             |
| Lepton reconstruction and identification | 1.8             |
| Jets                                     | 2.3             |
| Flavor tagging                           | 1.8             |
| Jets faking electrons                    | 20              |
| Charge misidentification                 | 25              |
| $W^\pm W^\pm jj$ (QCD)                   | 20              |
| Top                                      | 15              |
| Diboson                                  | 10              |
| Triboson                                 | 15              |

Table 6.7: Summary of estimated experimental and rate uncertainties.

2073 **6.6.3 Cross section measurement**

2074 The cross section is calculated using the same method as in the 13 TeV analysis, detailed in Sec-  
 2075 tion 5.4. Unlike the previous analysis, however, eight lepton channels are used here instead of six.  
 2076 The  $\mu e$  and  $e\mu$  channels remain separated in addition to the  $\mu\mu$  and  $ee$  channels, and each lepton  
 2077 flavor channel is further split by charge (i.e.  $\mu\mu \rightarrow \mu^+\mu^+ + \mu^-\mu^-$ ), as this increases the sensitivity  
 2078 of the analysis. Each channel's  $m_{jj}$  distribution is combined in a profile likelihood fit to extract  
 2079 the EWK  $W^\pm W^\pm jj$  production cross section. Using the default event selection, the expected cross  
 2080 section calculated to be:

$$\sigma_{W^\pm W^\pm jj}^{\text{expected}} = 16.89 \pm 0.36 \text{ (stat)} \pm 0.53 \text{ (theory)} \pm 0.84 \text{ (syst)} \text{ fb} \quad (6.5)$$

2081 and with the optimized event selection:

$$\sigma_{W^\pm W^\pm jj}^{\text{expected}} = 16.94 \pm 0.36 \text{ (stat)} \pm 0.53 \text{ (theory)} \pm 0.78 \text{ (syst)} \text{ fb} \quad (6.6)$$

2082 The optimized selection should not change the measured value of the cross section, and indeed both  
 2083 are consistent with within uncertainties. The systematic uncertainty is reduced by approximately  
 2084 7% with the optimized selection.

2085 Projections of the total uncertainty on the cross section as a function of integrated luminosity  
 2086 made by **TODO: how was this made?** is shown in Figure 6.9. As the integrated luminosity increases  
 2087 past  $\mathcal{L} > 3000 \text{ fb}^{-1}$ , the statistical uncertainty reduces faster than the systematic uncertainties.  
 2088 However, the total uncertainty is expected to reduce by less than a percent with increased luminosity  
 2089 past the planned  $3000 \text{ fb}^{-1}$ .

2090 **6.6.4 Longitudinal scattering significance**

2091 The longitudinal scattering significance is extracted in much the same way as the cross section, this  
 2092 time using a binned likelihood fit on the  $|\Delta\phi_{jj}|$  distribution. In order to increase sensitivity, the  
 2093  $|\Delta\phi_{jj}|$  distribution is split into two bins in  $m_{jj}$ , and an additional cut on the pseudorapidity of the  
 2094 subleading lepton is applied ( $|\eta| < 2.5$ ) to reduce background from fake and charge misidentification.  
 2095 The  $|\Delta\phi_{jj}|$  distributions used in the fit are shown in Figure 6.10. Due to limited statistics, the four  
 2096 lepton flavor channels are not split by charge. The expected significance of the  $W_L^\pm W_L^\pm jj$  process  
 2097 is  $1.8\sigma$  with a precision of 47% on the measurement. Projections of the expected significance as a  
 2098 function of integrated luminosity is shown in Figure 6.11.

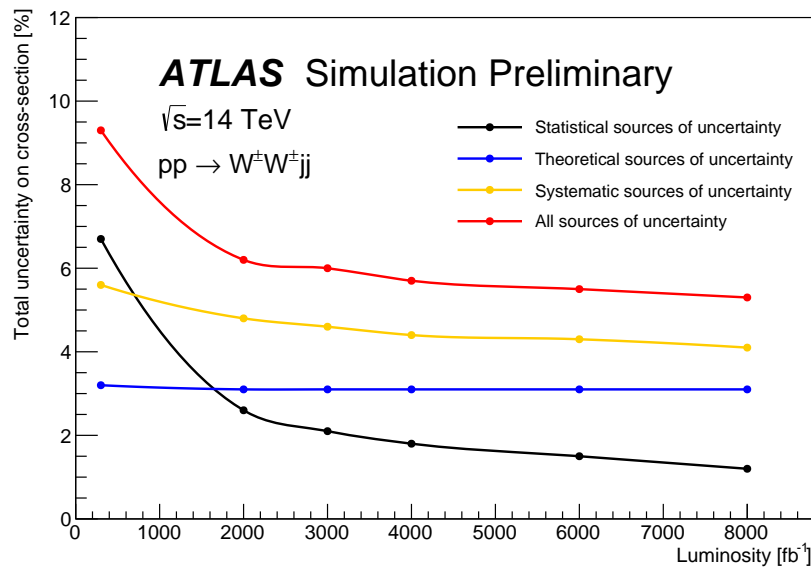


Figure 6.9: Projections of the statistical (black), theoretical (blue), systematic (yellow), and total (red) uncertainties on the measured cross section as a function of integrated luminosity using the optimized event selection.

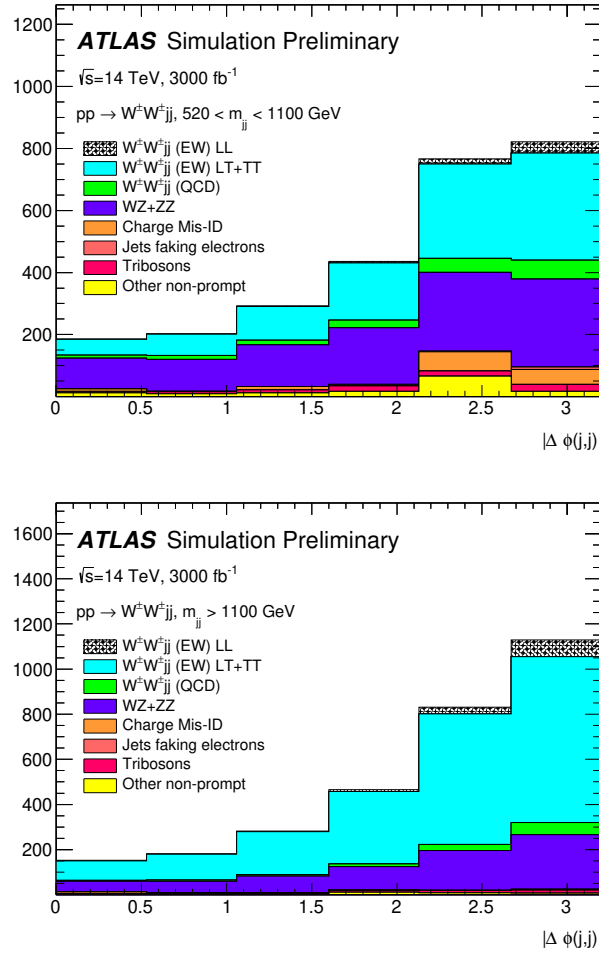


Figure 6.10: Dijet azimuthal separation ( $|\Delta\phi_{jj}|$ ) for the low  $m_{jj}$  region ( $520 < m_{jj} < 1100 \text{ GeV}$ , top) and the high  $m_{jj}$  region ( $m_{jj} > 1100 \text{ GeV}$ , bottom). The purely longitudinal (LL, gray) is plotted separately from the mixed and transverse (LT+TT, cyan) polarizations.

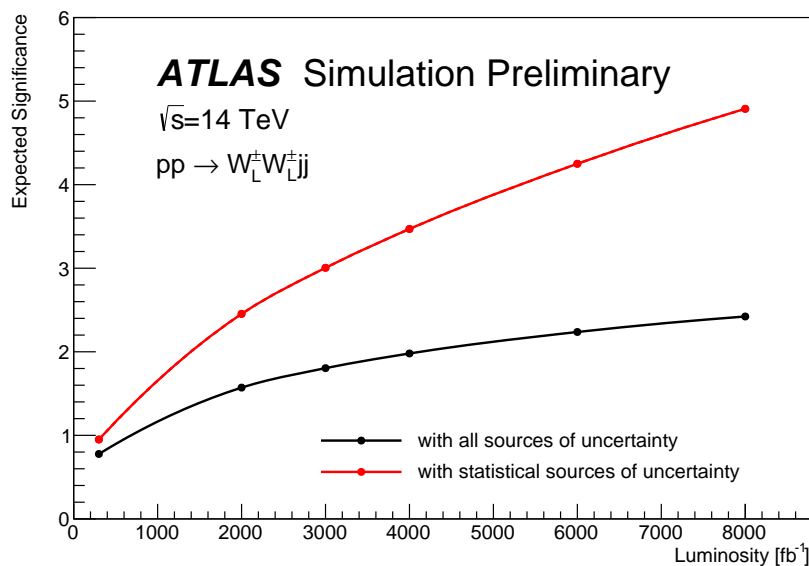


Figure 6.11: Projections of the expected longitudinal scattering significance as a function of integrated luminosity when considering all sources of uncertainties (black) or only statistical uncertainties (red).

2099

## CHAPTER 7

---

2100

## Conclusion

---

2101 Here's where you wrap it up.

2102 **Looking Ahead**

2103

2104 Here's an example of how to have an "informal subsection".

2105

## APPENDIX A

2106

---

# Additional material on

2107

## $W^\pm W^\pm jj$ measurement at $\sqrt{s} = 13$ TeV

---

2108

### A.1 Impact of experimental uncertainty on MC background estimations

2109 Tables A.1-A.6 contain the impact of experimental systematic uncertainties for the remaining back-  
2110 grounds estimated from MC simulation. The  $W^\pm W^\pm jj$  EWK signal and  $WZ$  background sys-  
2111 tematics are listed in the main body of the document, in Tables 5.21 and 5.22, respectively. While the  
2112 percentage of the contributions for some systematics appear large, the size of these backgrounds are  
2113 quite small compared to the total background.

| $W^\pm W^\pm jj$ QCD      | $ee$ % Yield | $e\mu$ % Yield | $\mu\mu$ % Yield |
|---------------------------|--------------|----------------|------------------|
| Jet-related Uncertainties | 3.41         | 3.04           | 2.85             |
| b-tagging efficiency      | 2.56         | 2.48           | 2.48             |
| Pile-up                   | 4.99         | 0.45           | 0.33             |
| Trigger efficiency        | 0.02         | 0.08           | 0.41             |
| Lepton reconstruction/ID  | 1.62         | 1.19           | 1.89             |
| MET reconstruction        | 0.41         | 0.22           | 0.34             |

Table A.1: Impact of experimental uncertainties for the  $W^\pm W^\pm jj$  QCD processes in all channels.

| Triboson                  | $ee$ % Yield | $e\mu$ % Yield | $\mu\mu$ % Yield |
|---------------------------|--------------|----------------|------------------|
| Jet-related Uncertainties | 13.09        | 13.39          | 16.85            |
| b-tagging efficiency      | 2.96         | 3.77           | 4.95             |
| Pile-up                   | 19.37        | 24.66          | 6.87             |
| Trigger efficiency        | 0.02         | 0.07           | 0.47             |
| Lepton reconstruction/ID  | 1.66         | 1.27           | 2.48             |
| MET reconstruction        | 0.00         | 0.46           | 0.00             |

Table A.2: Impact of experimental uncertainties for triboson process in all channels.

| $t\bar{t}V$               | $ee$ % Yield | $e\mu$ % Yield | $\mu\mu$ % Yield |
|---------------------------|--------------|----------------|------------------|
| Jet-related Uncertainties | 17.65        | 11.97          | 14.27            |
| b-tagging efficiency      | 15.02        | 9.04           | 13.83            |
| Pile-up                   | 8.73         | 10.69          | 4.18             |
| Trigger efficiency        | 0.03         | 0.08           | 0.39             |
| Lepton reconstruction/ID  | 2.57         | 3.27           | 2.66             |
| MET reconstruction        | 1.75         | 4.16           | 1.62             |

Table A.3: Impact of experimental uncertainties for  $t\bar{t}V$  processes in all channels.

| $W\gamma$                 | $ee$ % Yield | $e\mu$ % Yield | $\mu\mu$ % Yield |
|---------------------------|--------------|----------------|------------------|
| Jet-related Uncertainties | 7.05         | 33.36          | —                |
| b-tagging efficiency      | 1.97         | 2.94           | —                |
| Pile-up                   | 4.11         | 14.17          | —                |
| Trigger efficiency        | 0.01         | 0.14           | —                |
| Lepton reconstruction/ID  | 1.40         | 1.13           | —                |
| MET reconstruction        | 0.00         | 0.00           | —                |

Table A.4: Impact of experimental uncertainties for the  $W\gamma$  process in all channels.

| $Z\gamma$                 | $ee$ % Yield | $e\mu$ % Yield | $\mu\mu$ % Yield |
|---------------------------|--------------|----------------|------------------|
| Jet-related Uncertainties | 16.22        | 370.44         | —                |
| b-tagging efficiency      | 1.08         | 3.10           | —                |
| Pile-up                   | 12.57        | 11.51          | —                |
| Trigger efficiency        | 0.02         | 0.07           | —                |
| Lepton reconstruction/ID  | 1.26         | 22.01          | —                |
| MET reconstruction        | 0.00         | 0.00           | —                |

Table A.5: Impact of experimental uncertainties for the  $Z\gamma$  process in all channels.

| $ZZ$                      | $ee$ % Yield | $e\mu$ % Yield | $\mu\mu$ % Yield |
|---------------------------|--------------|----------------|------------------|
| Jet-related Uncertainties | 15.71        | 15.76          | 35.18            |
| b-tagging efficiency      | 2.23         | 2.35           | 2.89             |
| Pile-up                   | 1.22         | 3.20           | 4.58             |
| Trigger efficiency        | 0.03         | 0.10           | 0.36             |
| Lepton reconstruction/ID  | 3.59         | 3.10           | 5.70             |
| MET reconstruction        | 4.84         | 3.26           | 3.24             |

Table A.6: Impact of experimental uncertainties for the  $ZZ$  process in all channels.

2114 **A.2 Additional signal region plots**

2115

## APPENDIX B

2116

---

# Additional material on $W^\pm W^\pm jj$ prospects

2117

## at the HL-LHC

---

2118

### B.1 Truth isolation

2119 As mentioned in Section 6.3.1, the size of the background contribution from top processes are much  
 2120 larger than expected when no isolation is applied. The event yields using an earlier version of the  
 2121 event selection with no truth-based isolation requirement are listed in Table B.1. Here, top events  
 2122 make up nearly 90% of the total background, and the contributions from fake and charge-flipped  
 2123 electrons are also large. The event yields using the same event selection with the truth-based isolation  
 2124 included are shown in Figure B.2. When comparing the two tables, the considerable reduction in  
 the top background can be clearly seen.

| yields by type | all channels | $\mu\mu$ | $ee$    | $\mu e$ | $e\mu$  |
|----------------|--------------|----------|---------|---------|---------|
| signal         | 4011         | 1583.2   | 531.7   | 793.1   | 1103.1  |
| ww qcd         | 252.6        | 105.8    | 30.4    | 48      | 68.4    |
| charge flip    | 2528.4       | 0.0      | 2075.4  | 255.1   | 197.8   |
| fakes          | 7135.4       | 0.0      | 4675.1  | 1904.3  | 555.9   |
| diboson        | 2370.4       | 581.2    | 491.8   | 517.9   | 779.6   |
| triboson       | 125.5        | 49.1     | 17.8    | 24.6    | 34.1    |
| top            | 90150.5      | 26618    | 15301.6 | 25277.9 | 22953.1 |
| z+jets         | 241.2        | 0.0      | 0.0     | 0.0     | 241.2   |
| w+jets         | 31.4         | 3.9      | 7.6     | 13.2    | 6.7     |
| total bkg      | 102803.9     | 27354    | 22592   | 28027.8 | 24830.1 |
| signal         | 4011         | 1583.2   | 531.7   | 793.1   | 1103.1  |

Table B.1: Event yields prior to applying any form of truth-based isolation criteria.

2125

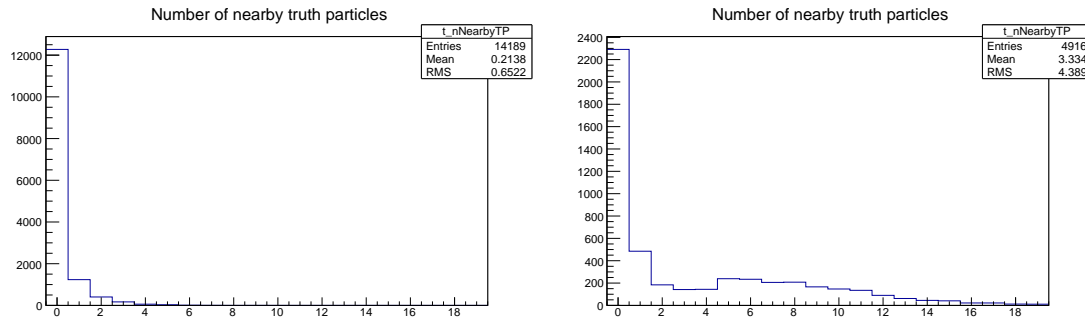
2126 **TODO:** Add tables for tight vs loose working point, information on the necessity of TRUTH1++

| yields by type | all channels | $\mu\mu$ | $ee$   | $\mu e$ | $e\mu$ |
|----------------|--------------|----------|--------|---------|--------|
| signal         | 3470.5       | 1427.3   | 428.8  | 675.8   | 938.7  |
| ww qcd         | 205.8        | 90.8     | 22.7   | 38.3    | 54     |
| charge flip    | 2398.3       | 0.0      | 2104.6 | 95.8    | 197.9  |
| fakes          | 4309.7       | 0.0      | 3390.6 | 750.8   | 168.3  |
| diboson        | 1552.4       | 311.3    | 355.6  | 346.8   | 538.7  |
| triboson       | 115          | 46.8     | 15.4   | 21.6    | 31.2   |
| top            | 156.9        | 42.3     | 14.8   | 76.6    | 23.3   |
| $z+jets$       | 0.0          | 0.0      | 0.0    | 0.0     | 0.0    |
| $w+jets$       | 0.3          | 0.0      | 0.0    | 0.3     | 0.0    |
| total bkg      | 8738.1       | 491.3    | 5903.7 | 1329.8  | 1013.4 |
| signal         | 3470.5       | 1427.3   | 428.8  | 675.8   | 938.7  |

Table B.2: Event yields after applying a test version of the truth-based isolation.

### 2127 B.1.1 TRUTH1++ derivations

2128 The ATLAS standard TRUTH1 derivations used for this analysis contain a slimmed truth particle  
 2129 container in order to reduce the file size. As a result, many of the truth particles that would be  
 2130 included in the isolation variables are missing, and the truth-based isolation will not accurately  
 2131 model the reconstruction-level isolation variables. In order to recover the performance of the truth-  
 2132 based isolation in the top MC samples (where it is most needed), a custom derivation was produced  
 2133 privately that duplicated the default TRUTH1 data structure but includes the full truth particle  
 2134 record. The reduced size of the truth particle information in the TRUTH1 derivation compared to the  
 2135 TRUTH1++ derivation is shown in Figure B.1.

Figure B.1: Number of truth particles within  $\Delta R < 0.4$  of a selected muon or electron using the ATLAS standard TRUTH1 (left) and the custom TRUTH1++ (right) derivations in  $t\bar{t}$  simulation. The complete truth record is stored in the TRUTH1++ derivation, and this is best seen in the first bin, where the lepton has no nearby truth particles.

2136 **B.1.2 Check of truth-based isolation**

2137 Since the isolation variables are constructed from truth particles, there is an expectation that the  
 2138 efficiency of the isolation selection will be higher than what would be seen in the full simulation.  
 2139 In order to test this, a truth-level 13 TeV  $t\bar{t}$  MC sample was run through a selection altered to  
 2140 mimic the 13 TeV  $W^\pm W^\pm jj$  measurement as closely as possible. The results were compared to the  
 2141  $t\bar{t}$  background in the 13 TeV analysis extrapolated to 14 TeV and  $3000 \text{ fb}^{-1}$ , and the truth-based  
 2142 isolation reduces the expected events by a factor of approximately 4. However, the statistics in the  
 2143 13 TeV truth-level sample are low, and it is therefore difficult to measure precisely how much the  
 2144 truth-based isolation overperforms.

2145 **B.1.3 Loose isolation working point**

2146 As another check on the truth-based isolation, a second isolation working point was constructed  
 2147 to match the official ATLAS Fixed Cut Loose isolation working point. The definition of this loose  
 2148 isolation are found in Table B.3.

2149 The primary impact of loosening the isolation is a substantial increase in the non-prompt back-  
 2150 round from top processes, and a moderate increase in the charge mis-ID and fake backgrounds.  
 2151 Backgrounds from prompt leptons only did not see major changes. As a result, the tight working  
 2152 point is chosen for the analysis. The event yields by sample and by background type using the  
 2153 loose working point are in Table B.4, and Table B.5 has the numbers using the tight working point  
 2154 (defined in Table 6.2) for comparison.

|   | Electron Isolation      | Muon Isolation            |
|---|-------------------------|---------------------------|
| Track-based isolation cone size         | $\Delta R < 0.2$        | $\Delta R < 0.3$          |
| Track-based isolation requirement       | $\sum p_T/p_T^e < 0.15$ | $\sum p_T/p_T^\mu < 0.15$ |
| Calorimeter-based isolation cone size   | $\Delta R < 0.2$        | $\Delta R < 0.2$          |
| Calorimeter-based isolation requirement | $\sum E_T/p_T^e < 0.2$  | $\sum E_T/p_T^\mu < 0.3$  |

Table B.3: Electron and muon isolation requirements for the loose working point.

| run number  | all channels |         |        | mm      |        |       | ee      |         |       | me      |        |       | em      |        |       |
|-------------|--------------|---------|--------|---------|--------|-------|---------|---------|-------|---------|--------|-------|---------|--------|-------|
|             | events       | stat    | sys    | events  | stat   | sys   | events  | stat    | sys   | events  | stat   | sys   | events  | stat   | sys   |
| signal      | 3783.21      | 22.08   | 0.00   | 1524.99 | 15.00  | 0.00  | 484.74  | 7.01    | 0.00  | 740.76  | 9.01   | 0.00  | 1032.72 | 11.50  | 0.00  |
| ww qcd      | 223.95       | 3.54    | 44.79  | 97.17   | 2.51   | 19.43 | 25.51   | 1.03    | 42.23 | 1.40    | 8.45   | 59.04 | 1.80    | 11.81  |       |
| charge flip | 3025.40      | 1276.74 | 0.00   | 0.00    | 0.00   | 0.00  | 2615.30 | 1267.89 | 0.00  | 197.20  | 87.94  | 0.00  | 212.90  | 121.63 | 0.00  |
| fakes       | 5315.55      | 1775.87 | 0.00   | 0.00    | 0.00   | 0.00  | 3524.24 | 1694.39 | 0.00  | 1356.74 | 450.60 | 0.00  | 434.57  | 282.33 | 0.00  |
| diboson     | 2195.61      | 38.10   | 219.58 | 548.72  | 18.54  | 54.87 | 451.27  | 18.29   | 45.14 | 470.61  | 15.71  | 47.07 | 725.01  | 22.95  | 72.50 |
| triboson    | 117.43       | 5.90    | 17.62  | 47.55   | 4.32   | 7.13  | 15.83   | 1.94    | 2.37  | 22.11   | 2.18   | 3.32  | 31.94   | 2.76   | 4.80  |
| top         | 554.63       | 218.75  | 83.21  | 229.26  | 135.53 | 34.40 | 61.15   | 38.23   | 9.18  | 232.30  | 167.28 | 34.85 | 31.92   | 6.43   | 4.78  |
| z+jets      | 0.00         | 0.00    | 0.00   | 0.00    | 0.00   | 0.00  | 0.00    | 0.00    | 0.00  | 0.00    | 0.00   | 0.00  | 0.00    | 0.00   | 0.00  |
| w+jets      | 1.21         | 0.87    | 0.00   | 0.00    | 0.00   | 0.00  | 0.00    | 0.00    | 0.00  | 0.00    | 0.00   | 0.00  | 0.02    | 0.00   | 0.00  |
| total bkg   | 11433.78     | 2198.44 | 239.70 | 922.70  | 136.88 | 67.99 | 6693.30 | 2116.67 | 46.41 | 2322.38 | 488.89 | 59.27 | 1495.40 | 308.36 | 73.77 |
| signal      | 3783.21      | 22.08   | 0.00   | 1524.99 | 15.00  | 0.00  | 484.74  | 7.01    | 0.00  | 740.76  | 9.01   | 0.00  | 1032.72 | 11.50  | 0.00  |

Table B.4: Event yields broken down by sample and by background type using the loose isolation workingpoint. Events containing a fake or charge-flipped electron are removed from their respective sample and added to the ‘fakes’ and ‘charge flip’ rows, respectively. Errors include statistical uncertainty and estimated systematic rate uncertainty based on the background process.

| run number  | all channels |         |        | mm      |       |       | ee      |         |       | me      |        |       | em      |        |       |
|-------------|--------------|---------|--------|---------|-------|-------|---------|---------|-------|---------|--------|-------|---------|--------|-------|
|             | events       | stat    | sys    | events  | stat  | sys   | events  | stat    | sys   | events  | stat   | sys   | events  | stat   | sys   |
| signal      | 3489.49      | 21.23   | 0.00   | 1434.85 | 14.55 | 0.00  | 431.75  | 6.61    | 0.00  | 679.09  | 8.63   | 0.00  | 943.8   | 11.00  | 0.00  |
| ww qcd      | 206.42       | 3.41    | 41.28  | 91.12   | 2.43  | 18.22 | 22.84   | 0.98    | 4.57  | 38.37   | 1.34   | 7.67  | 54.09   | 1.72   | 10.82 |
| charge flip | 2335.73      | 1163.47 | 0.00   | 0.00    | 0.00  | 0.00  | 2087.78 | 1159.5  | 0.00  | 90.37   | 33.32  | 0.00  | 157.58  | 90.02  | 0.00  |
| fakes       | 4979.27      | 1756.47 | 0.00   | 0.00    | 0.00  | 0.00  | 3406.20 | 1705.03 | 0.00  | 1230.80 | 362.15 | 0.00  | 342.27  | 216.54 | 0.00  |
| diboson     | 2039.94      | 36.93   | 204.00 | 499.69  | 18.04 | 49.97 | 437.60  | 14.12   | 43.76 | 422.90  | 14.18  | 42.29 | 679.75  | 25.25  | 67.98 |
| triboson    | 115.03       | 5.87    | 17.29  | 46.84   | 4.31  | 7.03  | 15.40   | 1.94    | 2.32  | 21.55   | 2.17   | 3.24  | 31.24   | 2.74   | 4.70  |
| top         | 211.74       | 84.14   | 31.76  | 107.96  | 71.12 | 16.20 | 19.58   | 3.76    | 2.93  | 57.21   | 44.47  | 8.58  | 26.99   | 5.40   | 4.05  |
| z+jets      | 0.00         | 0.00    | 0.00   | 0.00    | 0.00  | 0.00  | 0.00    | 0.00    | 0.00  | 0.00    | 0.00   | 0.00  | 0.00    | 0.00   | 0.00  |
| w+jets      | 0.30         | 0.28    | 0.00   | 0.00    | 0.00  | 0.00  | 0.00    | 0.00    | 0.00  | 0.28    | 0.28   | 0.00  | 0.02    | 0.02   | 0.00  |
| total bkg   | 9888.43      | 2108.87 | 211.25 | 745.61  | 73.54 | 56.04 | 5898.40 | 2061.99 | 44.16 | 1861.48 | 366.67 | 43.95 | 1291.94 | 235.95 | 69.11 |
| signal      | 3489.49      | 21.23   | 0.00   | 1434.85 | 14.55 | 0.00  | 431.75  | 6.61    | 0.00  | 679.09  | 8.63   | 0.00  | 943.80  | 11.00  | 0.00  |

Table B.5: Event yields broken down by background type using the tight isolation workingpoint. Events containing a fake or charge-flipped electron are removed from their respective sample and added to the “fakes” and “charge flip” rows, respectively. Errors include statistical uncertainty and estimated systematic rate uncertainty based on the background process.

2155 **B.2 Plots of other optimization variables**

2156 Plots of the remaining optimization variables not shown in Section 6.5.3 are presented here for  
2157 reference. Figures B.2, B.3, and B.4 compare signal and background distributions for the default  
2158 and optimized cuts. None of these cuts change by much in the optimized selection and their impacts  
2159 on the overall event selection is minimal.

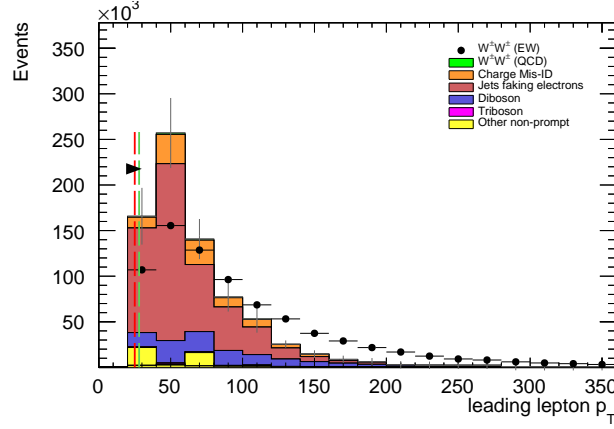


Figure B.2: Leading lepton  $p_T$  distribution. The default and optimized cuts are represented by the red and green dashed lines, respectively. The  $W^\pm W^\pm jj$  EWK signal (black points) is normalized to the same area as the sum of the backgrounds (colored histogram).

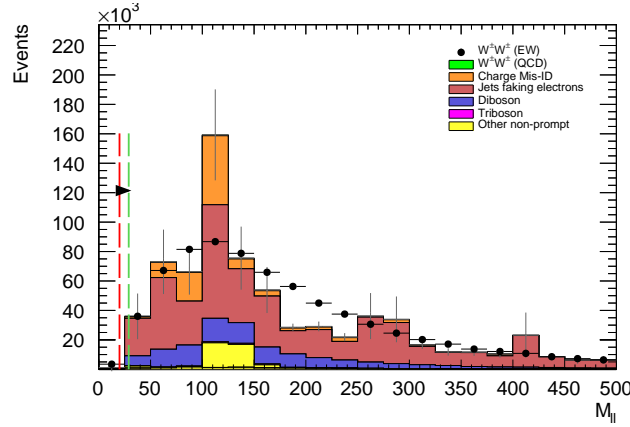


Figure B.3: Dilepton invariant mass distribution. The default and optimized cuts are represented by the red and green dashed lines, respectively. The  $W^\pm W^\pm jj$  EWK signal (black points) is normalized to the same area as the sum of the backgrounds (colored histogram).

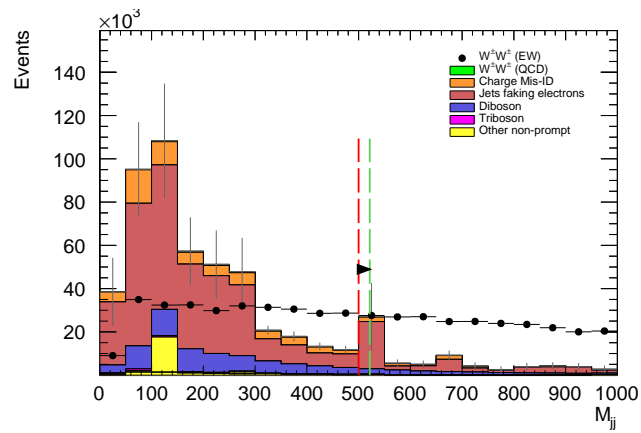


Figure B.4: Dijet invariant mass distribution. The default and optimized cuts are represented by the red and green dashed lines, respectively. The  $W^\pm W^\pm jj$  EWK signal (black points) is normalized to the same area as the sum of the backgrounds (colored histogram).

---

## Bibliography

---

- 2161 [1] ATLAS Collaboration, M. Aaboud et al., *Measurement of the  $W^\pm Z$  boson pair-production*  
 2162 *cross section in  $pp$  collisions at  $\sqrt{s} = 13$  TeV with the ATLAS Detector*, *Phys. Lett.* **B762**  
 2163 (2016) 1–22, [arXiv:1606.04017 \[hep-ex\]](#). (document)
- 2164 [2] S. Weinberg, *The Quantum Theory of Fields, Volume 1: Foundations*. Cambridge University  
 2165 Press, 1995. [2.1](#)
- 2166 [3] M. E. Peskin and D. V. Schroeder, *An Introduction to Quantum Field Theory*.  
 2167 Addison-Wesley, 1995. [2.1](#)
- 2168 [4] R. P. Feynman, *Mathematical formulation of the quantum theory of electromagnetic*  
 2169 *interaction*, *Phys. Rev.* **80** (1950) 440–457. [2.1](#)
- 2170 [5] M. Y. Han and Y. Nambu, *Three-triplet model with double SU(3) symmetry*, *Phys. Rev.* **139**  
 2171 (1965) B1006–B1010. [2.1](#)
- 2172 [6] D. J. Gross and F. Wilczek, *Asymptotically Free Gauge Theories - I*, *Phys. Rev.* **D8** (1973)  
 2173 3633–3652. [2.1](#)
- 2174 [7] D. J. Gross and F. Wilczek, *ASYMPTOTICALLY FREE GAUGE THEORIES. 2.*, *Phys.*  
 2175 *Rev.* **D9** (1974) 980–993. [2.1](#)
- 2176 [8] H. D. Politzer, *Reliable Perturbative Results for Strong Interactions?*, *Phys. Rev. Lett.* **30**  
 2177 (1973) 1346–1349. [,274(1973)]. [2.1](#)
- 2178 [9] A. Salam and J. C. Ward, *Weak and Electromagnetic Interactions*, *Nuovo Cimento* **11** (1959)  
 2179 568–577. [2.1](#)
- 2180 [10] S. L. Glashow, *The Renormalizability of Vector Meson Interactions*, *Nucl. Phys.* **10** (1959)  
 2181 107–117. [2.1](#)
- 2182 [11] ALEPH, DELPHI, L3, OPAL, SLD, LEP Electroweak Working Group, SLD Electroweak  
 2183 Group, SLD Heavy Flavour Group Collaboration, S. Schael et al., *Precision electroweak*  
 2184 *measurements on the  $Z$  resonance*, *Phys. Rept.* **427** (2006) 257–454, [arXiv:hep-ex/0509008](#)  
 2185 [hep-ex]. [2.1](#)
- 2186 [12] F. Englert and R. Brout, *Broken symmetry and the mass of gauge vector mesons*, *Phys. Rev.*  
 2187 *Lett.* **13** (1964) 321–323. [2.1](#)

- 2188 [13] P. W. Higgs, *Broken symmetries, massless particles and gauge fields*, Physics Letters **12**  
 2189 (1964) 132–133. 2.1
- 2190 [14] P. W. Higgs, *Broken symmetries and the masses of gauge bosons*, Phys. Rev. Lett. **13** (1964)  
 2191 508–509. 2.1
- 2192 [15] ATLAS Collaboration, *Observation of a new particle in the search for the Standard Model*  
 2193 *Higgs boson with the ATLAS detector at the LHC*, Phys. Lett. B **716** (2012) 1,  
 2194 arXiv:1207.7214 [hep-ex]. 2.1, 5.0.2
- 2195 [16] CMS Collaboration, *Observation of a new boson at a mass of 125 GeV with the CMS*  
 2196 *experiment at the LHC*, Phys. Lett. B **716** (2012) 30, arXiv:1207.7235 [hep-ex]. 2.1, 5.0.2
- 2197 [17] UA1 Collaboration, G. Arnison et al., *Experimental Observation of Isolated Large Transverse*  
 2198 *Energy Electrons with Associated Missing Energy at  $s^{**}(1/2) = 540\text{-GeV}$* , Phys. Lett. **B122**  
 2199 (1983) 103–116. [,611(1983)]. 2.2
- 2200 [18] UA1 Collaboration, G. Arnison et al., *Experimental Observation of Lepton Pairs of Invariant*  
 2201 *Mass Around  $95\text{-GeV}/c^{**2}$  at the CERN SPS Collider*, Phys. Lett. **B126** (1983) 398–410.  
 2202 [,7.55(1983)]. 2.2
- 2203 [19] Particle Data Group Collaboration, K. A. Olive et al., *Review of Particle Physics*, Chin.  
 2204 Phys. **C38** (2014) 090001. 2.2, 2.2
- 2205 [20] D. R. Green, P. Meade, and M.-A. Pleier, *Multiboson interactions at the LHC*, Rev. Mod.  
 2206 Phys. **89** (2017) no. 3, 035008, arXiv:1610.07572 [hep-ex]. 2.3
- 2207 [21] H.-J. He and W. B. Kilgore, *The Equivalence theorem and its radiative correction - free*  
 2208 *formulation for all  $R(xi)$  gauges*, Phys. Rev. **D55** (1997) 1515–1532, arXiv:hep-ph/9609326  
 2209 [hep-ph]. 2.3
- 2210 [22] B. W. Lee, C. Quigg, and H. B. Thacker, *The Strength of Weak Interactions at Very*  
 2211 *High-Energies and the Higgs Boson Mass*, Phys. Rev. Lett. **38** (1977) 883–885. 2.3
- 2212 [23] S. D. Rindani, *Strong gauge boson scattering at the LHC*, in *Physics at the Large Hadron*  
 2213 *Collider*, A. Datta, B. Mukhopadhyaya, A. Raychaudhuri, A. K. Gupta, C. L. Khetrapal,  
 2214 T. Padmanabhan, and M. Vijayan, eds., pp. 145–155. 2009. arXiv:0910.5068 [hep-ph]. 2.3, 2.3
- 2215 [24] V. D. Barger, K.-m. Cheung, T. Han, and R. J. N. Phillips, *Strong  $W^+W^+$  scattering signals*  
 2216 *at pp supercolliders*, Phys. Rev. **D42** (1990) 3052–3077. 2.3
- 2217 [25] G. van den Oord, *Recursion, Monte Carlo and Vector Boson Scattering at Hadron Colliders*.  
 2218 PhD thesis, Nijmegen U., 2012.  
 2219 [http://www.nikhef.nl/pub/services/biblio/theses\\_pdf/thesis\\_G\\_v\\_d\\_Oord.pdf](http://www.nikhef.nl/pub/services/biblio/theses_pdf/thesis_G_v_d_Oord.pdf). 2.3,  
 2220 2.3
- 2221 [26] A. Alboteanu, W. Kilian, and J. Reuter, *Resonances and Unitarity in Weak Boson Scattering*  
 2222 *at the LHC*, JHEP **11** (2008) 010, arXiv:0806.4145 [hep-ph]. 2.5
- 2223 [27] L. R. Evans and P. Bryant, *LHC Machine*, JINST **3** (2008) S08001.  
 2224 <https://cds.cern.ch/record/1129806>. This report is an abridged version of the LHC  
 2225 Design Report (CERN-2004-003). 3.1

- 2226 [28] ATLAS Collaboration, *The ATLAS Experiment at the CERN Large Hadron Collider*, JINST  
2227 **3** (2008) S08003. 3.1
- 2228 [29] ATLAS Collaboration, *ATLAS inner detector: Technical Design Report, Vol. 1*. CERN,  
2229 Geneva, 1997. <https://cds.cern.ch/record/331063>. 4
- 2230 [30] P. F. Åkesson, T. Atkinson, M. J. Costa, M. Elsing, S. Fleischmann, A. N. Gaponenko,  
2231 W. Liebig, E. Moyse, A. Salzburger, and M. Siebel, *ATLAS Tracking Event Data Model*,  
2232 Tech. Rep. ATL-SOFT-PUB-2006-004. ATL-COM-SOFT-2006-005.  
2233 CERN-ATL-COM-SOFT-2006-005, CERN, Geneva, Jul, 2006.  
2234 <https://cds.cern.ch/record/973401>. 4.1
- 2235 [31] P. Brückman, A. Hicheur, and S. J. Haywood, *Global chi2 approach to the Alignment of the*  
2236 *ATLAS Silicon Tracking Detectors*, Tech. Rep. ATL-INDET-PUB-2005-002.  
2237 ATL-COM-INDET-2005-004. CERN-ATL-INDET-PUB-2005-002, CERN, Geneva, 2005.  
2238 <https://cds.cern.ch/record/835270>. 4.1, 4.1
- 2239 [32] ATLAS Collaboration Collaboration, *Alignment of the ATLAS Inner Detector Tracking*  
2240 *System with 2010 LHC proton-proton collisions at  $\sqrt{s} = 7$  TeV*, Tech. Rep.  
2241 ATLAS-CONF-2011-012, CERN, Geneva, Mar, 2011.  
2242 <https://cds.cern.ch/record/1334582>. 4.1, 4.2.3, 4.14
- 2243 [33] R. Härtel and S. Bethke, *Iterative local Chi2 alignment approach for the ATLAS SCT*  
2244 *detector*, Nov, 2005. <http://cds.cern.ch/record/1511044>. Presented 28 Nov 2005. 4.1
- 2245 [34] ATLAS Collaboration Collaboration, P. Brückman de Renstrom, *Alignment strategy for the*  
2246 *Inner Detector of ATLAS*, . <https://cds.cern.ch/record/1047114>. 4.1
- 2247 [35] *Alignment of the ATLAS Inner Detector and its Performance in 2012*, Tech. Rep.  
2248 ATLAS-CONF-2014-047, CERN, Geneva, Jul, 2014.  
2249 <https://cds.cern.ch/record/1741021>. 4.1, 4.2.1, 4.4
- 2250 [36] J. J. Peña, *Alignment of the ATLAS Inner Detector Upgraded for the LHC Run II*, J. Phys.  
2251 Conf. Ser. **664** (2015) no. 7, 072025. 4.1
- 2252 [37] J. Alison and I. J. Kroll, *The Road to Discovery: Detector Alignment, Electron Identification,*  
2253 *Particle Misidentification, WW Physics, and the Discovery of the Higgs Boson*, Dec, 2015.  
2254 <https://cds.cern.ch/record/1536507>. Presented 08 Nov 2012. 6
- 2255 [38] *ATLAS Inner Detector Alignment Performance with February 2015 Cosmic Rays Data*, Tech.  
2256 Rep. ATL-PHYS-PUB-2015-009, CERN, Geneva, Apr, 2015.  
2257 <https://cds.cern.ch/record/2008724>. 4.3, 4.2
- 2258 [39] ATLAS Collaboration Collaboration, M. Capeans, G. Darbo, K. Einsweiller, M. Elsing,  
2259 T. Flick, M. Garcia-Sciveres, C. Gemme, H. Pernegger, O. Rohne, and R. Vuillermet, *ATLAS*  
2260 *Insertable B-Layer Technical Design Report*, Tech. Rep. CERN-LHCC-2010-013.  
2261 ATLAS-TDR-19, Sep, 2010. <https://cds.cern.ch/record/1291633>. 4.2
- 2262 [40] *Alignment of the ATLAS Inner Detector with the initial LHC data at  $\sqrt{s} = 13$  TeV*, Tech.  
2263 Rep. ATL-PHYS-PUB-2015-031, CERN, Geneva, Jul, 2015.  
2264 <https://cds.cern.ch/record/2038139>. 4.2

- 2265 [41] *Study of the mechanical stability of the ATLAS Insertable B-Layer*, Tech. Rep.  
2266 ATL-INDET-PUB-2015-001, CERN, Geneva, Jun, 2015.  
2267 <https://cds.cern.ch/record/2022587>. 4.2.1
- 2268 [42] *Common Framework Implementation for the Track-Based Alignment of the ATLAS Detector*,  
2269 Tech. Rep. ATL-SOFT-PUB-2014-003, CERN, Geneva, Mar, 2014.  
2270 <https://cds.cern.ch/record/1670354>. 4.2.1
- 2271 [43] ATLAS Collaboration Collaboration, *Study of alignment-related systematic effects on the*  
2272 *ATLAS Inner Detector track reconstruction*, Tech. Rep. ATLAS-CONF-2012-141, CERN,  
2273 Geneva, Oct, 2012. <https://cds.cern.ch/record/1483518>. 4.4, 4.4, 4.4.1.1, 4.4.1.2
- 2274 [44] S. Marti-Garcia, S. Camarda, T. Golling, M. Danninger, N. A. Styles, J. Wollrath, W. K.  
2275 Di Clemente, S. Henkelmann, J. Jimenez Peña, O. Estrada Pastor, A. K. Morley, H. Oide,  
2276 A. T. Vermeulen, P. Butti, E. Ricci, F. M. Follega, and R. Iuppa, *Studies of radial distortions*  
2277 *of the ATLAS Inner Detector*, Tech. Rep. ATL-COM-INDET-2018-010, CERN, Geneva, Mar,  
2278 2018. <https://cds.cern.ch/record/2306724>. 4.4
- 2279 [45] ATLAS Collaboration Collaboration, *Electron and photon energy calibration with the ATLAS*  
2280 *detector using data collected in 2015 at  $\sqrt{s} = 13$  TeV*, Tech. Rep. ATL-PHYS-PUB-2016-015,  
2281 CERN, Geneva, Aug, 2016. <https://cds.cern.ch/record/2203514>. 4.4.1
- 2282 [46] ATLAS Collaboration, ATLAS Collaboration, *Evidence for Electroweak Production*  
2283 *of  $W^\pm W^\pm jj$  in  $pp$  Collisions at  $\sqrt{s} = 8$  TeV with the ATLAS Detector*, *Phys. Rev. Lett.* **113**  
2284 (2014) no. 14, 141803, arXiv:1405.6241 [hep-ex]. 5
- 2285 [47] CMS Collaboration, V. Khachatryan et al., *Study of vector boson scattering and search for*  
2286 *new physics in events with two same-sign leptons and two jets*, *Phys. Rev. Lett.* **114** (2015)  
2287 no. 5, 051801, arXiv:1410.6315 [hep-ex]. 5
- 2288 [48] ATLAS Collaboration Collaboration, *Observation of electroweak production of a same-sign  $W$*   
2289 *boson pair in association with two jets in  $pp$  collisions at  $\sqrt{s} = 13$  TeV with the ATLAS*  
2290 *detector*, Tech. Rep. ATLAS-CONF-2018-030, CERN, Geneva, Jul, 2018.  
2291 <https://cds.cern.ch/record/2629411>. 5, 5.7, 6.6.2
- 2292 [49] CMS Collaboration, CMS Collaboration, *Observation of electroweak production of same-sign*  
2293  *$W$  boson pairs in the two jet and two same-sign lepton final state in proton-proton collisions*  
2294 *at  $\sqrt{s} = 13$  TeV*, arXiv:1709.05822 [hep-ex]. 5
- 2295 [50] C. Bittrich, W. K. Di Clemente, et al., *Support note for measurement of electroweak*  
2296  *$W^\pm W^\pm jj$  production at  $\sqrt{s} = 13$  TeV*, Tech. Rep. ATL-COM-PHYS-2018-252, CERN,  
2297 Geneva, Mar, 2018. <https://cds.cern.ch/record/2309552>. 5, 5.3.3, 2, 4, 5.4.3
- 2298 [51] J. M. Campbell and R. K. Ellis, *Higgs Constraints from Vector Boson Fusion and Scattering*,  
2299 *JHEP* **04** (2015) 030, arXiv:1502.02990 [hep-ph]. 5.0.2, 5.0.3
- 2300 [52] M. Szleper, *The Higgs boson and the physics of  $WW$  scattering before and after Higgs*  
2301 *discovery*, arXiv:1412.8367 [hep-ph]. 5.0.2
- 2302 [53] E. Accomando, A. Ballestrero, A. Belhouari, and E. Maina, *Isolating Vector Boson Scattering*  
2303 *at the LHC: Gauge cancellations and the Equivalent Vector Boson Approximation vs complete*  
2304 *calculations*, *Phys. Rev.* **D74** (2006) 073010, arXiv:hep-ph/0608019 [hep-ph]. 5.0.2

- 2305 [54] P. Anger, B. Axen, et al., *Same Sign  $W^\pm W^\pm$  Production and Limits on Anomalous Quartic*  
 2306 *Gauge Couplings*, Tech. Rep. ATL-COM-PHYS-2013-990, CERN, Geneva, Jul, 2013.  
 2307 <https://cds.cern.ch/record/1561731>. Internal note for approved paper **STDM-2013-06**.  
 2308 **5.0.3, 5.1, 5.6**
- 2309 [55] J. Almond, L. Bianchini, et al., *Search for heavy neutrino,  $W_R$  and  $Z_R$  gauge bosons in events*  
 2310 *with two high- $P_T$  leptons and jets with the ATLAS detector in pp collisions at  $\sqrt{s} = 8$  TeV*,  
 2311 Tech. Rep. ATL-COM-PHYS-2013-810, CERN, Geneva, Jun, 2013.  
 2312 <https://cds.cern.ch/record/1555805>. Supporting note for EXOT-2012-24, published as  
 2313 JHEP07 (2015) 162. **5.0.4**
- 2314 [56] ATLAS Collaboration, M. Aaboud et al., *Luminosity determination in pp collisions at  $\sqrt{s} = 8$  TeV using the ATLAS detector at the LHC*, Eur. Phys. J. **C76** (2016) no. 12, 653,  
 2315 [arXiv:1608.03953 \[hep-ex\]](https://arxiv.org/abs/1608.03953). **5.1**
- 2317 [57] G. Avoni et al., *The new LUCID-2 detector for luminosity measurement and monitoring in*  
 2318 *ATLAS*, JINST **13** (2018) no. 07, P07017. **5.1**
- 2319 [58] ATLAS Collaboration, G. Aad et al., *The ATLAS Simulation Infrastructure*, Eur. Phys. J.  
 2320 **C70** (2010) 823–874, [arXiv:1005.4568 \[physics.ins-det\]](https://arxiv.org/abs/1005.4568). **5.1.1**
- 2321 [59] S. Agostinelli et al., *GEANT4 - a simulation toolkit*, Nucl. Instrum. Meth. **A506** (2003)  
 2322 **250–303**. **5.1.1**
- 2323 [60] T. Sjostrand, S. Mrenna, and P. Skands, *A Brief Introduction to PYTHIA 8.1*, Comput.  
 2324 Phys. Commun. **178** (2008) 852–867, [arXiv:0710.3820 \[hep-ph\]](https://arxiv.org/abs/0710.3820). **5.1.1**
- 2325 [61] T. Gleisberg et al., *Event generation with SHERPA 1.1*, JHEP **02** (2009) 007,  
 2326 [arXiv:0811.4622 \[hep-ph\]](https://arxiv.org/abs/0811.4622). **5.1.1**
- 2327 [62] S. Schumann and F. Krauss, *A parton shower algorithm based on Catani-Seymour dipole*  
 2328 *factorization*, JHEP **03** (2008) 038, [arXiv:0709.1027 \[hep-ph\]](https://arxiv.org/abs/0709.1027). **5.1.1**
- 2329 [63] S. Höche, F. Krauss, S. Schumann, and F. Siegert, *QCD matrix elements and truncated*  
 2330 *showers*, JHEP **05** (2009) 053, [arXiv:0903.1219 \[hep-ph\]](https://arxiv.org/abs/0903.1219). **5.1.1**
- 2331 [64] R. D. Ball et al., *Parton distributions for the LHC Run II*, JHEP **04** (2015) 040,  
 2332 [arXiv:1410.8849 \[hep-ph\]](https://arxiv.org/abs/1410.8849). **5.1.1**
- 2333 [65] S. Alioli, P. Nason, C. Oleari, and E. Re, *A general framework for implementing NLO*  
 2334 *calculations in shower Monte Carlo programs: the POWHEG BOX*, JHEP **06** (2010) 043,  
 2335 [arXiv:1002.2581 \[hep-ph\]](https://arxiv.org/abs/1002.2581). **5.1.1**
- 2336 [66] A. Ballestrero et al., *Precise predictions for same-sign  $W$ -boson scattering at the LHC*, Eur.  
 2337 Phys. J. **C78** (2018) no. 8, 671, [arXiv:1803.07943 \[hep-ph\]](https://arxiv.org/abs/1803.07943). **5.1.1**
- 2338 [67] J. Alwall, R. Frederix, S. Frixione, V. Hirschi, F. Maltoni, O. Mattelaer, H. S. Shao,  
 2339 T. Stelzer, P. Torrielli, and M. Zaro, *The automated computation of tree-level and*  
 2340 *next-to-leading order differential cross sections, and their matching to parton shower*  
 2341 *simulations*, JHEP **07** (2014) 079, [arXiv:1405.0301 \[hep-ph\]](https://arxiv.org/abs/1405.0301). **5.1.1**
- 2342 [68] H.-L. Lai, M. Guzzi, J. Huston, Z. Li, P. M. Nadolsky, J. Pumplin, and C. P. Yuan, *New*  
 2343 *parton distributions for collider physics*, Phys. Rev. D **82** (2010) 074024, [arXiv:1007.2241](https://arxiv.org/abs/1007.2241)  
 2344 [\[hep-ph\]](https://arxiv.org/abs/hep-ph). **5.1.1**

- 2345 [69] T. Sjostrand, S. Mrenna, and P. Skands, *PYTHIA 6.4 physics and manual*, JHEP **05** (2006)  
 2346 026, [arXiv:0603175 \[hep-ph\]](https://arxiv.org/abs/0603175). 5.1.1
- 2347 [70] ATLAS Collaboration, G. Aad et al., *Muon reconstruction performance of the ATLAS*  
 2348 *detector in protonproton collision data at  $\sqrt{s} = 13$  TeV*, Eur. Phys. J. **C76** (2016) no. 5, 292,  
 2349 [arXiv:1603.05598 \[hep-ex\]](https://arxiv.org/abs/1603.05598). 5.2.1.1, 12
- 2350 [71] ATLAS Collaboration Collaboration, *Electron efficiency measurements with the ATLAS*  
 2351 *detector using the 2015 LHC proton-proton collision data*, Tech. Rep.  
 2352 ATLAS-CONF-2016-024, CERN, Geneva, Jun, 2016.  
 2353 <https://cds.cern.ch/record/2157687>. 5.2.1.2
- 2354 [72] M. Cacciari, G. P. Salam, G. Soyez, *The anti- $k_t$  jet clustering algorithm*, JHEP **04** (2008) 063,  
 2355 [arXiv:0802.1189 \[hep-ph\]](https://arxiv.org/abs/0802.1189). 5.2.1.3, 6.4.1
- 2356 [73] ATLAS Collaboration, M. Aaboud et al., *Jet energy scale measurements and their systematic*  
 2357 *uncertainties in proton-proton collisions at  $\sqrt{s} = 13$  TeV with the ATLAS detector*, Phys.  
 2358 Rev. **D96** (2017) no. 7, 072002, [arXiv:1703.09665 \[hep-ex\]](https://arxiv.org/abs/1703.09665). 5.2.1.3
- 2359 [74] *Tagging and suppression of pileup jets with the ATLAS detector*, Tech. Rep.  
 2360 ATLAS-CONF-2014-018, CERN, Geneva, May, 2014.  
 2361 [http://cds.cern.ch/record/1700870](https://cds.cern.ch/record/1700870). 5.2.1.3
- 2362 [75] D. Adams, C. Anastopoulos, et al., *Recommendations of the Physics Objects and Analysis*  
 2363 *Harmonisation Study Groups 2014*, Tech. Rep. ATL-PHYS-INT-2014-018, CERN, Geneva,  
 2364 Jul, 2014. <https://cds.cern.ch/record/1743654>. 5.2.1.4
- 2365 [76] ATLAS Collaboration, M. Aaboud et al., *Measurement of the cross-section for producing a W*  
 2366 *boson in association with a single top quark in pp collisions at  $\sqrt{s} = 13$  TeV with ATLAS*,  
 2367 JHEP **01** (2018) 063, [arXiv:1612.07231 \[hep-ex\]](https://arxiv.org/abs/1612.07231). 5.2.1.4
- 2368 [77] ATLAS Collaboration, M. Aaboud et al., *Performance of missing transverse momentum*  
 2369 *reconstruction with the ATLAS detector using proton-proton collisions at  $\sqrt{s} = 13$  TeV*, Eur.  
 2370 Phys. J. **C78** (2018) no. 11, 903, [arXiv:1802.08168 \[hep-ex\]](https://arxiv.org/abs/1802.08168). 5.2.2
- 2371 [78] ATLAS Collaboration, M. Aaboud et al., *Measurements of b-jet tagging efficiency with the*  
 2372 *ATLAS detector using  $t\bar{t}$  events at  $\sqrt{s} = 13$  TeV*, JHEP **08** (2018) 089, [arXiv:1805.01845](https://arxiv.org/abs/1805.01845)  
 2373 [hep-ex]. 5.2.2
- 2374 [79] J.-F. Arguin, J. Claude, G. Gonella, B. P. Kersevan, K. Koneke, K. Lohwasser, K. Mochizuki,  
 2375 M. Muskinja, C. Piaulet, and P. Sommer, *Support Note for Electron ID: charge*  
 2376 *mis-identification*, Tech. Rep. ATL-COM-PHYS-2017-1014, CERN, Geneva, Jul, 2017.  
 2377 <https://cds.cern.ch/record/2273365>. 5.3.3
- 2378 [80] C.-H. Kom and W. J. Stirling, *Charge asymmetry in W + jets production at the LHC*, Eur.  
 2379 Phys. J. **C69** (2010) 67–73, [arXiv:1004.3404 \[hep-ph\]](https://arxiv.org/abs/1004.3404). 5.4
- 2380 [81] R. Steerenberg, *LHC Report: Another run is over and LS2 has just begun...*,  
 2381 [https://home.cern/news/news/accelerators/](https://home.cern/news/news/accelerators/lhc-report-another-run-over-and-ls2-has-just-begun)  
 2382 [lhc-report-another-run-over-and-ls2-has-just-begun](https://home.cern/news/news/accelerators/lhc-report-another-run-over-and-ls2-has-just-begun), 2018. Accessed: 2018-12-14. 6
- 2383 [82] *Letter of Intent for the Phase-I Upgrade of the ATLAS Experiment*, Tech. Rep.  
 2384 CERN-LHCC-2011-012. LHCC-I-020, CERN, Geneva, Nov, 2011.  
 2385 [http://cds.cern.ch/record/1402470](https://cds.cern.ch/record/1402470). 6

- 2386 [83] G. Apollinari, I. Bjar Alonso, O. Brning, M. Lamont, and L. Rossi, *High-Luminosity Large*  
2387 *Hadron Collider (HL-LHC): Preliminary Design Report*. CERN Yellow Reports: Monographs.  
2388 CERN, Geneva, 2015. <https://cds.cern.ch/record/2116337>. 6
- 2389 [84] ATLAS Collaboration Collaboration, ATLAS Collaboration, *ATLAS Phase-II Upgrade*  
2390 *Scoping Document*, Cern-lhcc-2015-020, Geneva, Sep, 2015.  
2391 <http://cds.cern.ch/record/2055248>. 6
- 2392 [85] D. Espriu and B. Yencho, *Longitudinal WW scattering in light of the “Higgs boson”*  
2393 *discovery*, *Phys. Rev. D* **87** (2013) 055017, arXiv:1212.4158 [hep-ph]. 6, 6.1
- 2394 [86] ATLAS Collaboration Collaboration, *Prospects for the measurement of the  $W^\pm W^\pm$  scattering*  
2395 *cross section and extraction of the longitudinal scattering component in pp collisions at the*  
2396 *High-Luminosity LHC with the ATLAS experiment*, Tech. Rep. ATL-PHYS-PUB-2018-052,  
2397 CERN, Geneva, Dec, 2018. <http://cds.cern.ch/record/2652447>. 6
- 2398 [87] ATLAS Collaboration Collaboration, *Studies on the impact of an extended Inner Detector*  
2399 *tracker and a forward muon tagger on  $W^\pm W^\pm$  scattering in pp collisions at the*  
2400 *High-Luminosity LHC with the ATLAS experiment*, Tech. Rep. ATL-PHYS-PUB-2017-023,  
2401 CERN, Geneva, Dec, 2017. <https://cds.cern.ch/record/2298958>. 6
- 2402 [88] T. Sjöstrand, S. Ask, J. R. Christiansen, R. Corke, N. Desai, P. Ilten, S. Mrenna, S. Prestel,  
2403 C. O. Rasmussen, and P. Z. Skands, *An Introduction to PYTHIA 8.2*, *Comput. Phys.*  
2404 *Commun.* **191** (2015) 159–177, arXiv:1410.3012 [hep-ph]. 6.2
- 2405 [89] ATLAS Collaboration Collaboration, *Expected performance for an upgraded ATLAS detector*  
2406 *at High-Luminosity LHC*, Tech. Rep. ATL-PHYS-PUB-2016-026, CERN, Geneva, Oct, 2016.  
2407 <http://cds.cern.ch/record/2223839>. 6.3
- 2408 [90] P. C. Bhat, H. B. Prosper, S. Sekmen, and C. Stewart, *Optimizing Event Selection with the*  
2409 *Random Grid Search*, *Comput. Phys. Commun.* **228** (2018) 245–257, arXiv:1706.09907  
2410 [hep-ph]. 6.5.1
- 2411 [91] G. Cowan, K. Cranmer, E. Gross, and O. Vitells, *Asymptotic formulae for likelihood-based*  
2412 *tests of new physics*, *Eur. Phys. J. C* **71** (2011) 1554, arXiv:1007.1727 [physics.data-an].  
2413 [Erratum: Eur. Phys. J.C73,2501(2013)]. 6.5.1